

Population properties of compact objects from the second LIGO–Virgo Gravitational-Wave Transient Catalog

R. ABBOTT,¹ T. D. ABBOTT,² S. ABRAHAM,³ F. ACERNESE,^{4,5} K. ACKLEY,⁶ A. ADAMS,⁷ C. ADAMS,⁸
R. X. ADHIKARI,¹ V. B. ADYA,⁹ C. AFFELDT,^{10,11} M. AGATHOS,^{12,13} K. AGATSUMA,¹⁴ N. AGGARWAL,¹⁵
O. D. AGUIAR,¹⁶ L. AIELLO,^{17,18} A. AIN,^{19,20} P. AJITH,²¹ G. ALLEN,²² A. ALLOCCA,¹⁹ P. A. ALTIN,⁹ A. AMATO,²³
S. ANAND,¹ A. ANANYEVA,¹ S. B. ANDERSON,¹ W. G. ANDERSON,²⁴ S. V. ANGELOVA,²⁵ S. ANSOLDI,^{26,27}
J. M. ANTELIS,²⁸ S. ANTIER,²⁹ S. APPERT,¹ K. ARAI,¹ M. C. ARAYA,¹ J. S. AREEDA,³⁰ M. ARÈNE,²⁹ N. ARNAUD,^{31,32}
S. M. ARONSON,³³ K. G. ARUN,³⁴ Y. ASALI,³⁵ S. ASCENZI,^{17,36} G. ASHTON,⁶ S. M. ASTON,⁸ P. ASTONE,³⁷
F. AUBIN,³⁸ P. AUFMUTH,^{10,11} K. AULTONEAL,²⁸ C. AUSTIN,² V. AVENDANO,³⁹ S. BABAK,²⁹ F. BADARACCO,^{17,18}
M. K. M. BADER,⁴⁰ S. BAE,⁴¹ A. M. BAER,⁷ S. BAGNASCO,⁴² J. BAIRD,²⁹ M. BALL,⁴³ G. BALLARDIN,³²
S. W. BALLMER,⁴⁴ A. BALS,²⁸ A. BALSAMO,⁷ G. BALTUS,⁴⁵ S. BANAGIRI,⁴⁶ D. BANKAR,³ R. S. BANKAR,³
J. C. BARAYOGA,¹ C. BARBIERI,^{47,48,49} B. C. BARISH,¹ D. BARKER,⁵⁰ P. BARNEO,⁵¹ S. BARNUM,⁵² F. BARONE,^{53,5}
B. BARR,⁵⁴ L. BARSOTTI,⁵² M. BARSUGLIA,²⁹ D. BARTA,⁵⁵ J. BARTLETT,⁵⁰ I. BARTOS,³³ R. BASSIRI,⁵⁶ A. BASTI,^{20,19}
M. BAWAJ,^{57,58} J. C. BAYLEY,⁵⁴ M. BAZZAN,^{59,60} B. R. BECHER,⁶¹ B. BÉCSY,⁶² V. M. BEDAKIHALE,⁶³ M. BEJGER,⁶⁴
I. BELAHCENE,³¹ D. BENIWAL,⁶⁵ M. G. BENJAMIN,²⁸ T. F. BENNETT,⁶⁶ J. D. BENTLEY,¹⁴ F. BERGAMIN,^{10,11}
B. K. BERGER,⁵⁶ G. BERGMANN,^{10,11} S. BERNUZZI,¹³ C. P. L. BERRY,¹⁵ D. BERSANETTI,⁶⁷ A. BERTOLINI,⁴⁰
J. BETZWIESER,⁸ R. BHANDARE,⁶⁸ A. V. BHANDARI,³ D. BHATTACHARJEE,⁶⁹ J. BIDLER,³⁰ I. A. BILENKO,⁷⁰
G. BILLINGSLEY,¹ R. BIRNEY,⁷¹ O. BIRNHOLTZ,⁷² S. BISCANS,^{1,52} M. BISCHI,^{73,74} S. BISCOVEANU,⁵² A. BISHT,^{10,11}
M. BITOSSI,^{32,19} M.-A. BIZOUARD,⁷⁵ J. K. BLACKBURN,¹ J. BLACKMAN,⁷⁶ C. D. BLAIR,⁷⁷ D. G. BLAIR,⁷⁷
R. M. BLAIR,⁵⁰ O. BLANCH,⁷⁸ F. BOBBA,^{79,80} N. BODE,^{10,11} M. BOER,⁷⁵ Y. BOETZEL,⁸¹ G. BOGAERT,⁷⁵
M. BOLDRINI,^{82,37} F. BONDU,⁸³ E. BONILLA,⁵⁶ R. BONNAND,³⁸ P. BOOKER,^{10,11} B. A. BOOM,⁴⁰ R. BORK,¹
V. BOSCHI,¹⁹ S. BOSE,³ V. BOSSILKOV,⁷⁷ V. BOUDART,⁴⁵ Y. BOUFFANAIS,^{59,60} A. BOZZI,³² C. BRADASCHIA,¹⁹
P. R. BRADY,²⁴ A. BRAMLEY,⁸ M. BRANCHESI,^{17,18} J. E. BRAU,⁴³ M. BRESCHI,¹³ T. BRIANT,⁸⁴ J. H. BRIGGS,⁵⁴
F. BRIGHENTI,^{73,74} A. BRILLET,⁷⁵ M. BRINKMANN,^{10,11} P. BROCKILL,²⁴ A. F. BROOKS,¹ J. BROOKS,³²
D. D. BROWN,⁶⁵ S. BRUNETT,¹ G. BRUNO,⁸⁵ R. BRUNTZ,⁷ A. BUIKEMA,⁵² T. BULIK,⁸⁶ H. J. BULTEN,^{40,87}
A. BUONANNO,^{88,89} R. BUSCICCHIO,¹⁴ D. BUSKULIC,³⁸ R. L. BYER,⁵⁶ M. CABERO,^{10,11} L. CADONATI,⁹⁰ M. CAESAR,⁹¹
G. CAGNOLI,²³ C. CAHILLANE,¹ J. CALDERÓN BUSTILLO,⁶ J. D. CALLAGHAN,⁵⁴ T. A. CALLISTER,⁹² E. CALLONI,^{93,5}
J. B. CAMP,⁹⁴ M. CANEPA,^{95,67} K. C. CANNON,⁹⁶ H. CAO,⁶⁵ J. CAO,⁹⁷ G. CARAPELLA,^{79,80} F. CARBOGNANI,³²
M. F. CARNEY,¹⁵ M. CARPINELLI,^{98,99} G. CARULLO,^{20,19} T. L. CARVER,¹⁰⁰ J. CASANUEVA DIAZ,³² C. CASENTINI,^{101,36}
S. CAUDILL,⁴⁰ M. CAVAGLIÀ,⁶⁹ F. CAVALIER,³¹ R. CAVALIERI,³² G. CELLA,¹⁹ P. CERDÁ-DURÁN,¹⁰² E. CESARINI,³⁶
W. CHAIBI,⁷⁵ K. CHAKRAVARTI,³ C.-L. CHAN,¹⁰³ C. CHAN,⁹⁶ K. CHANDRA,¹⁰⁴ P. CHANIAL,³² S. CHAO,¹⁰⁵
P. CHARLTON,¹⁰⁶ E. A. CHASE,¹⁵ E. CHASSANDE-MOTTIN,²⁹ D. CHATTERJEE,²⁴ D. CHATTOPADHYAY,¹⁰⁷
M. CHATURVEDI,⁶⁸ K. CHATZIOANNOU,⁹² A. CHEN,¹⁰³ H. Y. CHEN,¹⁰⁸ X. CHEN,⁷⁷ Y. CHEN,⁷⁶ H.-P. CHENG,³³
C. K. CHEONG,¹⁰³ H. Y. CHIA,³³ F. CHIADINI,^{109,80} R. CHIERICI,¹¹⁰ A. CHINCARINI,⁶⁷ A. CHIUMMO,³² G. CHO,¹¹¹
H. S. CHO,¹¹² M. CHO,⁸⁹ S. CHOATE,⁹¹ N. CHRISTENSEN,⁷⁵ Q. CHU,⁷⁷ S. CHUA,⁸⁴ K. W. CHUNG,¹¹³ S. CHUNG,⁷⁷
G. CIANI,^{59,60} P. CIECIELAG,⁶⁴ M. CIEŚLAR,⁶⁴ M. CIFALDI,^{101,36} A. A. CIOBANU,⁶⁵ R. CIOLFI,^{114,60} F. CIPRIANO,⁷⁵
A. CIRONE,^{95,67} F. CLARA,⁵⁰ E. N. CLARK,¹¹⁵ J. A. CLARK,⁹⁰ L. CLARKE,¹¹⁶ P. CLEARWATER,¹¹⁷ S. CLESSE,⁸⁵
F. CLEVA,⁷⁵ E. COCCIA,^{17,18} P.-F. COHADON,⁸⁴ D. E. COHEN,³¹ M. COLLEONI,¹¹⁸ C. G. COLLETTE,¹¹⁹ C. COLLINS,¹⁴
M. COLPI,^{47,48} M. CONSTANCIO JR.,¹⁶ L. CONTI,⁶⁰ S. J. COOPER,¹⁴ P. CORBAN,⁸ T. R. CORBITT,²
I. CORDERO-CARRIÓN,¹²⁰ S. COREZZI,^{58,57} K. R. CORLEY,³⁵ N. CORNISH,⁶² D. CORRE,³¹ A. CORSI,¹²¹ S. CORTESE,³²
C. A. COSTA,¹⁶ R. COTESTA,⁸⁸ M. W. COUGHLIN,^{46,1} S. B. COUGHLIN,^{15,100} J.-P. COULON,⁷⁵ S. T. COUNTRYMAN,³⁵
P. COUVARES,¹ P. B. COVAS,¹¹⁸ D. M. COWARD,⁷⁷ M. J. COWART,⁸ D. C. COYNE,¹ R. COYNE,¹²²
J. D. E. CREIGHTON,²⁴ T. D. CREIGHTON,¹²³ M. CROQUETTE,⁸⁴ S. G. CROWDER,¹²⁴ J.R. CUDELL,⁴⁵ T. J. CULLEN,²
A. CUMMING,⁵⁴ R. CUMMINGS,⁵⁴ L. CUNNINGHAM,⁵⁴ E. CUOCO,^{32,125} M. CURYLO,⁸⁶ T. DAL CANTON,^{31,88}
G. DÁLYA,¹²⁶ A. DANA,⁵⁶ L. M. DANESHGARANBAJASTANI,⁶⁶ B. D'ANGELO,^{95,67} S. L. DANILISHIN,¹²⁷ S. D'ANTONIO,³⁶
K. DANZMANN,^{10,11} C. DARSOW-FROMM,¹²⁸ A. DASGUPTA,⁶³ L. E. H. DATRIER,⁵⁴ V. DATTILO,³² I. DAVE,⁶⁸
M. DAVIER,³¹ G. S. DAVIES,¹²⁹ D. DAVIS,¹ E. J. DAW,¹³⁰ R. DEAN,⁹¹ D. DEBRA,⁵⁶ M. DEENADAYALAN,³
J. DEGALLAIX,¹³¹ M. DE LAURENTIS,^{93,5} S. DELÉGLISE,⁸⁴ V. DEL FAVERO,¹³² F. DE LILLO,⁸⁵ N. DE LILLO,⁵⁴
W. DEL POZZO,^{20,19} L. M. DEMARCHI,¹⁵ F. DE MATTEIS,^{101,36} V. D'EMILIO,¹⁰⁰ N. DEMOS,⁵² T. DENKER,^{10,11}
T. DENT,¹²⁹ A. DEPASSE,⁸⁵ R. DE PIETRI,^{133,134} R. DE ROSA,^{93,5} C. DE ROSSI,³² R. DESALVO,^{135,80}
O. DE VARONA,^{10,11} S. DHURANDHAR,³ M. C. DÍAZ,¹²³ M. DIAZ-ORTIZ JR.,³³ N. A. DIDIO,⁴⁴ T. DIETRICH,⁴⁰
L. DI FIORE,⁵ C. DIFRONZO,¹⁴ C. DI GIORGIO,^{79,80} F. DI GIOVANNI,¹⁰² M. DI GIOVANNI,^{136,137} T. DI GIROLAMO,^{93,5}
A. DI LIETO,^{20,19} B. DING,¹¹⁹ S. DI PACE,^{82,37} I. DI PALMA,^{82,37} F. DI RENZO,^{20,19} A. K. DIVAKARLA,³³
A. DMITRIEV,¹⁴ Z. DOCTOR,⁴³ L. D'ONOFRIO,^{93,5} F. DONOVAN,⁵² K. L. DOOLEY,¹⁰⁰ S. DORAVARI,³ I. DORRINGTON,¹⁰⁰
T. P. DOWNES,²⁴ M. DRAGO,^{17,18} J. C. DRIGGERS,⁵⁰ Z. DU,⁹⁷ J.-G. DUCOIN,³¹ P. DUPEJ,⁵⁴ O. DURANTE,^{79,80}
D. D'URSO,^{98,99} P.-A. DUVERNE,³¹ S. E. DWYER,⁵⁰ P. J. EASTER,⁶ G. EDDOLLS,⁵⁴ B. EDELMAN,⁴³ T. B. EDO,¹³⁰
O. EDY,¹³⁸ A. EFFLER,⁸ J. EICHHOLZ,⁹ S. S. EIKENBERRY,³³ M. EISENMANN,³⁸ R. A. EISENSTEIN,⁵² A. EJLLI,¹⁰⁰
L. ERRICO,^{93,5} R. C. ESSICK,¹⁰⁸ H. ESTELLÉS,¹¹⁸ D. ESTEVEZ,³⁸ Z. B. ETIENNE,¹³⁹ T. ETZEL,¹ M. EVANS,⁵²

- T. M. EVANS,⁸ B. E. EWING,¹⁴⁰ V. FAFONE,^{101,36,17} H. FAIR,⁴⁴ S. FAIRHURST,¹⁰⁰ X. FAN,⁹⁷ A. M. FARAH,¹⁰⁸
 S. FARINON,⁶⁷ B. FARR,⁴³ W. M. FARR,^{141,92} E. J. FAUCHON-JONES,¹⁰⁰ M. FAVATA,³⁹ M. FAYS,^{45,130} M. FAZIO,¹⁴²
 J. FEICHT,¹ M. M. FEJER,⁵⁶ F. FENG,²⁹ E. FENYVESI,^{55,143} D. L. FERGUSON,⁹⁰ A. FERNANDEZ-GALIANA,⁵²
 I. FERRANTE,^{20,19} T. A. FERREIRA,¹⁶ F. FIDECARO,^{20,19} P. FIGURA,⁸⁶ I. FIORI,³² D. FIORUCCI,^{17,18} M. FISHBACH,¹⁰⁸
 R. P. FISHER,⁷ J. M. FISHNER,⁵² R. FITTIPALDI,^{144,80} M. FITZ-AXEN,⁴⁶ V. FIUMARA,^{145,80} R. FLAMINIO,^{38,146}
 E. FLODEN,⁴⁶ E. FLYNN,³⁰ H. FONG,⁹⁶ J. A. FONT,^{102,147} P. W. F. FORSYTH,⁹ J.-D. FOURNIER,⁷⁵ S. FRASCA,^{82,37}
 F. FRASCONI,¹⁹ Z. FREI,¹²⁶ A. FREISE,¹⁴ R. FREY,⁴³ V. FREY,³¹ P. FRITSCHER,⁵² V. V. FROLOV,⁸ G. G. FRONZÉ,⁴²
 P. FULDA,³³ M. FYFFE,⁸ H. A. GABBARD,⁵⁴ B. U. GADRE,⁸⁸ S. M. GAEBEL,¹⁴ J. R. GAIR,⁸⁸ J. GAIS,¹⁰³
 S. GALAUDAGE,⁶ R. GAMBA,¹³ D. GANAPATHY,⁵² A. GANGULY,²¹ S. G. GAONKAR,³ B. GARAVENTA,^{67,95}
 C. GARCÍA-QUIRÓS,¹¹⁸ F. GARUFI,^{93,5} B. GATELEY,⁵⁰ S. GAUDIO,²⁸ V. GAYATHRI,³³ G. GEMME,⁶⁷ A. GENNAI,¹⁹
 D. GEORGE,²² J. GEORGE,⁶⁸ L. GERGELY,¹⁴⁸ S. GHONGE,⁹⁰ ABHIRUP GHOSH,⁸⁸ ARCHISMAN GHOSH,^{40,149,150,151}
 S. GHOSH,^{24,39} B. GIACOMAZZO,^{47,48,49} L. GIACOPPO,^{82,37} J. A. GIAIME,^{2,8} K. D. GIARDINA,⁸ D. R. GIBSON,⁷¹
 C. GIER,²⁵ K. GILL,³⁵ P. GIRI,^{19,20} J. GLANZER,² A. E. GLECKL,³⁰ P. GODWIN,¹⁴⁰ E. GOETZ,¹⁵² R. GOETZ,³³
 N. GOHLKE,^{10,11} B. GONCHAROV,⁶ G. GONZÁLEZ,² A. GOPAKUMAR,¹⁵³ S. E. GOSSAN,¹ M. GOSSELIN,^{20,19}
 R. GOUATY,³⁸ B. GRACE,⁹ A. GRADO,^{154,5} M. GRANATA,¹³¹ V. GRANATA,⁷⁹ A. GRANT,⁵⁴ S. GRAS,⁵² P. GRASSIA,¹
 C. GRAY,⁵⁰ R. GRAY,⁵⁴ G. GRECO,^{73,74} A. C. GREEN,³³ R. GREEN,¹⁰⁰ E. M. GREJARSSON,²⁸ H. L. GRIGGS,⁹⁰
 G. GRIGNANI,^{58,57} A. GRIMALDI,^{136,137} E. GRIMES,²⁸ S. J. GRIMM,^{17,18} H. GROTE,¹⁰⁰ S. GRUNEWALD,⁸⁸
 P. GRUNING,³¹ J. G. GUERRERO,³⁰ G. M. GUIDI,^{73,74} A. R. GUIMARAES,² G. GUIXÉ,⁵¹ H. K. GULATI,⁶³ Y. GUO,⁴⁰
 ANCHAL GUPTA,¹ ANURADHA GUPTA,¹⁴⁰ P. GUPTA,^{40,155} E. K. GUSTAFSON,¹ R. GUSTAFSON,¹⁵⁶ F. GUZMAN,¹¹⁵
 L. HAEGEL,²⁹ O. HALIM,^{18,17} E. D. HALL,⁵² E. Z. HAMILTON,¹⁰⁰ G. HAMMOND,⁵⁴ M. HANEY,⁸¹ M. M. HANKE,^{10,11}
 J. HANKS,⁵⁰ C. HANNA,¹⁴⁰ O. A. HANNUKSELA,¹⁰³ O. HANNUKSELA,^{155,40} H. HANSEN,⁵⁰ T. J. HANSEN,²⁸ J. HANSON,⁸
 T. HARDER,⁷⁵ T. HARDWICK,² K. HARIS,^{40,155,21} J. HARMS,^{17,18} G. M. HARRY,¹⁵⁷ I. W. HARRY,¹³⁸ D. HARTWIG,¹²⁸
 R. K. HASSKEW,⁸ C.-J. HASTER,⁵² K. HAUGHIAN,⁵⁴ F. J. HAYES,⁵⁴ J. HEALY,¹³² A. HEIDMANN,⁸⁴ M. C. HEINTZE,⁸
 J. HEINZE,^{10,11} J. HEINZEL,¹⁵⁸ H. HEITMANN,⁷⁵ F. HELLMAN,¹⁵⁹ P. HELLO,³¹ A. F. HELMLING-CORNELL,⁴³
 G. HEMMING,³² M. HENDRY,⁵⁴ I. S. HENG,⁵⁴ E. HENNES,⁴⁰ J. HENNIG,^{10,11} M. H. HENNIG,^{10,11}
 F. HERNANDEZ VIVANCO,⁶ M. HEURS,^{10,11} S. HILD,¹²⁷ P. HILL,²⁵ A. S. HINES,¹¹⁵ S. HOCHHEIM,^{10,11} E. HOFGARD,⁵⁶
 D. HOFMAN,¹³¹ J. N. HOHMANN,¹²⁸ A. M. HOLGADO,²² N. A. HOLLAND,⁹ I. J. HOLLOWS,¹³⁰ Z. J. HOLMES,⁶⁵
 K. HOLT,⁸ D. E. HOLZ,¹⁰⁸ P. HOPKINS,¹⁰⁰ C. HORST,²⁴ J. HOUGH,⁵⁴ E. J. HOWELL,⁷⁷ C. G. HOY,¹⁰⁰ D. HOYLAND,¹⁴
 Y. HUANG,⁵² M. T. HÜBNER,⁶ A. D. HUDDART,¹¹⁶ E. A. HUERTA,²² B. HUGHEY,²⁸ V. HUI,³⁸ S. HUSA,¹¹⁸
 S. H. HUTTNER,⁵⁴ B. M. HUTZLER,² R. HUXFORD,¹⁴⁰ T. HUYNH-DINH,⁸ B. IDZKOWSKI,⁸⁶ A. IESS,^{101,36}
 S. IMPERATO,¹⁵ H. INCHAUSPE,³³ C. INGRAM,⁶⁵ G. INTINI,^{82,37} M. ISI,⁵² B. R. IYER,²¹ V. JABERIANHAMEDAN,⁷⁷
 T. JACQMIN,⁸⁴ S. J. JADHAV,¹⁶⁰ S. P. JADHAV,³ A. L. JAMES,¹⁰⁰ K. JANI,⁹⁰ K. JANSSENS,¹⁶¹ N. N. JANTHALUR,¹⁶⁰
 P. JARANOWSKI,¹⁶² D. JARIWALA,³³ R. JAUME,¹¹⁸ A. C. JENKINS,¹¹³ M. JEUNON,⁴⁶ J. JIANG,³³ G. R. JOHNS,⁷
 A. W. JONES,¹⁴ D. I. JONES,¹⁶³ J. D. JONES,⁵⁰ P. JONES,¹⁴ R. JONES,⁵⁴ R. J. G. JONKER,⁴⁰ L. JU,⁷⁷ J. JUNKER,^{10,11}
 C. V. KALAGHATGI,¹⁰⁰ V. KALOGERA,¹⁵ B. KAMAI,¹ S. KANDHASAMY,³ G. KANG,⁴¹ J. B. KANNER,¹ S. J. KAPADIA,²¹
 D. P. KAPASI,⁹ C. KARATHANASIS,⁷⁸ S. KARKI,⁶⁹ R. KASHYAP,¹⁴⁰ M. KASPRZACK,¹ W. KASTAUN,^{10,11}
 S. KATSANEVAS,³² E. KATSAVOUNIDIS,⁵² W. KATZMAN,⁸ K. KAWABE,⁵⁰ F. KÉFÉLIAN,⁷⁵ D. KEITEL,¹¹⁸ J. S. KEY,¹⁶⁴
 S. KHADKA,⁵⁶ F. Y. KHALILI,⁷⁰ I. KHAN,^{17,36} S. KHAN,¹⁰⁰ E. A. KHAZANOV,¹⁶⁵ N. KHETAN,^{17,18} M. KHURSHEED,⁶⁸
 N. KIJBUNCHOO,⁹ C. KIM,¹⁶⁶ G. J. KIM,⁹⁰ J. C. KIM,¹⁶⁷ K. KIM,¹⁶⁸ W. S. KIM,¹⁶⁹ Y.-M. KIM,¹⁷⁰ C. KIMBALL,¹⁵
 P. J. KING,⁵⁰ M. KINLEY-HANLON,⁵⁴ R. KIRCHHOFF,^{10,11} J. S. KISSEL,⁵⁰ L. KLEYBOLTE,¹²⁸ S. KLIMENKO,³³
 T. D. KNOWLES,¹³⁹ E. KNYAZEV,⁵² P. KOCH,^{10,11} S. M. KOEHLLENBECK,^{10,11} G. KOEKOEK,^{40,171} S. KOLEY,⁴⁰
 M. KOLSTEIN,⁷⁸ K. KOMORI,⁵² V. KONDRASHOV,¹ A. KONTOS,⁶¹ N. KOPER,^{10,11} M. KOROBKO,¹²⁸ W. Z. KORTH,¹
 M. KOVALAM,⁷⁷ D. B. KOZAK,¹ C. KRÄMER,^{10,11} V. KRINGEL,^{10,11} N. V. KRISHNENDU,^{10,11} A. KRÓLAK,^{172,173}
 G. KUEHN,^{10,11} A. KUMAR,¹⁶⁰ P. KUMAR,¹⁷⁴ RAHUL KUMAR,⁵⁰ RAKESH KUMAR,⁶³ K. KUNS,⁵² S. KWANG,²⁴
 B. D. LACKEY,⁸⁸ D. LAGHI,^{20,19} E. LALANDE,¹⁷⁵ T. L. LAM,¹⁰³ A. LAMBERTS,^{75,176} M. LANDRY,⁵⁰ B. B. LANE,⁵²
 R. N. LANG,⁵² J. LANGE,¹³² B. LANTZ,⁵⁶ R. K. LANZA,⁵² I. LA ROSA,³⁸ A. LARTAUD-VOLLARD,³¹ P. D. LASKY,⁶
 M. LAXEN,⁸ A. LAZZARINI,¹ C. LAZZARO,^{60,59} P. LEACI,^{82,37} S. LEAVEY,^{10,11} Y. K. LECOEUCE,⁵⁰ H. M. LEE,¹⁶⁸
 H. W. LEE,¹⁶⁷ J. LEE,¹¹¹ K. LEE,⁵⁶ J. LEHMANN,^{10,11} E. LEON,³⁰ N. LEROY,³¹ N. LETENDRE,³⁸ Y. LEVIN,⁶ A. LI,¹
 J. LI,⁹⁷ K. J. L. LI,¹⁰³ T. G. F. LI,¹⁰³ X. LI,⁷⁶ F. LINDE,^{177,40} S. D. LINKER,⁶⁶ J. N. LINLEY,⁵⁴
 T. B. LITTENBERG,¹⁷⁸ J. LIU,^{10,11} X. LIU,²⁴ M. LLORENS-MONTEAGUDO,¹⁰² R. K. L. LO,¹ A. LOCKWOOD,¹⁷⁹
 L. T. LONDON,⁵² A. LONGO,^{180,181} M. LORENZINI,^{101,36} V. LORIETTE,¹⁸² M. LORMAND,⁸ G. LOSURDO,¹⁹
 J. D. LOUGH,^{10,11} C. O. LOUSTO,¹³² G. LOVELACE,³⁰ H. LÜCK,^{10,11} D. LUMACA,^{101,36} A. P. LUNDGREN,¹³⁸ Y. MA,⁷⁶
 R. MACAS,¹⁰⁰ M. MACINNIS,⁵² D. M. MACLEOD,¹⁰⁰ I. A. O. MACMILLAN,¹ A. MACQUET,⁷⁵ I. MAGAÑA HERNANDEZ,²⁴
 F. MAGAÑA-SANDOVAL,³³ C. MAGAZZÙ,¹⁹ R. M. MAGEE,¹⁴⁰ E. MAJORANA,³⁷ I. MAKSIMOVIC,¹⁸² S. MALIAKAL,¹
 A. MALIK,⁶⁸ N. MAN,⁷⁵ V. MANDIC,⁴⁶ V. MANGANO,^{82,37} G. L. MANSELL,^{50,52} M. MANSKE,²⁴ M. MANTOVANI,³²
 M. MAPELLI,^{59,60} F. MARCHESONI,^{183,57} F. MARION,³⁸ S. MÁRKA,³⁵ Z. MÁRKA,³⁵ C. MARKAKIS,¹²
 A. S. MARKOSYAN,⁵⁶ A. MARKOWITZ,¹ E. MAROS,¹ A. MARQUINA,¹²⁰ S. MARSAT,²⁹ F. MARTELLI,^{73,74}
 I. W. MARTIN,⁵⁴ R. M. MARTIN,³⁹ M. MARTINEZ,⁷⁸ V. MARTINEZ,²³ D. V. MARTYNOV,¹⁴ H. MASALEHDAN,¹²⁸
 K. MASON,⁵² E. MASSERA,¹³⁰ A. MASSEROT,³⁸ T. J. MASSINGER,⁵² M. MASSO-REID,⁵⁴ S. MASTROGIOVANNI,²⁹
 A. MATAS,⁸⁸ M. MATEU-LUCENA,¹¹⁸ F. MATICHARD,^{1,52} M. MATIUSHECHKINA,^{10,11} N. MAVALVALA,⁵² E. MAYNARD,²
 J. J. McCANN,⁷⁷ R. MCCARTHY,⁵⁰ D. E. MCCLELLAND,⁹ S. MCCORMICK,⁸ L. MCCULLER,⁵² S. C. MCGUIRE,¹⁸⁴
 C. McISAAC,¹³⁸ J. McIVER,¹⁵² D. J. McMANUS,⁹ T. McRAE,⁹ S. T. McWILLIAMS,¹³⁹ D. MEACHER,²⁴

- G. D. MEADORS,⁶ M. MEHMET,^{10, 11} A. K. MEHTA,⁸⁸ A. MELATOS,¹¹⁷ D. A. MELCHOR,³⁰ G. MENDELL,⁵⁰
A. MENENDEZ-VAZQUEZ,⁷⁸ R. A. MERCER,²⁴ L. MERENI,¹³¹ K. MERFELD,⁴³ E. L. MERILH,⁵⁰ J. D. MERRITT,⁴³
M. MERZOUGUI,⁷⁵ S. MESHKOV,¹ C. MESSENGER,⁵⁴ C. MESSICK,¹⁸⁵ R. METZDORFF,⁸⁴ P. M. MEYERS,¹¹⁷
F. MEYLAHN,^{10, 11} A. MHASKE,³ A. MIANI,^{136, 137} H. MIAO,¹⁴ I. MICHALOLIAKOS,³³ C. MICHEL,¹³¹ H. MIDDLETON,¹¹⁷
L. MILANO,^{93, 5} A. L. MILLER,^{33, 85} S. MILLER,^{186, 92} M. MILLHOUSE,¹¹⁷ J. C. MILLS,¹⁰⁰ E. MILOTTI,^{187, 27}
M. C. MILOVICH-GOFF,⁶⁶ O. MINAZZOLI,^{75, 188} Y. MINENKOV,³⁶ LL. M. MIR,⁷⁸ A. MISHKIN,³³ C. MISHRA,¹⁸⁹
T. MISTRY,¹³⁰ S. MITRA,³ V. P. MITROFANOV,⁷⁰ G. MITSELMAKHER,³³ R. MITTLEMAN,⁵² G. MO,⁵² K. MOGUSHI,⁶⁹
S. R. P. MOHAPATRA,⁵² S. R. MOHITE,²⁴ I. MOLINA,³⁰ M. MOLINA-RUIZ,¹⁵⁹ M. MONDIN,⁶⁶ M. MONTANI,^{73, 74}
C. J. MOORE,¹⁴ D. MORARU,⁵⁰ F. MORAWSKI,⁶⁴ G. MORENO,⁵⁰ S. MORISAKI,⁹⁶ B. MOURS,¹⁹⁰ C. M. MOW-LOWRY,¹⁴
S. MOZZON,¹³⁸ F. MUCIACCIA,^{82, 37} ARUNAVA MUKHERJEE,⁵⁴ D. MUKHERJEE,¹⁴⁰ SOMA MUKHERJEE,¹²³
SUBROTO MUKHERJEE,⁶³ N. MUKUND,^{10, 11} A. MULLAVEY,⁸ J. MUNCH,⁶⁵ E. A. MUÑOZ,⁴⁴ P. G. MURRAY,⁵⁴
S. L. NADJI,^{10, 11} A. NAGAR,^{191, 42, 192} I. NARDECCHIA,^{101, 36} L. NATICCHIONI,³⁷ R. K. NAYAK,¹⁹³ B. F. NEIL,⁷⁷
J. NEILSON,^{135, 80} G. NELEMANS,¹⁹⁴ T. J. N. NELSON,⁸ M. NERY,^{10, 11} A. NEUNZERT,¹⁶⁴ K. Y. NG,⁵² S. NG,⁶⁵
C. NGUYEN,²⁹ P. NGUYEN,⁴³ T. NGUYEN,⁵² S. A. NICHOLS,² S. NISSANKE,^{149, 40} F. NOCERA,³² M. NOH,¹⁵²
C. NORTH,¹⁰⁰ D. NOTHARD,¹⁹⁵ L. K. NUTTALL,¹³⁸ J. OBERLING,⁵⁰ B. D. O'BRIEN,³³ J. O'DELL,¹¹⁶
G. OGANESYAN,^{17, 18} G. H. OGIN,¹⁹⁶ J. J. OH,¹⁶⁹ S. H. OH,¹⁶⁹ F. OHME,^{10, 11} H. OHTA,⁹⁶ M. A. OKADA,¹⁶
C. OLIVETTO,³² P. OPPERMAN,^{10, 11} R. J. ORAM,⁸ B. O'REILLY,⁸ R. G. ORMISTON,⁴⁶ N. ORMSBY,⁷ L. F. ORTEGA,³³
R. O'SHAUGHNESSY,¹³² S. OSSOKINE,⁸⁸ C. OSTHELDER,¹ D. J. OTTAWAY,⁶⁵ H. OVERMIER,⁸ B. J. OWEN,¹²¹
A. E. PACE,¹⁴⁰ G. PAGANO,^{20, 19} M. A. PAGE,⁷⁷ G. PAGLIAROLI,^{17, 18} A. PAI,¹⁰⁴ S. A. PAI,⁶⁸ J. R. PALAMOS,⁴³
O. PALASHOV,¹⁶⁵ C. PALOMBA,³⁷ H. PAN,¹⁰⁵ P. K. PANDA,¹⁶⁰ T. H. PANG,^{40, 155} C. PANKOW,¹⁵ F. PANNARALE,^{82, 37}
B. C. PANT,⁶⁸ F. PAOLETTI,¹⁹ A. PAOLI,³² A. PAOLONE,^{37, 197} W. PARKER,^{8, 184} D. PASCUCCHI,⁴⁰ A. PASQUALETTI,³²
R. PASSAQUETI,^{20, 19} D. PASSUELLO,¹⁹ M. PATEL,⁷ B. PATRICELLI,^{20, 19} E. PAYNE,⁶ T. C. PECHSIRI,³³ M. PEDRAZA,¹
M. PEGORARO,⁶⁰ A. PELE,⁸ S. PENN,¹⁹⁸ A. PEREGO,^{136, 137} C. J. PEREZ,⁵⁰ C. PÉRIGOIS,³⁸ A. PERRECA,^{136, 137}
S. PERRIÈS,¹¹⁰ J. PETERMANN,¹²⁸ D. PETTERSON,¹ H. P. PFEIFFER,⁸⁸ K. A. PHAM,⁴⁶ K. S. PHUKON,^{40, 177, 3}
O. J. PICCINNI,^{82, 37} M. PICHOT,⁷⁵ M. PIENDIBENE,^{20, 19} F. PIERGIOVANNI,^{73, 74} L. PIERINI,^{82, 37} V. PIERRO,^{135, 80}
G. PILLANT,³² F. PILO,¹⁹ L. PINARD,¹³¹ I. M. PINTO,^{135, 80, 191} K. PIOTRZKOWSKI,⁸⁵ M. PIRELLO,⁵⁰ M. PITKIN,¹⁹⁹
E. PLACIDI,⁸² W. PLASTINO,^{180, 181} C. PLUCHAR,¹¹⁵ R. POGGIANI,^{20, 19} E. POLINI,³⁸ D. Y. T. PONG,¹⁰³
S. PONRATHNAM,³ P. POPOLIZIO,³² E. K. PORTER,²⁹ A. POVERMAN,⁶¹ J. POWELL,¹⁰⁷ M. PRACCHIA,³⁸
A. K. PRAJAPATI,⁶³ K. PRASAI,⁵⁶ R. PRASANNA,¹⁶⁰ G. PRATTEN,¹⁴ T. PRESTEGARD,²⁴ M. PRINCIPE,^{135, 191, 80}
G. A. PRODI,^{200, 137} L. PROKHOROV,¹⁴ P. PROSPITO,^{101, 36} A. PUECHER,^{40, 155} M. PUNTURO,⁵⁷ F. PUOSI,^{19, 20}
P. PUPPO,³⁷ M. PÜRRER,⁸⁸ H. QI,¹⁰⁰ V. QUETSCHKE,¹²³ P. J. QUINONEZ,²⁸ R. QUITZOW-JAMES,⁶⁹ F. J. RAAB,⁵⁰
G. RAAIJMAKERS,^{149, 40} H. RADKINS,⁵⁰ N. RADULESCU,⁷⁵ P. RAFFAI,¹²⁶ H. RAFFERTY,²⁰¹ S. X. RAIL,¹⁷⁵ S. RAJA,⁶⁸
C. RAJAN,⁶⁸ B. RAJBHANDARI,¹²¹ M. RAKHMANOV,¹²³ K. E. RAMIREZ,¹²³ T. D. RAMIREZ,³⁰ A. RAMOS-BUADES,¹¹⁸
J. RANA,¹⁴⁰ K. RAO,¹⁵ P. RAPAGNANI,^{82, 37} U. D. RAPOL,²⁰² B. RATTO,²⁸ V. RAYMOND,¹⁰⁰ M. RAZZANO,^{20, 19}
J. READ,³⁰ T. REGIMBAU,³⁸ L. REI,⁶⁷ S. REID,²⁵ D. H. REITZE,^{1, 33} P. RETTEGNO,^{203, 42} F. RICCI,^{82, 37}
C. J. RICHARDSON,²⁸ J. W. RICHARDSON,¹ L. RICHARDSON,¹¹⁵ P. M. RICKER,²² G. RIEMENSCHNEIDER,^{203, 42}
K. RILES,¹⁵⁶ M. RIZZO,¹⁵ N. A. ROBERTSON,^{1, 54} F. ROBINET,³¹ A. ROCCHI,³⁶ J. A. ROCHA,³⁰ S. RODRIGUEZ,³⁰
R. D. RODRIGUEZ-SOTO,²⁸ L. ROLLAND,³⁸ J. G. ROLLINS,¹ V. J. ROMA,⁴³ M. ROMANELLI,⁸³ R. ROMANO,^{4, 5}
C. L. ROMEL,⁵⁰ A. ROMERO,⁷⁸ I. M. ROMERO-SHAW,⁶ J. H. ROMIE,⁸ S. RONCHINI,^{17, 18} C. A. ROSE,²⁴ D. ROSE,³⁰
K. ROSE,¹⁹⁵ M. J. B. ROSELL,¹⁸⁵ D. ROSIŃSKA,⁸⁶ S. G. ROSOFKY,²² M. P. ROSS,¹⁷⁹ S. ROWAN,⁵⁴ S. J. ROWLINSON,¹⁴
SANTOSH ROY,³ SOUMEN ROY,²⁰⁴ P. RUGGI,³² K. RYAN,⁵⁰ S. SACHDEV,¹⁴⁰ T. SADECKI,⁵⁰ M. SAKELLARIADOU,¹¹³
O. S. SALAFIA,^{49, 48, 47} L. SALCONI,³² M. SALEEM,³⁴ A. SAMAJDAR,^{40, 155} E. J. SANCHEZ,¹ J. H. SANCHEZ,³⁰
L. E. SANCHEZ,¹ N. SANCHIS-GUAL,²⁰⁵ J. R. SANDERS,²⁰⁶ K. A. SANTIAGO,³⁹ E. SANTOS,⁷⁵ T. R. SARAVANAN,³
N. SARIN,⁶ B. SASSOLAS,¹³¹ B. S. SATHYAPRAKASH,^{140, 100} O. SAUTER,³⁸ R. L. SAVAGE,⁵⁰ V. SAVANT,³ D. SAWANT,¹⁰⁴
S. SAYAH,¹³¹ D. SCHAETZL,¹ P. SCHALE,⁴³ M. SCHEEL,⁷⁶ J. SCHEUER,¹⁵ A. SCHINDLER-TYKA,³³ P. SCHMIDT,¹⁴
R. SCHNABEL,¹²⁸ R. M. S. SCHOFIELD,⁴³ A. SCHÖNBECK,¹²⁸ E. SCHREIBER,^{10, 11} B. W. SCHULTE,^{10, 11}
B. F. SCHUTZ,^{100, 10} O. SCHWARM,¹⁹⁶ E. SCHWARTZ,¹⁰⁰ J. SCOTT,⁵⁴ S. M. SCOTT,⁹ M. SEGLAR-ARROYO,³⁸
E. SEIDEL,²² D. SELLERS,⁸ A. S. SENGUPTA,²⁰⁴ N. SENNETT,⁸⁸ D. SENTENAC,³² V. SEQUINO,^{93, 5} A. SERGEEV,¹⁶⁵
Y. SETYAWATI,^{10, 11} T. SHAFFER,⁵⁰ M. S. SHAHRIAR,¹⁵ S. SHARIFI,² A. SHARMA,^{17, 18} P. SHARMA,⁶⁸ P. SHAWHAN,⁸⁹
H. SHEN,²² M. SHIKAUCHI,⁹⁶ R. SHINK,¹⁷⁵ D. H. SHOEMAKER,⁵² D. M. SHOEMAKER,⁹⁰ K. SHUKLA,¹⁵⁹
S. SHYAMSUNDAR,⁶⁸ M. SIENIAWSKA,⁶⁴ D. SIGG,⁵⁰ L. P. SINGER,⁹⁴ D. SINGH,¹⁴⁰ N. SINGH,⁸⁶ A. SINGHA,¹²⁷
A. SINGHAL,^{17, 37} A. M. SINTES,¹¹⁸ V. SIPALA,^{98, 99} V. SKLIRIS,¹⁰⁰ B. J. J. SLAGMOLEN,⁹ T. J. SLAVEN-BLAIR,⁷⁷
J. SMETANA,¹⁴ J. R. SMITH,³⁰ R. J. E. SMITH,⁶ S. N. SOMALA,²⁰⁷ E. J. SON,¹⁶⁹ S. SONI,² B. SORAZU,⁵⁴
V. SORDINI,¹¹⁰ F. SORRENTINO,⁶⁷ N. SORRENTINO,^{20, 19} R. SOULARD,⁷⁵ T. SOURADEEP,^{202, 3} E. SOWELL,¹²¹
A. P. SPENCER,⁵⁴ M. SPERA,^{59, 60, 15} A. K. SRIVASTAVA,⁶³ V. SRIVASTAVA,⁴⁴ K. STAATS,¹⁵ C. STACHIE,⁷⁵
D. A. STEER,²⁹ M. STEINKE,^{10, 11} J. STEINLECHNER,^{127, 54} S. STEINLECHNER,¹²⁷ D. STEINMEYER,^{10, 11}
S. P. STEVENSON,¹⁰⁷ G. STOLLE-McALLISTER,¹⁹⁵ D. J. STOPS,¹⁴ M. STOVER,¹⁹⁵ K. A. STRAIN,⁵⁴ G. STRATTA,^{208, 74}
A. STRUNK,⁵⁰ R. STURANI,²⁰⁹ A. L. STUVER,⁹¹ J. SÜDBECK,¹²⁸ S. SUDHAGAR,³ V. SUDHIR,⁵² H. G. SUH,²⁴
T. Z. SUMMERSCALES,²¹⁰ H. SUN,⁷⁷ L. SUN,¹ S. SUNIL,⁶³ A. SUR,⁶⁴ J. SURESH,⁹⁶ P. J. SUTTON,¹⁰⁰ B. L. SWINKELS,⁴⁰
M. J. SZCZEPAŃCZYK,³³ M. TACCA,⁴⁰ S. C. TAIT,⁵⁴ C. TALBOT,⁶ A. J. TANASIJCZUK,⁸⁵ D. B. TANNER,³³ D. TAO,¹
A. TAPIA,³⁰ E. N. TAPIA SAN MARTIN,⁴⁰ J. D. TASSON,¹⁵⁸ R. TAYLOR,¹ R. TENORIO,¹¹⁸ L. TERKOWSKI,¹²⁸
M. P. THIRUGNANASAMBANDAM,³ L. THOMAS,¹⁴ M. THOMAS,⁸ P. THOMAS,⁵⁰ J. E. THOMPSON,¹⁰⁰ S. R. THONDAPU,⁶⁸

K. A. THORNE,⁸ E. THRANE,⁶ SHUBHANSHU TIWARI,⁸¹ SRISHTI TIWARI,¹⁵³ V. TIWARI,¹⁰⁰ K. TOLAND,⁵⁴
 A. E. TOLLEY,¹³⁸ M. TONELLI,^{20,19} Z. TORNASI,⁵⁴ A. TORRES-FORNÉ,⁸⁸ C. I. TORRIE,¹ I. TOSTA E MELO,^{98,99}
 D. TÖYRÄ,⁹ A. T. TRAN,¹²⁴ A. TRAPANANTI,^{183,57} F. TRAVASSO,^{57,183} G. TRAYLOR,⁸ M. C. TRINGALI,⁸⁶
 A. TRIPATHEE,¹⁵⁶ A. TROVATO,²⁹ R. J. TRUDEAU,¹ D. S. TSAI,¹⁰⁵ K. W. TSANG,^{40,211,155} M. TSE,⁵² R. TSO,⁷⁶
 L. TSUKADA,⁹⁶ D. TSUNA,⁹⁶ T. TSUTSUI,⁹⁶ M. TURCONI,⁷⁵ A. S. UBHI,¹⁴ R. P. UDALL,⁹⁰ K. UENO,⁹⁶ D. UGOLINI,²⁰¹
 C. S. UNNIKRISSNAN,¹⁵³ A. L. URBAN,² S. A. USMAN,¹⁰⁸ A. C. UTINA,¹²⁷ H. VAHLBRUCH,^{10,11} G. VAJENTE,¹
 A. VAJPEYI,⁶ G. VALDES,² M. VALENTINI,^{136,137} V. VALSAN,²⁴ N. VAN BAKEL,⁴⁰ M. VAN BEUZekom,⁴⁰
 J. F. J. VAN DEN BRAND,^{171,87,40} C. VAN DEN BROECK,^{155,40} D. C. VANDER-HYDE,⁴⁴ L. VAN DER SCHAAF,⁴⁰
 J. V. VAN HEIJNINGEN,⁷⁷ M. VARDARO,^{177,40} A. F. VARGAS,¹¹⁷ V. VARMA,⁷⁶ S. VASS,¹ M. VASÚTH,⁵⁵ A. VECCHIO,¹⁴
 G. VEDOVATO,⁶⁰ J. VEITCH,⁵⁴ P. J. VEITCH,⁶⁵ K. VENKATESWARA,¹⁷⁹ J. VENNEBERG,^{10,11} G. VENUGOPALAN,¹
 D. VERKINDT,³⁸ Y. VERMA,⁶⁸ D. VESKE,³⁵ F. VETRANO,⁷³ A. VICERÉ,^{73,74} A. D. VIETS,²¹² V. VILLA-ORTEGA,¹²⁹
 J.-Y. VINET,⁷⁵ S. VITALE,⁵² T. VO,⁴⁴ H. VOCCA,^{58,57} C. VORVICK,⁵⁰ S. P. VYATCHANIN,⁷⁰ A. R. WADE,⁹
 L. E. WADE,¹⁹⁵ M. WADE,¹⁹⁵ R. C. WALET,⁴⁰ M. WALKER,⁷ G. S. WALLACE,²⁵ L. WALLACE,¹ S. WALSH,²⁴
 J. Z. WANG,¹⁵⁶ S. WANG,²² W. H. WANG,¹²³ Y. F. WANG,¹⁰³ R. L. WARD,⁹ J. WARNER,⁵⁰ M. WAS,³⁸
 N. Y. WASHINGTON,¹ J. WATCHI,¹¹⁹ B. WEAVER,⁵⁰ L. WEI,^{10,11} M. WEINERT,^{10,11} A. J. WEINSTEIN,¹ R. WEISS,⁵²
 F. WELLMANN,^{10,11} L. WEN,⁷⁷ P. WESSELS,^{10,11} J. W. WESTHOUSE,²⁸ K. WETTE,⁹ J. T. WHELAN,¹³²
 D. D. WHITE,³⁰ L. V. WHITE,⁴⁴ B. F. WHITING,³³ C. WHITTLE,⁵² D. M. WILKEN,^{10,11} D. WILLIAMS,⁵⁴
 M. J. WILLIAMS,⁵⁴ A. R. WILLIAMSON,¹³⁸ J. L. WILLIS,¹ B. WHITKE,^{10,11} D. J. WILSON,¹¹⁵ M. H. WIMMER,^{10,11}
 W. WINKLER,^{10,11} C. C. WIPF,¹ G. WOAN,⁵⁴ J. WOEHLE,^{10,11} J. K. WOFFORD,¹³² I. C. F. WONG,¹⁰³
 J. WRANGEL,^{10,11} J. L. WRIGHT,⁵⁴ D. S. WU,^{10,11} D. M. WYSOCKI,¹³² L. XIAO,¹ H. YAMAMOTO,¹ L. YANG,¹⁴²
 Y. YANG,³³ Z. YANG,⁴⁶ M. J. YAP,⁹ D. W. YEELES,¹⁰⁰ A. YOON,⁷ HANG YU,⁷⁶ HAOCUN YU,⁵² S. H. R. YUEN,¹⁰³
 A. ZADROŻNY,¹⁷³ M. ZANOLIN,²⁸ T. ZELENKOVA,³² J.-P. ZENDRI,⁶⁰ M. ZEVIN,¹⁵ J. ZHANG,⁷⁷ L. ZHANG,¹ R. ZHANG,³³
 T. ZHANG,¹⁴ C. ZHAO,⁷⁷ G. ZHAO,¹¹⁹ M. ZHOU,¹⁵ Z. ZHOU,¹⁵ X. J. ZHU,⁶ A. B. ZIMMERMAN,¹⁸⁵ M. E. ZUCKER,^{1,52}
 AND J. ZWEIZIG¹

THE LIGO SCIENTIFIC COLLABORATION AND THE VIRGO COLLABORATION

¹LIGO, California Institute of Technology, Pasadena, CA 91125, USA

²Louisiana State University, Baton Rouge, LA 70803, USA

³Inter-University Centre for Astronomy and Astrophysics, Pune 411007, India

⁴Dipartimento di Farmacia, Università di Salerno, I-84084 Fisciano, Salerno, Italy

⁵INFN, Sezione di Napoli, Complesso Universitario di Monte S. Angelo, I-80126 Napoli, Italy

⁶OzGrav, School of Physics & Astronomy, Monash University, Clayton 3800, Victoria, Australia

⁷Christopher Newport University, Newport News, VA 23606, USA

⁸LIGO Livingston Observatory, Livingston, LA 70754, USA

⁹OzGrav, Australian National University, Canberra, Australian Capital Territory 0200, Australia

¹⁰Max Planck Institute for Gravitational Physics (Albert Einstein Institute), D-30167 Hannover, Germany

¹¹Leibniz Universität Hannover, D-30167 Hannover, Germany

¹²University of Cambridge, Cambridge CB2 1TN, United Kingdom

¹³Theoretisch-Physikalisches Institut, Friedrich-Schiller-Universität Jena, D-07743 Jena, Germany

¹⁴University of Birmingham, Birmingham B15 2TT, United Kingdom

¹⁵Center for Interdisciplinary Exploration & Research in Astrophysics (CIERA), Northwestern University, Evanston, IL 60208, USA

¹⁶Instituto Nacional de Pesquisas Espaciais, 12227-010 São José dos Campos, São Paulo, Brazil

¹⁷Gran Sasso Science Institute (GSSI), I-67100 L'Aquila, Italy

¹⁸INFN, Laboratori Nazionali del Gran Sasso, I-67100 Assergi, Italy

¹⁹INFN, Sezione di Pisa, I-56127 Pisa, Italy

²⁰Università di Pisa, I-56127 Pisa, Italy

²¹International Centre for Theoretical Sciences, Tata Institute of Fundamental Research, Bengaluru 560089, India

²²NCSA, University of Illinois at Urbana-Champaign, Urbana, IL 61801, USA

²³Université de Lyon, Université Claude Bernard Lyon 1, CNRS, Institut Lumière Matière, F-69622 Villeurbanne, France

²⁴University of Wisconsin-Milwaukee, Milwaukee, WI 53201, USA

²⁵SUPA, University of Strathclyde, Glasgow G1 1XQ, United Kingdom

²⁶Dipartimento di Matematica e Informatica, Università di Udine, I-33100 Udine, Italy

²⁷INFN, Sezione di Trieste, I-34127 Trieste, Italy

²⁸Embry-Riddle Aeronautical University, Prescott, AZ 86301, USA

²⁹Université de Paris, CNRS, Astroparticule et Cosmologie, F-75013 Paris, France

³⁰California State University Fullerton, Fullerton, CA 92831, USA

³¹Université Paris-Saclay, CNRS/IN2P3, IJCLab, 91405 Orsay, France

³²European Gravitational Observatory (EGO), I-56021 Cascina, Pisa, Italy

- ³³ *University of Florida, Gainesville, FL 32611, USA*
- ³⁴ *Chennai Mathematical Institute, Chennai 603103, India*
- ³⁵ *Columbia University, New York, NY 10027, USA*
- ³⁶ *INFN, Sezione di Roma Tor Vergata, I-00133 Roma, Italy*
- ³⁷ *INFN, Sezione di Roma, I-00185 Roma, Italy*
- ³⁸ *Laboratoire d'Annecy de Physique des Particules (LAPP), Univ. Grenoble Alpes, Université Savoie Mont Blanc, CNRS/IN2P3, F-74941 Annecy, France*
- ³⁹ *Montclair State University, Montclair, NJ 07043, USA*
- ⁴⁰ *Nikhef, Science Park 105, 1098 XG Amsterdam, Netherlands*
- ⁴¹ *Korea Institute of Science and Technology Information, Daejeon 34141, South Korea*
- ⁴² *INFN Sezione di Torino, I-10125 Torino, Italy*
- ⁴³ *University of Oregon, Eugene, OR 97403, USA*
- ⁴⁴ *Syracuse University, Syracuse, NY 13244, USA*
- ⁴⁵ *Université de Liège, B-4000 Liège, Belgium*
- ⁴⁶ *University of Minnesota, Minneapolis, MN 55455, USA*
- ⁴⁷ *Università degli Studi di Milano-Bicocca, I-20126 Milano, Italy*
- ⁴⁸ *INFN, Sezione di Milano-Bicocca, I-20126 Milano, Italy*
- ⁴⁹ *INAF, Osservatorio Astronomico di Brera sede di Merate, I-23807 Merate, Lecco, Italy*
- ⁵⁰ *LIGO Hanford Observatory, Richland, WA 99352, USA*
- ⁵¹ *Institut de Ciències del Cosmos, Universitat de Barcelona, C/ Martí i Franquès 1, Barcelona, 08028, Spain*
- ⁵² *LIGO, Massachusetts Institute of Technology, Cambridge, MA 02139, USA*
- ⁵³ *Dipartimento di Medicina, Chirurgia e Odontoiatria "Scuola Medica Salernitana," Università di Salerno, I-84081 Baronissi, Salerno, Italy*
- ⁵⁴ *SUPA, University of Glasgow, Glasgow G12 8QQ, United Kingdom*
- ⁵⁵ *Wigner RCP, RMKI, H-1121 Budapest, Konkoly Thege Miklós út 29-33, Hungary*
- ⁵⁶ *Stanford University, Stanford, CA 94305, USA*
- ⁵⁷ *INFN, Sezione di Perugia, I-06123 Perugia, Italy*
- ⁵⁸ *Università di Perugia, I-06123 Perugia, Italy*
- ⁵⁹ *Università di Padova, Dipartimento di Fisica e Astronomia, I-35131 Padova, Italy*
- ⁶⁰ *INFN, Sezione di Padova, I-35131 Padova, Italy*
- ⁶¹ *Bard College, 30 Campus Rd, Annandale-On-Hudson, NY 12504, USA*
- ⁶² *Montana State University, Bozeman, MT 59717, USA*
- ⁶³ *Institute for Plasma Research, Bhat, Gandhinagar 382428, India*
- ⁶⁴ *Nicolaus Copernicus Astronomical Center, Polish Academy of Sciences, 00-716, Warsaw, Poland*
- ⁶⁵ *OzGrav, University of Adelaide, Adelaide, South Australia 5005, Australia*
- ⁶⁶ *California State University, Los Angeles, 5151 State University Dr, Los Angeles, CA 90032, USA*
- ⁶⁷ *INFN, Sezione di Genova, I-16146 Genova, Italy*
- ⁶⁸ *RRCAT, Indore, Madhya Pradesh 452013, India*
- ⁶⁹ *Missouri University of Science and Technology, Rolla, MO 65409, USA*
- ⁷⁰ *Faculty of Physics, Lomonosov Moscow State University, Moscow 119991, Russia*
- ⁷¹ *SUPA, University of the West of Scotland, Paisley PA1 2BE, United Kingdom*
- ⁷² *Bar-Ilan University, Ramat Gan, 5290002, Israel*
- ⁷³ *Università degli Studi di Urbino "Carlo Bo", I-61029 Urbino, Italy*
- ⁷⁴ *INFN, Sezione di Firenze, I-50019 Sesto Fiorentino, Firenze, Italy*
- ⁷⁵ *Artemis, Université Côte d'Azur, Observatoire Côte d'Azur, CNRS, F-06304 Nice, France*
- ⁷⁶ *Caltech CaRT, Pasadena, CA 91125, USA*
- ⁷⁷ *OzGrav, University of Western Australia, Crawley, Western Australia 6009, Australia*
- ⁷⁸ *Institut de Física d'Altes Energies (IFAE), Barcelona Institute of Science and Technology, and ICREA, E-08193 Barcelona, Spain*
- ⁷⁹ *Dipartimento di Fisica "E.R. Caianiello," Università di Salerno, I-84084 Fisciano, Salerno, Italy*
- ⁸⁰ *INFN, Sezione di Napoli, Gruppo Collegato di Salerno, Complesso Universitario di Monte S. Angelo, I-80126 Napoli, Italy*
- ⁸¹ *Physik-Institut, University of Zurich, Winterthurerstrasse 190, 8057 Zurich, Switzerland*
- ⁸² *Università di Roma "La Sapienza", I-00185 Roma, Italy*
- ⁸³ *Univ Rennes, CNRS, Institut FOTON - UMR6082, F-3500 Rennes, France*
- ⁸⁴ *Laboratoire Kastler Brossel, Sorbonne Université, CNRS, ENS-Université PSL, Collège de France, F-75005 Paris, France*
- ⁸⁵ *Université catholique de Louvain, B-1348 Louvain-la-Neuve, Belgium*
- ⁸⁶ *Astronomical Observatory Warsaw University, 00-478 Warsaw, Poland*
- ⁸⁷ *VU University Amsterdam, 1081 HV Amsterdam, Netherlands*
- ⁸⁸ *Max Planck Institute for Gravitational Physics (Albert Einstein Institute), D-14476 Potsdam-Golm, Germany*

- ⁸⁹ *University of Maryland, College Park, MD 20742, USA*
- ⁹⁰ *School of Physics, Georgia Institute of Technology, Atlanta, GA 30332, USA*
- ⁹¹ *Villanova University, 800 Lancaster Ave, Villanova, PA 19085, USA*
- ⁹² *Center for Computational Astrophysics, Flatiron Institute, New York, NY 10010, USA*
- ⁹³ *Università di Napoli "Federico II", Complesso Universitario di Monte S. Angelo, I-80126 Napoli, Italy*
- ⁹⁴ *NASA Goddard Space Flight Center, Greenbelt, MD 20771, USA*
- ⁹⁵ *Dipartimento di Fisica, Università degli Studi di Genova, I-16146 Genova, Italy*
- ⁹⁶ *RESCEU, University of Tokyo, Tokyo, 113-0033, Japan.*
- ⁹⁷ *Tsinghua University, Beijing 100084, China*
- ⁹⁸ *Università degli Studi di Sassari, I-07100 Sassari, Italy*
- ⁹⁹ *INFN, Laboratori Nazionali del Sud, I-95125 Catania, Italy*
- ¹⁰⁰ *Gravity Exploration Institute, Cardiff University, Cardiff CF24 3AA, United Kingdom*
- ¹⁰¹ *Università di Roma Tor Vergata, I-00133 Roma, Italy*
- ¹⁰² *Departamento de Astronomía y Astrofísica, Universitat de València, E-46100 Burjassot, València, Spain*
- ¹⁰³ *The Chinese University of Hong Kong, Shatin, NT, Hong Kong*
- ¹⁰⁴ *Indian Institute of Technology Bombay, Powai, Mumbai 400 076, India*
- ¹⁰⁵ *National Tsing Hua University, Hsinchu City, 30013 Taiwan, Republic of China*
- ¹⁰⁶ *Charles Sturt University, Wagga Wagga, New South Wales 2678, Australia*
- ¹⁰⁷ *OzGrav, Swinburne University of Technology, Hawthorn VIC 3122, Australia*
- ¹⁰⁸ *University of Chicago, Chicago, IL 60637, USA*
- ¹⁰⁹ *Dipartimento di Ingegneria Industriale (DIIN), Università di Salerno, I-84084 Fisciano, Salerno, Italy*
- ¹¹⁰ *Institut de Physique des 2 Infinis de Lyon, CNRS/IN2P3, Université de Lyon, Université Claude Bernard Lyon 1, F-69622 Villeurbanne, France*
- ¹¹¹ *Seoul National University, Seoul 08826, South Korea*
- ¹¹² *Pusan National University, Busan 46241, South Korea*
- ¹¹³ *King's College London, University of London, London WC2R 2LS, United Kingdom*
- ¹¹⁴ *INAF, Osservatorio Astronomico di Padova, I-35122 Padova, Italy*
- ¹¹⁵ *University of Arizona, Tucson, AZ 85721, USA*
- ¹¹⁶ *Rutherford Appleton Laboratory, Didcot OX11 0DE, United Kingdom*
- ¹¹⁷ *OzGrav, University of Melbourne, Parkville, Victoria 3010, Australia*
- ¹¹⁸ *Universitat de les Illes Balears, IAC3—IEEC, E-07122 Palma de Mallorca, Spain*
- ¹¹⁹ *Université Libre de Bruxelles, Brussels 1050, Belgium*
- ¹²⁰ *Departamento de Matemáticas, Universitat de València, E-46100 Burjassot, València, Spain*
- ¹²¹ *Texas Tech University, Lubbock, TX 79409, USA*
- ¹²² *University of Rhode Island, Kingston, RI 02881, USA*
- ¹²³ *The University of Texas Rio Grande Valley, Brownsville, TX 78520, USA*
- ¹²⁴ *Bellevue College, Bellevue, WA 98007, USA*
- ¹²⁵ *Scuola Normale Superiore, Piazza dei Cavalieri, 7 - 56126 Pisa, Italy*
- ¹²⁶ *MTA-ELTE Astrophysics Research Group, Institute of Physics, Eötvös University, Budapest 1117, Hungary*
- ¹²⁷ *Maastricht University, 6200 MD, Maastricht, Netherlands*
- ¹²⁸ *Universität Hamburg, D-22761 Hamburg, Germany*
- ¹²⁹ *IGFAE, Campus Sur, Universidade de Santiago de Compostela, 15782 Spain*
- ¹³⁰ *The University of Sheffield, Sheffield S10 2TN, United Kingdom*
- ¹³¹ *Laboratoire des Matériaux Avancés (LMA), Institut de Physique des 2 Infinis de Lyon, CNRS/IN2P3, Université de Lyon, F-69622 Villeurbanne, France*
- ¹³² *Rochester Institute of Technology, Rochester, NY 14623, USA*
- ¹³³ *Dipartimento di Scienze Matematiche, Fisiche e Informatiche, Università di Parma, I-43124 Parma, Italy*
- ¹³⁴ *INFN, Sezione di Milano Bicocca, Gruppo Collegato di Parma, I-43124 Parma, Italy*
- ¹³⁵ *Dipartimento di Ingegneria, Università del Sannio, I-82100 Benevento, Italy*
- ¹³⁶ *Università di Trento, Dipartimento di Fisica, I-38123 Povo, Trento, Italy*
- ¹³⁷ *INFN, Trento Institute for Fundamental Physics and Applications, I-38123 Povo, Trento, Italy*
- ¹³⁸ *University of Portsmouth, Portsmouth, PO1 3FX, United Kingdom*
- ¹³⁹ *West Virginia University, Morgantown, WV 26506, USA*
- ¹⁴⁰ *The Pennsylvania State University, University Park, PA 16802, USA*
- ¹⁴¹ *Stony Brook University, Stony Brook, NY 11794, USA*
- ¹⁴² *Colorado State University, Fort Collins, CO 80523, USA*
- ¹⁴³ *Institute for Nuclear Research, Hungarian Academy of Sciences, Bem t'er 18/c, H-4026 Debrecen, Hungary*

- ¹⁴⁴ *CNR-SPIN, c/o Università di Salerno, I-84084 Fisciano, Salerno, Italy*
- ¹⁴⁵ *Scuola di Ingegneria, Università della Basilicata, I-85100 Potenza, Italy*
- ¹⁴⁶ *National Astronomical Observatory of Japan, 2-21-1 Osawa, Mitaka, Tokyo 181-8588, Japan*
- ¹⁴⁷ *Observatori Astronòmic, Universitat de València, E-46980 Paterna, València, Spain*
- ¹⁴⁸ *University of Szeged, Dóm tér 9, Szeged 6720, Hungary*
- ¹⁴⁹ *GRAPPA, Anton Pannekoek Institute for Astronomy and Institute for High-Energy Physics, University of Amsterdam, Science Park 904, 1098 XH Amsterdam, Netherlands*
- ¹⁵⁰ *Delta Institute for Theoretical Physics, Science Park 904, 1090 GL Amsterdam, Netherlands*
- ¹⁵¹ *Lorentz Institute, Leiden University, Niels Bohrweg 2, 2333 CA Leiden, Netherlands*
- ¹⁵² *University of British Columbia, Vancouver, BC V6T 1Z4, Canada*
- ¹⁵³ *Tata Institute of Fundamental Research, Mumbai 400005, India*
- ¹⁵⁴ *INAF, Osservatorio Astronomico di Capodimonte, I-80131 Napoli, Italy*
- ¹⁵⁵ *Department of Physics, Utrecht University, Princetonplein 1, 3584 CC Utrecht, Netherlands*
- ¹⁵⁶ *University of Michigan, Ann Arbor, MI 48109, USA*
- ¹⁵⁷ *American University, Washington, D.C. 20016, USA*
- ¹⁵⁸ *Carleton College, Northfield, MN 55057, USA*
- ¹⁵⁹ *University of California, Berkeley, CA 94720, USA*
- ¹⁶⁰ *Directorate of Construction, Services & Estate Management, Mumbai 400094 India*
- ¹⁶¹ *Universiteit Antwerpen, Prinsstraat 13, 2000 Antwerpen, Belgium*
- ¹⁶² *University of Bialystok, 15-424 Bialystok, Poland*
- ¹⁶³ *University of Southampton, Southampton SO17 1BJ, United Kingdom*
- ¹⁶⁴ *University of Washington Bothell, Bothell, WA 98011, USA*
- ¹⁶⁵ *Institute of Applied Physics, Nizhny Novgorod, 603950, Russia*
- ¹⁶⁶ *Ewha Womans University, Seoul 03760, South Korea*
- ¹⁶⁷ *Inje University Gimhae, South Gyeongsang 50834, South Korea*
- ¹⁶⁸ *Korea Astronomy and Space Science Institute, Daejeon 34055, South Korea*
- ¹⁶⁹ *National Institute for Mathematical Sciences, Daejeon 34047, South Korea*
- ¹⁷⁰ *Ulsan National Institute of Science and Technology, Ulsan 44919, South Korea*
- ¹⁷¹ *Maastricht University, P.O. Box 616, 6200 MD Maastricht, Netherlands*
- ¹⁷² *Institute of Mathematics, Polish Academy of Sciences, 00656 Warsaw, Poland*
- ¹⁷³ *National Center for Nuclear Research, 05-400 Świerk-Otwock, Poland*
- ¹⁷⁴ *Cornell University, Ithaca, NY 14850, USA*
- ¹⁷⁵ *Université de Montréal/Polytechnique, Montreal, Quebec H3T 1J4, Canada*
- ¹⁷⁶ *Laboratoire Lagrange, Université Côte d'Azur, Observatoire Côte d'Azur, CNRS, F-06304 Nice, France*
- ¹⁷⁷ *Institute for High-Energy Physics, University of Amsterdam, Science Park 904, 1098 XH Amsterdam, Netherlands*
- ¹⁷⁸ *NASA Marshall Space Flight Center, Huntsville, AL 35811, USA*
- ¹⁷⁹ *University of Washington, Seattle, WA 98195, USA*
- ¹⁸⁰ *Dipartimento di Matematica e Fisica, Università degli Studi Roma Tre, I-00146 Roma, Italy*
- ¹⁸¹ *INFN, Sezione di Roma Tre, I-00146 Roma, Italy*
- ¹⁸² *ESPCI, CNRS, F-75005 Paris, France*
- ¹⁸³ *Università di Camerino, Dipartimento di Fisica, I-62032 Camerino, Italy*
- ¹⁸⁴ *Southern University and A&M College, Baton Rouge, LA 70813, USA*
- ¹⁸⁵ *Department of Physics, University of Texas, Austin, TX 78712, USA*
- ¹⁸⁶ *Department of Physics, Smith College, Northampton, MA 01063, USA*
- ¹⁸⁷ *Dipartimento di Fisica, Università di Trieste, I-34127 Trieste, Italy*
- ¹⁸⁸ *Centre Scientifique de Monaco, 8 quai Antoine 1er, MC-98000, Monaco*
- ¹⁸⁹ *Indian Institute of Technology Madras, Chennai 600036, India*
- ¹⁹⁰ *Institut Pluridisciplinaire Hubert CURIE, 23 rue du loess - BP28 67037 Strasbourg cedex 2, France*
- ¹⁹¹ *Museo Storico della Fisica e Centro Studi e Ricerche "Enrico Fermi", I-00184 Roma, Italy*
- ¹⁹² *Institut des Hautes Etudes Scientifiques, F-91440 Bures-sur-Yvette, France*
- ¹⁹³ *Indian Institute of Science Education and Research, Kolkata, Mohanpur, West Bengal 741252, India*
- ¹⁹⁴ *Department of Astrophysics/IMAPP, Radboud University Nijmegen, P.O. Box 9010, 6500 GL Nijmegen, Netherlands*
- ¹⁹⁵ *Kenyon College, Gambier, OH 43022, USA*
- ¹⁹⁶ *Whitman College, 345 Boyer Avenue, Walla Walla, WA 99362 USA*
- ¹⁹⁷ *Consiglio Nazionale delle Ricerche - Istituto dei Sistemi Complessi, Piazzale Aldo Moro 5, I-00185 Roma, Italy*
- ¹⁹⁸ *Hobart and William Smith Colleges, Geneva, NY 14456, USA*
- ¹⁹⁹ *Lancaster University, Lancaster LA1 4YW, United Kingdom*

²⁰⁰ *Università di Trento, Dipartimento di Matematica, I-38123 Povo, Trento, Italy*

²⁰¹ *Trinity University, San Antonio, TX 78212, USA*

²⁰² *Indian Institute of Science Education and Research, Pune, Maharashtra 411008, India*

²⁰³ *Dipartimento di Fisica, Università degli Studi di Torino, I-10125 Torino, Italy*

²⁰⁴ *Indian Institute of Technology, Palaj, Gandhinagar, Gujarat 382355, India*

²⁰⁵ *Centro de Astrofísica e Gravitação (CENTRA), Departamento de Física, Instituto Superior Técnico, Universidade de Lisboa, 1049-001 Lisboa, Portugal*

²⁰⁶ *Marquette University, 11420 W. Clybourn St., Milwaukee, WI 53233, USA*

²⁰⁷ *Indian Institute of Technology Hyderabad, Sangareddy, Khandi, Telangana 502285, India*

²⁰⁸ *INAF, Osservatorio di Astrofisica e Scienza dello Spazio, I-40129 Bologna, Italy*

²⁰⁹ *International Institute of Physics, Universidade Federal do Rio Grande do Norte, Natal RN 59078-970, Brazil*

²¹⁰ *Andrews University, Berrien Springs, MI 49104, USA*

²¹¹ *Van Swinderen Institute for Particle Physics and Gravity, University of Groningen, Nijenborgh 4, 9747 AG Groningen, Netherlands*

²¹² *Concordia University Wisconsin, Mequon, WI 53097, USA*

ABSTRACT

We report on the population of the 47 compact binary mergers detected with a false-alarm rate $< 1 \text{ yr}^{-1}$ in the second LIGO–Virgo Gravitational-Wave Transient Catalog, GWTC-2. We observe several characteristics of the merging binary black hole (BBH) population not discernible until now. First, the primary mass spectrum contains structure beyond a power-law with a sharp high-mass cut-off; it is more consistent with a *broken* power law with a break at $39.7^{+20.3}_{-9.1} M_{\odot}$, or a power law with a Gaussian feature peaking at $33.1^{+4.0}_{-5.6} M_{\odot}$ (90% credible interval). While the primary mass distribution must extend to $\sim 65 M_{\odot}$ or beyond, only $2.9^{+3.5}_{-1.7}\%$ of systems have primary masses greater than $45 M_{\odot}$. Second, we find that a fraction of BBH systems have component spins misaligned with the orbital angular momentum, giving rise to precession of the orbital plane. Moreover, 12% to 44% of BBH systems have spins tilted by more than 90° , giving rise to a negative effective inspiral spin parameter χ_{eff} . Under the assumption that such systems can only be formed by dynamical interactions, we infer that between 25% and 93% of BBH with non-vanishing $|\chi_{\text{eff}}| > 0.01$ are dynamically assembled. Third, we estimate merger rates, finding $\mathcal{R}_{\text{BBH}} = 23.9^{+14.3}_{-8.6} \text{ Gpc}^{-3} \text{ yr}^{-1}$ for BBH and $\mathcal{R}_{\text{BNS}} = 320^{+490}_{-240} \text{ Gpc}^{-3} \text{ yr}^{-1}$ for binary neutron stars. We find that the BBH rate likely increases with redshift (85% credibility), but not faster than the star-formation rate (86% credibility). Additionally, we examine recent exceptional events in the context of our population models, finding that the asymmetric masses of GW190412 and the high component masses of GW190521 are consistent with our models, but the low secondary mass of GW190814 makes it an outlier.

Keywords: gravitational waves

1. INTRODUCTION

We analyze the population properties of black holes (BHs) and neutron stars (NSs) in compact binary systems using data from the LIGO–Virgo Gravitational-wave Transient Catalog 2 (GWTC-2; Abbott et al. 2020c). The GWTC-2 catalog combines observations from the first two observing runs (O1 and O2; Abbott et al. 2019b) and the first half of the third observing run (O3a; Abbott et al. 2020c) of the Advanced LIGO (Aasi et al. 2015) and Advanced Virgo (Acernese et al. 2015) gravitational-wave observatories. With the 39 additional candidates from O3a, we have more than quadrupled the number of events from O1 and O2, published in the first LIGO–Virgo Transient Catalog (GWTC-1; Abbott et al. 2019b). Counting only events with false alarm rate (FAR) $< 1 \text{ yr}^{-1}$ (as opposed to the less conservative FAR threshold of $< 2 \text{ yr}^{-1}$

in GWTC-2), the new combined catalog includes: two binary NS (BNS) events, 44 confident binary black hole (BBH) events, and one NS–BH (NSBH) candidate, which may be a BBH—a topic we discuss below. We define BBH events as systems where both masses are above $3 M_{\odot}$ at 90% credibility. These 47 events are listed in Table 1. Our chosen FAR threshold ensures a relatively pure sample with only ~ 1 noise event (see Section 2) and excludes three marginal triggers presented in GWTC-2. Two of these excluded events are BBH candidates (GW190719_215514 and GW190909_114149) and one is an NSBH candidate (GW190426_152155).

The latest observations include a number of individually remarkable events, which invite theoretical speculation while providing challenges to existing models. The observation of high-mass binaries such as

GW190521 (Abbott et al. 2020e), which has a primary mass $m_1 \sim 85 M_\odot$, is in tension with the sharp mass cutoff $m_{\max} = 40.8^{+11.8}_{-4.4} M_\odot$ inferred from the GWTC-1 detections, forcing us to reconsider models for the distribution of black hole (BH) masses in binary systems (Abbott et al. 2020e,f). Here and in the following, the primary mass m_1 refers to the bigger of the two component masses in the binary, while the secondary mass m_2 refers to the smaller of the two. Along with GW190521, GW190602_175927 and GW190519_153544 also have primary masses above $45 M_\odot$ at $> 99\%$ credibility. These high-mass binaries are interesting from a theoretical perspective since they occur in the predicted pair-instability gap (Barkat et al. 1967; Fowler & Hoyle 1964; Heger & Woosley 2002; Heger et al. 2003; Woosley & Heger 2015; Belczynski et al. 2016). Additionally, GWTC-2 includes the first systems with confidently asymmetric component masses, including GW190412 with mass ratio $m_2/m_1 \equiv q = 0.28^{+0.12}_{-0.06}$ (Abbott et al. 2020a) and GW190814 (Abbott et al. 2020b), with $q = 0.112^{+0.008}_{-0.009}$. Furthermore, the secondary mass of GW190814, $m_2 = 2.59^{+0.08}_{-0.09} M_\odot$, is near the purported NS–BH gap (Bailyn et al. 1998; Özel et al. 2011; Farr et al. 2011), posing a challenge to our understanding of binary formation (Abbott et al. 2020b; Zevin et al. 2020; Mandel et al. 2021). We can gain insight into these exceptional events by studying them in the context of the larger population of compact binaries (Fishbach et al. 2020b).

In particular, studying the enlarged population of BBH events enables us to investigate how compact binaries form.¹ Several evolutionary channels have been proposed to explain the origin of the compact binary mergers observed with Advanced LIGO and Advanced Virgo. The isolated binary channel may occur via common envelope evolution (e.g., Bethe & Brown 1998; Portegies Zwart & Yungelson 1998; Belczynski et al. 2002; Dominik et al. 2015), the remnants of Population III stars (e.g., Madau & Rees 2001; Inayoshi et al. 2017), or chemically homogeneous stellar evolution (e.g., Marchant et al. 2016; de Mink & Mandel 2016; Mandel & de Mink 2016). Evolution via common envelope predicts BBH systems with component masses up to $\sim 50 M_\odot$, mass ratios in the range $0.3 \lesssim q < 1$, and nearly aligned spins (Kalogera 2000; Mandel & O’Shaughnessy 2010; Dominik et al. 2013; Giacobbo et al. 2017; Eldridge et al. 2017; Olejak et al. 2020).

In the chemically homogeneous scenario, BBH systems are expected to form with nearly equal mass components, in addition to aligned spins and component masses in the range $\sim 20\text{--}50 M_\odot$. In isolated formation scenarios, component BHs form via stellar collapse, and are thus not expected to occur within the pair-instability mass gap, $\sim 50\text{--}120 M_\odot$, but may populate either side of the gap.

Alternatively, BBH mergers could form via dynamical interactions in young stellar clusters, globular clusters, or nuclear star clusters (e.g., Kulkarni et al. 1993; Sigurdsson & Hernquist 1993; Portegies Zwart & McMillan 2000), triple systems (e.g. Antonini et al. 2014; Kimpson et al. 2016; Antonini et al. 2017; Vigna-Gómez et al. 2020) or the disks of active galactic nuclei (e.g. McKernan et al. 2012; Bartos et al. 2017; Stone et al. 2017; Fragione et al. 2019). Dynamical formation in dense stellar clusters typically produces an isotropic distribution of spin directions (e.g. Vitale et al. 2017b; Rodriguez et al. 2016), and may enable hierarchical mergers characterized by relatively high-mass binaries (e.g. Antonini & Rasio 2016; Mapelli 2016; McKernan et al. 2018; Rodriguez et al. 2018; Arca Sedda et al. 2020) and large BH spins (Fishbach et al. 2017; Gerosa & Berti 2017). Finally, BBH systems might originate as part of a primordial BH population in the early Universe (Carr & Hawking 1974; Carr et al. 2016). Most primordial BH models predict low spins and isotropic spin orientation (Fernandez & Profumo 2019).

Before we continue, we summarize key questions addressed in the previous analysis of GWTC-1 data (Abbott et al. 2019a) and how the inclusion of O3a events affects our findings:

1. *Are there BBH systems with component masses $\gtrsim 45 M_\odot$?* Following O1 and O2, we inferred that 99% of BBH systems have primary mass below $m_{99\%} \approx 45 M_\odot$. Moreover, this limit was consistent with a sharp cutoff at $m_{\max} = 40.8^{+11.8}_{-4.4} M_\odot$, hypothesized to correspond to the lower edge of the pair-instability mass gap expected from supernova theory (Woosley & Heger 2015; Heger & Woosley 2002; Heger et al. 2003; Fishbach & Holz 2017; Talbot & Thrane 2018). While the GWTC-2 events remain consistent with $97.1^{+1.7}_{-3.5} \%$ of BBH systems having primary masses below $45 M_\odot$ (inferred using the the POWER LAW + PEAK mass model described in Section 3, or “Model C” from Abbott et al. 2019a), high-mass detections such as GW190521, GW190602_175927 and GW190519_153544 imply a non-zero rate of BBH mergers beyond the $\sim 45 M_\odot$ mass limit. We infer that the merger rate for systems with primary masses in the range

¹ For the sake of brevity, we refer throughout to “BBHs” when we really mean “merging BBHs.” It is possible that non-merging BBHs have different properties from those that merge.

$45 M_{\odot} < m_1 < 100 M_{\odot}$ is $0.70^{+0.65}_{-0.35} \text{ Gpc}^{-3} \text{ yr}^{-1}$, consistent with estimates inferred from GWTC-1 (Fishbach et al. 2020b).

2. *Is there a preference for nearly equal component masses?* All of the GWTC-1 observations are consistent with equal-mass binaries, with mass ratios $q \equiv m_2/m_1 = 1$. In O3a, however, we detected two events with mass ratios bounded confidently away from unity: GW190814 and GW190412, though, most binaries are consistent with equal-mass. The NSBH candidate GW190426_152155, if real, also has unequal component masses $q = 0.25^{+0.41}_{-0.15}$, but is above the FAR threshold for this work.
3. *Does the merger rate evolve with redshift?* From GWTC-1 we inferred that the BBH merger rate is $53.2^{+55.8}_{-28.2} \text{ Gpc}^{-3} \text{ yr}^{-1}$, assuming a rate density that is uniform in comoving volume. Allowing for a rate that evolves with redshift (Fishbach et al. 2018), we found that the local merger rate is $\mathcal{R}_{\text{BBH}}(z=0) = 19.7^{+57.3}_{-15.9} \text{ Gpc}^{-3} \text{ yr}^{-1}$, and that, while still consistent with a uniform-in-comoving volume model, the rate density is likely increasing with redshift with 93% credibility (Abbott et al. 2019a). With GWTC-2, we are able to more tightly bound the BBH merger rate at $\mathcal{R}_{\text{BBH}} = 23.9^{+14.3}_{-8.6} \text{ Gpc}^{-3} \text{ yr}^{-1}$ (assuming the POWER LAW + PEAK mass model and a constant-in-comoving-volume merger rate), as well as its evolution with redshift. The data remain consistent with a merger rate that does not evolve with redshift, but prefer a rate that increases with redshift (85% credibility). Using the POWER LAW redshift evolution model of Section 3, we find that the merger rate evolves slower than the naive expectation of $(1+z)^{2.7}$ from the local ($z \lesssim 1$) star formation rate (SFR; Madau & Dickinson 2014) at 86% credibility.
4. *How fast do black holes spin?* From GWTC-1, we inferred that the BH spin component aligned with the orbital angular momentum is typically small (Abbott et al. 2016a; Farr et al. 2017; Farr et al. 2018; Tiwari et al. 2018; Abbott et al. 2019a; Wysocki et al. 2019a; Fernandez & Profumo 2019; Roulet & Zaldarriaga 2019; Miller et al. 2020; Roulet et al. 2020). Among the GWTC-1 events, GW151226 is the only event to exhibit unambiguous signs of spin (Abbott et al. 2016b; Vitale et al. 2017a; Kimball et al. 2020a), while a few other events, including GW170729, show a mild preference for spin (Chatziioannou et al. 2019). We were unable to determine if this typical smallness was

because the spin vectors are misaligned, because the spin magnitudes are small, or both, although the GWTC-1 data weakly disfavors the scenario in which all spins are perfectly aligned (Farr et al. 2017; Tiwari et al. 2018; Abbott et al. 2019a; Biscoveanu et al. 2020). With additional data, we can now say confidently that some BBH systems have spins misaligned with the orbital angular momentum. A nonzero fraction of systems have measurable in-plane spin components, leading them to undergo precession of the orbital plane. Additionally, 12% to 44% of BBH systems merge with a negative effective inspiral spin parameter χ_{eff} , see Eq. (5) below, implying that some component spins are tilted by more than 90° relative to the orbital angular momentum axis. We refer to spins tilted more than 90° as *anti-aligned spins*.² While some events identified in O3a have individually measurable nonzero spin, they occur infrequently, consistent with our previous estimates. We identify nine out of 44 BBH events in GWTC-2 with a positive effective inspiral spin parameter that excludes zero at greater than 95% credibility.³ These nine events include both massive BBH systems like GW190519_153544, with a source primary mass $m_1 = 66.0^{+10.7}_{-12.0} M_{\odot}$ (90% credibility, uniform in redshifted mass prior) and less massive BBH systems like GW190728_064510, with $m_1 = 12.3^{+7.2}_{-2.2} M_{\odot}$. No individual BBH events are observed with confidently negative effective inspiral spin parameter.

5. *What is the minimum black hole mass?* Using GWTC-1, we previously inferred that, if there is a low-mass cut-off in the BBH mass spectrum, it is somewhere below $9 M_{\odot}$ (Abbott et al. 2019a). With GWTC-2, we tighten the constraints on the minimum BH mass in a BBH system, finding $m_{\text{min}} < 6.6 M_{\odot}$ (90% credibility). Furthermore, we find that if the BH mass spectrum extends down to $3 M_{\odot}$, it likely turns over at $\sim 7.8^{+1.8}_{-2.0} M_{\odot}$. This suggests that there may be a dearth of systems between NS and BH masses (Fishbach et al. 2020a). However, the O3a observation of GW190814 (Abbott et al. 2020b), with a sec-

² Our definition of anti-aligned does not imply *perfect* anti-alignment (tilt angles of exactly 180°) as the phrase is sometimes used to mean in the context of waveform modelling or numerical relativity.

³ This result is obtained using a prior informed by the full population of GWTC-2 events. In particular, we employ the GAUSSIAN model described in Section 3.

ondary mass $m_2 = 2.59_{-0.09}^{+0.08} M_\odot$, complicates this picture. If the secondary mass is a BH, it would indicate that the BH mass spectrum extends below $3 M_\odot$, to much lower masses than exhibited by the Galactic X-ray binary population (Bailyn et al. 1998; Özel et al. 2011; Farr et al. 2011, but see also Kreidberg et al. 2012; Thompson et al. 2019; Mandel et al. 2021). Alternatively, the secondary object in GW190814 could be an NS, but it would likely have to be significantly spinning to satisfy constraints on the maximum NS mass (Abbott et al. 2020b; Most et al. 2020; Tan et al. 2020; Essick & Landry 2020; Tews et al. 2020; Zhang & Li 2020). Either way, we find that GW190814 is an outlier with respect to the BBH population and the models we consider in this work. Unless stated otherwise, when presenting results on the BBH population, we exclude GW190814.

The remainder of this paper is organized as follows. In Section 2 we describe the data used in this study and detail how we select events for analysis. In Section 3, we provide a high-level overview of our models for the distributions of binary mass, spins, and redshift. In Section 4, we describe the hierarchical method used to fit population models to data. In Section 5, we present key results and discuss the astrophysical implications. Concluding remarks are provided in Section 6. The Appendix provides additional details regarding the statistical method (Appendix A) and descriptions of models (Appendix B, D, E), outlier analyses and model checking (Appendix C), and other supplementary material, including a discussion of gravitational lensing (Appendix F). The data release for this paper is available online in Abbott et al. (2020d).

2. DATA AND EVENT SELECTION

Searches for gravitational wave transients in the O3a data identified 39 candidate events with FAR below 2 yr^{-1} (Abbott et al. 2020c). This FAR cut excludes two BBH candidates and one low-significance NSBH candidate. It is unlikely the results of our BBH analyses would differ qualitatively with the inclusion of these two additional BBH events because they are typical of other, more confident GWTC-2 detections, and including them would lead to a modest 5% increase in the catalog size. The event list was collated by combining results from several pipelines searching for compact binary mergers using archival data. The search pipelines include GstLAL (Sachdev et al. 2019; Hanna et al. 2020; Messick et al. 2017) and PyCBC (Nitz et al. 2019a; Allen et al. 2012; Allen 2005; Canton et al. 2014; Usman et al. 2016; Nitz et al. 2017), which use template-based matched

filtering techniques, and cWB (Klimenko & Mitselmakher 2004; Klimenko et al. 2016), which uses a wavelet-based search that does not assume a physically parameterized signal model. These pipelines, along with two additional pipelines, MBTA (Adams et al. 2016), and SPIIR (Chu 2017), recovered most of the event candidates in low-latency.

For the population studies presented here, the event list is further restricted to the 36 events with $\text{FAR} < 1 \text{ yr}^{-1}$ as a means to increase the purity of the sample. This FAR threshold excludes the lower-significance triggers GW190426_152155 (a potential NSBH or BBH candidate), GW190719_215514 and GW190909_114149 that appear in Abbott et al. (2020c). At this FAR threshold, we expect ~ 1 noise event, and therefore a contamination fraction of $\lesssim 3\%$.⁴ In this work we assume that all of the event candidates that meet this FAR threshold are of astrophysical origin. For the population analysis of the GWTC-1 BBH events, the selection criteria used for inclusion in the study is the FAR and the probability p_{astro} that the source is of astrophysical origin. This value was only computed for BBHs with $\text{FAR} < 2 \text{ yr}^{-1}$ in Abbott et al. (2020c), so we simplify our criterion to only select on FAR. The set of GWTC-1 events that pass this FAR threshold is identical to the previous set chosen by FAR and p_{astro} . Therefore, while the selection criteria here are different from our GWTC-1 analysis, the analyzed events are consistent.

In addition to the 36 events from O3a which passed the FAR threshold, the 11 detections presented in GWTC-1 (Abbott et al. 2019b) are also included in the event list used here to infer properties of the underlying population. All 47 events used in this analysis are tabulated in Table 1. Of these systems, 44 have both masses confidently in the BH mass range, with $m_1 \geq m_2 > 3 M_\odot$. Unless stated otherwise, we restrict BBH population results to these 44 (see also Appendix C.3). Since our statistical framework relies on accurately quantifying the selection effects of our search, we only include events identified in GWTC-2, for which we have measured the search sensitivity; see Appendix A. In particular, the event list does not include candidates identified by independent analyses (Zackay et al. 2020; Venumadhav et al. 2020, 2019; Zackay et al. 2019; Nitz et al. 2019b, 2020; Magee et al. 2019) of the publicly released LIGO and Virgo data (Abbott et al. 2019c; Trovato et al. 2020). Galaudage et al. (2019) and Roulet et al. (2020) suggest that our results are unlikely to change significantly with the inclusion of these events, and in the future it may be possible to include events

⁴ In this estimate, we do not include a trial factor penalty for the fact that we look for candidates with multiple pipelines.

from independent groups using a unified framework for the calculation of significance (Ashton & Thrane 2020; Pratten & Vecchio 2020; Roulet et al. 2020).

Parameter estimation results for each candidate event (Abbott et al. 2020c) were obtained using the **LALInference** (Veitch et al. 2015; LIGO Scientific Collaboration 2018), **RIFT** (Lange et al. 2018; Wysocki et al. 2019b), and **Bilby** (Ashton et al. 2019; Romero-Shaw et al. 2020b) pipelines, the latter employing the **dynesty** nested sampling tool (Speagle 2020). The parameter estimation pipelines use Bayesian sampling methods to produce fair draws from the posterior distribution function of the source parameters, conditioned on the data and given a models for the signal and noise (Abbott et al. 2016c).

For the BBH events previously published in GWTC-1, we use the published posterior samples inferred using the **IMRPHENOMPv2** (Hannam et al. 2014; Khan et al. 2016; Husa et al. 2016; Bohé et al. 2016) and **SEOB-NRv3** (Pan et al. 2014; Taracchini et al. 2014; Babak et al. 2017) waveform models. For the new BBH events of GWTC-2, we use waveform approximants that include higher-order multipole content, including the **IMRPHENOMPv3HM** (Khan et al. 2020), **NRSUR7DQ4** (Varma et al. 2019) and **SEOBNRv4PHM** (Bohé et al. 2017; Ossokine et al. 2020). For all events, we average over these waveform families, in contrast to our previously published parameter estimation results for GW190521, which highlighted results from one waveform, **NRSUR7DQ4** (Abbott et al. 2020e). A more complete description of the parameter estimation methods and waveform models used can be found in Section V of Abbott et al. (2020c).

3. POPULATION MODELS

In this section, we provide a high-level overview of the different population models used in this paper. Each model is given a nickname indicated in boldface. There are three categories of models: models for the shape of the mass distribution (Section 3.1), models for the spin distribution (Section 3.2), and models for the redshift distribution (Section 3.3). Readers interested in the astrophysical results may wish to skip ahead to Section 5. In Fig. 1, we provide graphical representations of each mass model described below. Additional details about each model are provided in Appendix B, including their mathematical definitions, lists of hyper-parameters, and their associated prior distributions.

3.1. Black hole mass distribution

- **TRUNCATED** (4 parameters; Appendix B.1). Our simplest mass model, the distribution of primary masses is a power-law with hard cut-offs at both

low (m_{\min}) and high (m_{\max}) masses. The high-mass cut-off corresponds to the lower edge of the theorized pair-instability gap in the BH mass spectrum (Woosley & Heger 2015; Heger & Woosley 2002; Heger et al. 2003). The mass ratio distribution is also assumed to be a power law (Kovetz et al. 2017; Fishbach & Holz 2017). In Abbott et al. (2019a), it is referred to as “Model B.” This model struggles to accommodate high-mass events like GW190521, necessitating more complicated models.

- **POWER LAW + PEAK** (8 parameters; Appendix B.2). Similar to the **TRUNCATED** model, but with two modifications. At low masses we implement a smoothing function to avoid a hard cut-off. At high masses, we include a Gaussian peak, initially introduced to model a pile-up from pulsational pair-instability supernovae (Talbot & Thrane 2018). This model is better able to accommodate the high-mass events that pose a challenge for the **TRUNCATED** model. In Abbott et al. (2019a), it is referred to as “Model C.”
- **BROKEN POWER LAW** (7 parameters; Appendix B.3). The same as **TRUNCATED** except, instead of a single power-law between m_{\min} and m_{\max} , the model allows for a break in the power-law at some mass m_{break} . This model includes the low-mass smoothing function used in the **POWER LAW + PEAK** model. The high mass feature m_{break} may correspond to the onset of pair-instability, and the second power-law can be thought of as either a gradual tapering off, or a subpopulation of BHs within the pair-instability mass gap. This model accommodates the high-mass events that pose a challenge for the **TRUNCATED** while providing an alternative to the **POWER LAW + PEAK** model.
- **MULTI PEAK** (11 parameters; Appendix B.4). This phenomenological model is similar to **POWER LAW + PEAK** except we allow for two peaks. The resulting mass distribution can accommodate hierarchical BBH mergers (Miller & Hamilton 2002b; Gültekin et al. 2004; Antonini & Rasio 2016; Rodriguez et al. 2019), in which second-generation mergers create a second high-mass peak in the BH mass spectrum. We use this model to test if GWTC-2 exhibits evidence for hierarchical mergers.

3.2. Spin Distribution

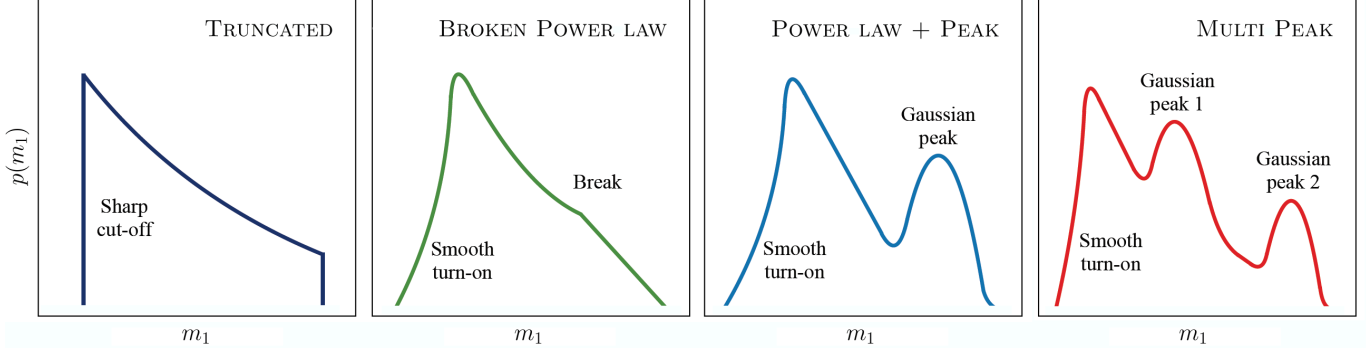


Figure 1. Graphical representations of the various mass distributions described in Section 3.1. MULTI SPIN, a model of both mass and spin, is similar to the mass distribution of POWER LAW + PEAK, with a sharp lower mass cutoff rather than the smooth low mass turn-on.

- **DEFAULT** (4 parameters; Appendix D.1). This parameterization for the component BH spin magnitudes and tilts was previously used to explore the spin distribution of compact binaries in GWTC-1 (Abbott et al. 2019a). The spin of each component BH in a binary is assumed to be independently drawn from the same underlying distribution. The dimensionless spin magnitude is described using a beta distribution as in Wysocki et al. (2019a). The spin tilt distribution from Talbot & Thrane (2017) is a mixture model comprising two components: an isotropic component designed to model dynamically assembled binaries, and a second component in which the spins are preferentially aligned with the orbital angular momentum, as expected for isolated field binaries; the fraction of binaries in the purely-aligned sub-population is denoted ζ .⁵ For this latter component, the spin tilt angles are distributed as a truncated Gaussian, with width σ_t , that peaks when the BH spin is aligned to the orbital angular momentum. We use this model in concert with the mass models described above.
- **GAUSSIAN** (5 parameters; Appendix D.2). While the DEFAULT spin model is physically inspired, this model, based on that of Miller et al. (2020), allows us to fit the distribution of phenomenological spin parameters χ_{eff} (the effective inspiral spin parameter, Eq. 5) and χ_p (the effective precession spin parameter, Eq. 6), assuming that their distribution is jointly described as a bivariate Gaussian. The ensemble properties of χ_{eff} and χ_p allow us to con-

clude that the BBHs in GWTC-2 exhibit general relativistic spin-induced precession of the orbital plane ($\chi_p > 0$), and that some systems have component spins misaligned by more than 90° ($\chi_{\text{eff}} < 0$) relative to the orbital angular momentum.

- **MULTI SPIN** (12 spin parameters, 10 mass parameters; Appendix D.3). This model allows for multiple subpopulations of BBH systems with distinct mass and spin distributions. Specifically, this model assumes a TRUNCATED power-law mass distribution with the additional presence of a 2-D Gaussian subpopulation in m_1 and m_2 , truncated such that $m_1 \geq m_2$. While similar to the POWER LAW + PEAK mass model, there is no smooth turn on and the mass ratio distribution is allowed to differ between each subpopulation. Most importantly, the two subpopulations have independently parameterized DEFAULT spin distributions. We use this model to test whether the BBH spin distribution varies as a function of mass as expected if higher-mass systems are the products of hierarchical mergers.

3.3. Redshift evolution

- **NON-EVOLVING** (0 parameters). Our default model posits that the merger rate is uniform in comoving volume.
- **POWER-LAW EVOLUTION** (1 parameter; Appendix E). Following Fishbach et al. (2018), the merger rate density is described by a power-law in $(1+z)$ where z is redshift. Given the finite range of Advanced LIGO and Advanced Virgo to BBH mergers, we only expect to constrain the redshift evolution at redshifts $z \lesssim 1$ (Abbott et al. 2013). The farthest event in our analysis is likely GW190706_222641, at redshift $z = 0.71^{+0.32}_{-0.27}$.

⁵ Throughout the paper, spin tilt is measured at a reference frequency of 20 Hz for all events except GW190521, for which the spin tilt is measured at 11 Hz (see discussion in Abbott et al. 2020c). We verified that for GW190521, the difference between the spin measurements at 20 Hz and 11 Hz are smaller than the systematic uncertainty between the waveform models.

Event	$m_1 [M_\odot]$	$m_2 [M_\odot]$	FAR [yr ⁻¹]
GW150914	35.7 ^{+4.7} _{-3.1}	30.6 ^{+3.0} _{-4.4}	$< 1.0 \times 10^{-7}$
GW151012	23.4 ^{+15.1} _{-5.6}	13.6 ^{+4.1} _{-4.9}	7.9×10^{-3}
GW151226	13.7 ^{+8.7} _{-3.2}	7.7 ^{+2.2} _{-2.6}	$< 1.0 \times 10^{-7}$
GW170104	31.2 ^{+7.3} _{-5.8}	20.0 ^{+4.9} _{-4.7}	$< 1.0 \times 10^{-7}$
GW170608	10.9 ^{+5.5} _{-1.7}	7.6 ^{+1.4} _{-2.2}	$< 1.0 \times 10^{-7}$
GW170729	51.9 ^{+16.5} _{-10.8}	33.9 ^{+10.2} _{-10.4}	2.0×10^{-2}
GW170809	35.2 ^{+8.5} _{-6.0}	23.8 ^{+5.3} _{-5.2}	$< 1.0 \times 10^{-7}$
GW170814	30.6 ^{+5.6} _{-3.0}	25.3 ^{+2.8} _{-4.1}	$< 1.0 \times 10^{-7}$
* GW170817	1.6 ^{+0.3} _{-0.2}	1.2 ^{+0.2} _{-0.2}	$< 1.0 \times 10^{-7}$
GW170818	35.4 ^{+7.5} _{-4.7}	26.7 ^{+4.3} _{-5.2}	4.2×10^{-5}
GW170823	40.0 ^{+11.5} _{-7.1}	29.1 ^{+7.2} _{-8.4}	$< 1.0 \times 10^{-7}$
GW190408_181802	24.6 ^{+5.1} _{-3.4}	18.4 ^{+3.3} _{-3.6}	$< 1.0 \times 10^{-5}$
GW190412	30.1 ^{+4.7} _{-5.1}	8.3 ^{+1.6} _{-0.9}	$< 1.0 \times 10^{-5}$
GW190413_052954	34.7 ^{+12.6} _{-8.1}	23.7 ^{+7.3} _{-6.7}	7.2×10^{-2}
GW190413_134308	47.5 ^{+13.5} _{-10.7}	31.8 ^{+11.7} _{-10.8}	4.4×10^{-2}
GW190421_213856	41.3 ^{+10.4} _{-6.9}	31.9 ^{+8.0} _{-8.8}	7.7×10^{-4}
GW190424_180648	40.5 ^{+11.1} _{-7.3}	31.8 ^{+7.6} _{-7.7}	7.8×10^{-1}
* GW190425	2.0 ^{+0.6} _{-0.3}	1.4 ^{+0.3} _{-0.3}	7.5×10^{-4}
GW190503_185404	43.3 ^{+9.2} _{-8.1}	28.4 ^{+7.7} _{-8.0}	$< 1.0 \times 10^{-5}$
GW190512_180714	23.3 ^{+5.3} _{-5.8}	12.6 ^{+3.6} _{-2.5}	$< 1.0 \times 10^{-5}$
GW190513_205428	35.7 ^{+9.5} _{-9.2}	18.0 ^{+7.7} _{-4.1}	$< 1.0 \times 10^{-5}$
GW190514_065416	39.0 ^{+14.7} _{-8.2}	28.4 ^{+9.3} _{-8.8}	5.3×10^{-1}
GW190517_055101	37.4 ^{+11.7} _{-7.6}	25.3 ^{+7.0} _{-7.3}	5.7×10^{-5}
GW190519_153544	66.0 ^{+10.7} _{-12.0}	40.5 ^{+11.0} _{-11.1}	$< 1.0 \times 10^{-5}$
GW190521	95.3 ^{+28.7} _{-18.9}	69.0 ^{+22.7} _{-23.1}	2.0×10^{-4}
GW190521_074359	42.2 ^{+5.9} _{-4.8}	32.8 ^{+5.4} _{-6.4}	$< 1.0 \times 10^{-5}$
GW190527_092055	36.5 ^{+16.4} _{-9.0}	22.6 ^{+10.5} _{-8.1}	6.2×10^{-2}
GW190602_175927	69.1 ^{+15.7} _{-13.0}	47.8 ^{+14.3} _{-17.4}	1.1×10^{-5}
GW190620_030421	57.1 ^{+16.0} _{-12.7}	35.5 ^{+12.2} _{-12.3}	2.9×10^{-3}
GW190630_185205	35.1 ^{+6.9} _{-5.6}	23.7 ^{+5.2} _{-5.1}	$< 1.0 \times 10^{-5}$
GW190701_203306	53.9 ^{+11.8} _{-8.0}	40.8 ^{+8.7} _{-12.0}	1.1×10^{-2}
GW190706_222641	67.0 ^{+14.6} _{-16.2}	38.2 ^{+14.6} _{-13.3}	$< 1.0 \times 10^{-5}$
GW190707_093326	11.6 ^{+3.3} _{-1.7}	8.4 ^{+1.4} _{-1.7}	$< 1.0 \times 10^{-5}$
GW190708_232457	17.6 ^{+4.7} _{-2.3}	13.2 ^{+2.0} _{-2.7}	2.8×10^{-5}
GW190720_000836	13.4 ^{+6.7} _{-3.0}	7.8 ^{+2.3} _{-2.2}	$< 1.0 \times 10^{-5}$
GW190727_060333	38.0 ^{+9.5} _{-6.2}	29.4 ^{+7.1} _{-8.4}	$< 1.0 \times 10^{-5}$
GW190728_064510	12.3 ^{+7.2} _{-2.2}	8.1 ^{+1.7} _{-2.6}	$< 1.0 \times 10^{-5}$
GW190731_140936	41.5 ^{+12.2} _{-9.0}	28.8 ^{+9.7} _{-9.5}	2.1×10^{-1}
GW190803_022701	37.3 ^{+10.6} _{-7.0}	27.3 ^{+7.8} _{-8.2}	2.7×10^{-2}
† GW190814	23.2 ^{+1.1} _{-1.0}	2.59 ^{+0.08} _{-0.09}	$< 1.0 \times 10^{-5}$
GW190828_063405	32.1 ^{+5.8} _{-4.0}	26.2 ^{+4.6} _{-4.8}	$< 1.0 \times 10^{-5}$
GW190828_065509	24.1 ^{+7.0} _{-7.2}	10.2 ^{+3.6} _{-2.1}	$< 1.0 \times 10^{-5}$
GW190910_112807	43.9 ^{+7.6} _{-6.1}	35.6 ^{+6.3} _{-7.2}	1.9×10^{-5}
GW190915_235702	35.3 ^{+9.5} _{-6.4}	24.4 ^{+5.6} _{-6.1}	$< 1.0 \times 10^{-5}$
GW190924_021846	8.9 ^{+7.0} _{-2.0}	5.0 ^{+1.4} _{-1.9}	$< 1.0 \times 10^{-5}$
GW190929_012149	80.8 ^{+33.0} _{-33.2}	24.1 ^{+19.3} _{-10.6}	2.0×10^{-2}
GW190930_133541	12.3 ^{+12.4} _{-2.3}	7.8 ^{+1.7} _{-3.3}	3.3×10^{-2}

Table 1. A summary of the events included in this analysis. Asterisks (*) denote binaries in which both components lie in the NS mass range while a dagger (†) indicates a system in which the nature of the secondary component is unknown. Both of these classes are excluded from our analyses unless explicitly stated. From left to right, the columns show the event name, the 90% credible interval for primary source mass (units of M_\odot), the 90% credible interval for secondary mass (units of M_\odot), and the minimum available FAR. For events detected in more than one CBC detection pipeline, we report the lowest of the available FAR estimate. These credible intervals are obtained using a prior that is uniform in redshifted component mass and comoving volume, as in Table 6 of [Abbott et al. \(2020c\)](#).

4. METHOD

We adopt a hierarchical Bayesian approach, marginalizing over the properties of individual events to measure parameters of the population models described above; see, e.g., (Thrane & Talbot 2019; Mandel et al. 2019; Vitale 2020). Given data $\{d_i\}$ from N_{det} gravitational-wave detections, the likelihood of the data given population parameters Λ is (Loredo 2004; Mandel et al. 2019; Thrane & Talbot 2019)

$$\mathcal{L}(\{d\}|\Lambda, N) \propto N^{N_{\text{det}}} e^{-N\xi(\Lambda)} \prod_{i=1}^{N_{\text{det}}} \int \mathcal{L}(d_i|\theta) \pi(\theta|\Lambda) d\theta. \quad (1)$$

Here, N is the total number of events expected during the observation period (including both resolvable and unresolvable signals). Each event is described by a set of parameters θ , the likelihood of which is $\mathcal{L}(d|\theta)$. The conditional prior $\pi(\theta|\Lambda)$, meanwhile, is defined by the mass, spin, and redshift models described above in Sec. 3. It serves to quantify the predicted distribution of event parameters θ given the hyper-parameters Λ of the population model. An example of a hyper-parameter is the power-law index α governing primary mass distribution $\pi(m_1|\alpha) \propto m_1^{-\alpha}$ for the TRUNCATED mass model. Finally, $\xi(\Lambda)$ is the fraction of binaries that we expect to successfully detect for a population described by hyper-parameters Λ . The procedure for calculating $\xi(\Lambda)$ is described in Appendix A. One of our primary goals in this paper is to constrain the population hyper-parameters describing the distribution of gravitational-wave signals. Given a log-uniform prior on N , one can marginalize Eq. (1) over N to obtain (Fishbach et al. 2018; Mandel et al. 2019; Vitale 2020)

$$\mathcal{L}(\{d\}|\Lambda) \propto \prod_{i=1}^{N_{\text{det}}} \frac{\int \mathcal{L}(d_i|\theta) \pi(\theta|\Lambda) d\theta}{\xi(\Lambda)}. \quad (2)$$

To evaluate the single-event likelihood $\mathcal{L}(d_i|\theta)$, we use posterior samples that are obtained using some default prior $\pi_{\emptyset}(\theta)$. In this case, integrals over the likelihood can be replaced with weighted averages “ $\langle \dots \rangle$ ” over discrete samples. Equation (2), for example, becomes

$$\mathcal{L}(\{d\}|\Lambda) \propto \prod_{i=1}^{N_{\text{det}}} \frac{1}{\xi(\Lambda)} \left\langle \frac{\pi(\theta|\Lambda)}{\pi_{\emptyset}(\theta)} \right\rangle_{\text{samples}}, \quad (3)$$

where the factor of $\pi_{\emptyset}(\theta)$ serves to divide out the prior used for initial parameter estimation. We evaluate the likelihoods for population models using the `emcee`, `dynesty`, and `stan` packages (Foreman-Mackey et al. 2013; Speagle 2020; Carpenter et al. 2017; Riddell et al. 2018). The likelihoods are implemented in a variety of

software including `GWPopulation` (Talbot et al. 2019) and `PopModels` (Wysocki & O’Shaughnessy 2017). The priors adopted for each of our hyper-parameters are described in Appendix B.

Throughout this paper, we find it useful to distinguish between the *astrophysical* distribution of a parameter—the distribution as it is in nature—and the *observed* distribution of a parameter—the distribution as it appears among detected events due to selection effects. The *posterior population distribution* for a given model represents our best guess for the *astrophysical* distribution of some source parameter θ , averaged over the posterior for population parameters Λ :

$$p_{\Lambda}(\theta) = \int d\Lambda \pi(\theta|\Lambda) p(\Lambda|\{d\}). \quad (4)$$

The subscript Λ indicates that we have marginalised over population parameters. Meanwhile, the *posterior predictive distribution* refers to the population-averaged distribution of source parameters θ *conditioned on detection*.

In Appendix C, D and E, we provide posterior predictive checks for our population models. These checks consist of comparing simulated sets of N_{obs} “predicted” and “observed” events. For every sample in the model hyper-posterior, we generate a set of predicted events by reweighting our found injections to the population model, and drawing N_{obs} synthetic events. For each hyper-posterior sample, we then generate a set of observed events by reweighting the single-event posteriors of the N_{obs} events to this population prior, and drawing one sample per event. Therefore, the inferred distribution of observed events depends on the population model considered. The first example of such a posterior predictive check is shown in Fig. 19. We calculate the cumulative distribution function for each set of predicted and observed events in the model hyper-posterior, and summarize these curves with 90% credibility bands. The uncertainty in the predicted bands comes from uncertainty in the population hyper-posterior, as well as Poisson fluctuations, because each cumulative distribution curve consists of N_{obs} simulated events.

Phenomenological models such as we employ here can fail if their assumed form does not adequately represent reality or if priors are inappropriately chosen. Inferences from such models are inevitably prone to systematic error, given that the model is unlikely to be a perfect description of reality; for instance, the inferred local rate of BBH mergers is subject to a systematic error associated with our choice of model(s) for the BBH mass distribution. While such errors cannot be eliminated, we take steps to control and minimize their magnitude. First, we carry out posterior predictive checks to make sure

our models are consistent with the data. Next, where possible, we check for consistency between models with different assumptions, for example, looking for common features in the POWER LAW + PEAK and BROKEN POWER LAW models. Finally, we carry out tests to make sure that our inferences are not artifacts of our model design, for example, by applying the models to simulated uninformative data. Additional information about these tests is provided in the Appendix.

5. RESULTS AND DISCUSSION

5.1. Mass Distribution

In this subsection we report results obtained using the mass models described in Section 3.1 (see Fig. 1).⁶ We employ the DEFAULT spin model and the NON-EVOLVING redshift model. The results shown here are marginalized over the hyperparameters of the spin distribution.

A truncated power law fails to fit the high-mass BBH events. The TRUNCATED model applied in Abbott et al. (2019a) measured the sharp high-mass cutoff to be $m_{\max} = 40.8^{+11.8}_{-4.4} M_{\odot}$. When we fit this model to GWTC-2 data, we obtain $m_{\max} = 78.5^{+14.1}_{-9.4} M_{\odot}$, in significant tension ($> 99\%$ credibility) with the GWTC-1 result; see Fig. 2. The TRUNCATED model struggles to accommodate the high-mass systems of GWTC-2. At 99% credibility, three events of GWTC-2 have $m_1 > 45 M_{\odot}$ (regardless of whether we use a population-informed prior; Fishbach et al. 2020b). This tension remains (at the $> 93\%$ credibility level) even when we exclude the highest-mass event GW190521 (Abbott et al. 2020e,f). The poor fit of the TRUNCATED model is further seen in the posterior predictive check of Fig. 19 in Appendix C, which shows that the TRUNCATED model fails to capture the relative excess of observations with $m_1 \sim 30 M_{\odot}$ compared to the number of events with $m_1 \gtrsim 45 M_{\odot}$. Our fit to the TRUNCATED model overpredicts the number of observations with $m_1 > 45 M_{\odot}$ relative to the number of observations with $30 M_{\odot} < m_1 < 45 M_{\odot}$ (98% credibility).

The POWER LAW + PEAK, BROKEN POWER LAW, and MULTI PEAK models provide better fits to the shape of the mass distribution, particularly at high masses. Although our updated fit to the mass distribution extends to higher masses than the GWTC-1 fit, we find that $97.1^{+1.7}_{-3.5}\%$ of BBH systems have primary masses

⁶ In this study, we employ models in which the mass and redshift distributions factorize. This is a reasonable assumption for the $z \lesssim 1$ binaries in GWTC-2 and preliminary tests suggest our data are well-fit with this assumption. However, as more binaries are detected from ever greater distances, it will be interesting to test models that allow for the mass distribution to evolve with redshift.

Mass model	\mathcal{B}	$\log_{10} \mathcal{B}$
POWER LAW + PEAK	1.0	0.0
MULTI PEAK	0.5	-0.3
BROKEN POWER LAW	0.12	-0.92
TRUNCATED	0.01	-1.91
POWER LAW + PEAK ($\delta_m = 0$)	0.87	-0.06
BROKEN POWER LAW + PEAK	0.74	-0.13
BROKEN POWER LAW ($\delta_m = 0$)	0.35	-0.46
POWER LAW + PEAK ($\lambda_{\text{peak}} = 0$)	0.05	-1.34

Table 2. Bayes factors for each mass model relative to the favored POWER LAW + PEAK model, which gives the highest Bayesian evidence for GWTC-2. For models that have a smooth turn on at low masses parameterized by δ_m , we also compare the corresponding sub-model with a sharp minimum mass cutoff ($\delta_m = 0$). For the POWER LAW + PEAK model which includes a fraction λ_{peak} of systems in the Gaussian component, we compare the sub-model with $\lambda_{\text{peak}} = 0$. GW190814 is excluded from this analysis.

below $45 M_{\odot}$ (POWER LAW + PEAK model), consistent with the GWTC-1 estimate that 99% of primary masses lie below $\sim 45 M_{\odot}$ (Abbott et al. 2019a; Kimball et al. 2020a). In Table 2, we provide log Bayes factors ($\log_{10} \mathcal{B}$) comparing the mass models; each Bayes factor is measured relative to the model with the highest Bayesian evidence: POWER LAW + PEAK. In each case we use the DEFAULT spin model. For context, $\log_{10} \mathcal{B} > 1.5$ is often interpreted as a strong preference for one model over another, and $\log_{10} \mathcal{B} > 2$ as decisive evidence (Jeffreys 1961).

While Bayes factors depend on the choice of hyperparameter priors, it is nonetheless possible to see that the TRUNCATED model is disfavored compared to the more complicated models. This inference is driven in part by the fact that—in our posterior predictive checks—94% of the time, the TRUNCATED model overpredicts the number of detections with $m_1 > 50 M_{\odot}$. See Appendix C for information about the posterior predictive checks. Meanwhile, there is not a strong preference for POWER LAW + PEAK over BROKEN POWER LAW or MULTI PEAK. We currently lack the resolving power to determine whether the deviations from TRUNCATED are best modeled as a break, a Gaussian peak, or two Gaussian peaks. As a further check, we carried out a follow-up analysis using a hybrid BROKEN POWER LAW + PEAK model, which indicated only modest support for a peak on top of the BROKEN POWER LAW distribution ($\log_{10} \mathcal{B} = 0.79$).

There are features in the black hole mass spectrum beyond a power-law. Figure 3 shows the astrophysical merger rate density as a function of primary BH mass for the TRUNCATED, POWER LAW + PEAK,

Events	Mass model	$m_{1\%} (M_{\odot})$	$m_{99\%} (M_{\odot})$
All confident BBH events - <i>excluding</i> GW190814	TRUNCATED	$6.0^{+0.8}_{-2.1}$	$65.5^{+10.4}_{-9.6}$
	BROKEN POWER LAW	$5.6^{+1.3}_{-1.6}$	$57.8^{+12.5}_{-8.7}$
	POWER LAW + PEAK	$6.0^{+1.0}_{-1.6}$	$59.7^{+13.9}_{-12.8}$
	MULTI PEAK	$6.0^{+1.0}_{-1.6}$	$66.0^{+12.1}_{-16.4}$
All confident BBH events - <i>including</i> GW190814	TRUNCATED	$2.4^{+0.2}_{-0.3}$	$60.3^{+10.1}_{-13.2}$
	BROKEN POWER LAW	$2.6^{+0.5}_{-0.3}$	$56.1^{+12.5}_{-9.0}$
	POWER LAW + PEAK	$2.5^{+0.3}_{-0.3}$	$57.8^{+15.3}_{-14.5}$
	MULTI PEAK	$2.6^{+0.4}_{-0.3}$	$63.8^{+11.2}_{-19.1}$
All confident BBH events - <i>excluding</i> GW190521, GW190814	TRUNCATED	$5.8^{+0.9}_{-2.8}$	$52.3^{+8.9}_{-5.2}$
	BROKEN POWER LAW	$5.6^{+1.3}_{-1.8}$	$52.3^{+9.5}_{-5.9}$
	POWER LAW + PEAK	$5.9^{+1.0}_{-1.5}$	$52.4^{+13.2}_{-7.0}$
	MULTI PEAK	$6.2^{+0.8}_{-1.5}$	$58.9^{+11.0}_{-11.7}$

Table 3. The $m_{1\%}$ and $m_{99\%}$ credible intervals (90%) for various mass models and combinations of events. These variables are defined such that, among the *astrophysical* BBH population, 1% of systems have primary masses $m_1 \leq m_{1\%}$, while 99% have primary masses $m_1 \leq m_{99\%}$. The POWER LAW + PEAK, MULTI PEAK, and BROKEN POWER LAW models are preferred over the TRUNCATED model.

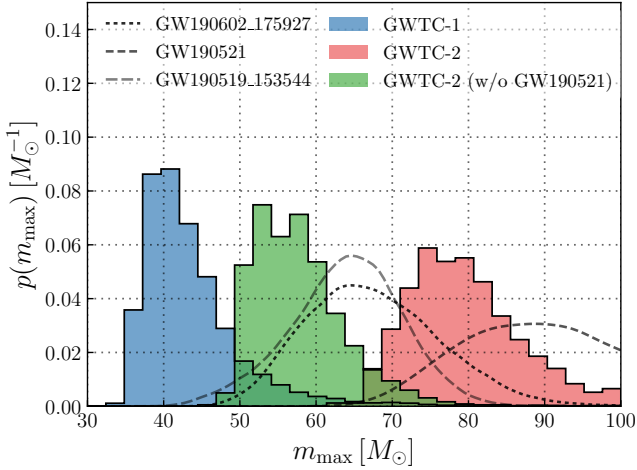


Figure 2. Posterior for the maximum mass using GWTC-1 and fit to the TRUNCATED model (blue), compared to the posterior obtained by adding events from O3a data (red). The two distributions are inconsistent, suggesting the TRUNCATED model is inadequate. The tension between GWTC-1 and GWTC-2 is somewhat alleviated by the exclusion of the high-mass event GW190521 (green). However, there remain several other high-mass events in O3a. The black dashed lines show primary mass posteriors for the three events in which $m_1 > 45 M_{\odot}$ at 99% credibility (we employ a prior that is uniform in redshifted masses). These events cause a significant shift in the m_{\max} posterior if we assume a simple power-law fits the data.

MULTI PEAK and BROKEN POWER LAW models. Figure 4, meanwhile, shows the posterior predictive distribution for primary masses, including selection effects. Corner plots showing the constraints for the parameters in each model are available in Appendix B; see Figs. 16, 17 and 18. In Appendix C, we show posterior predictive

checks for each model (Fig. 19 and Fig. 23), comparing mock observations predicted by the model to the empirical distribution inferred from GWTC-2.

We turn first to the BROKEN POWER LAW model (second panel in Fig. 3), which is characterized by two spectral indices, α_1 and α_2 , with $p(m_1) \propto m_1^{-\alpha_1}$ for $m_1 < m_{\text{break}}$, and $p(m_1) \propto m_1^{-\alpha_2}$ above the break. We find the data prefer a break at $m_{\text{break}} = 39.7^{+20.3}_{-9.1} M_{\odot}$; 90% credible bounds on the location of this break are denoted by the gray vertical band in the second panel of Fig. 3. For masses above the break, the BROKEN POWER LAW model prefers a significantly steeper power-law slope, from $\alpha_1 = 1.58^{+0.82}_{-0.86}$ before to $\alpha_2 = 5.6^{+4.1}_{-2.5}$ after. Figure 5 shows the joint posterior on α_1 and α_2 . We infer that $\alpha_2 > \alpha_1$ at credibility 98%. The break aligns with the cutoff m_{\max} inferred with GWTC-1 data (Abbott et al. 2019a), and we speculate that the steep drop-off in the merger rate that occurs after m_{break} may be an imprint of PPSN, which are expected to become important for BH masses around $35 M_{\odot}$ (Woosley & Heger 2015; Heger & Woosley 2002; Heger et al. 2003).

The POWER LAW + PEAK model (third panel of Fig. 3) produces a qualitatively similar fit to the one obtained from the BROKEN POWER LAW model. However, a key feature of the POWER LAW + PEAK model is the Gaussian peak at $33.1^{+4.0}_{-5.6} M_{\odot}$, denoted by the gray vertical band in the third panel of Fig. 3. Evidence for a peak can be seen in Fig. 6, which shows the posterior for λ_{peak} , the fraction of systems that belong to the Gaussian component. We see that $\lambda_{\text{peak}} = 0$ (pure power law) is disfavored. It was envisioned (Talbot & Thrane 2018) that the power-law component of the POWER LAW + PEAK model would terminate in the vicinity of this peak to create a high-mass gap. However, in order to

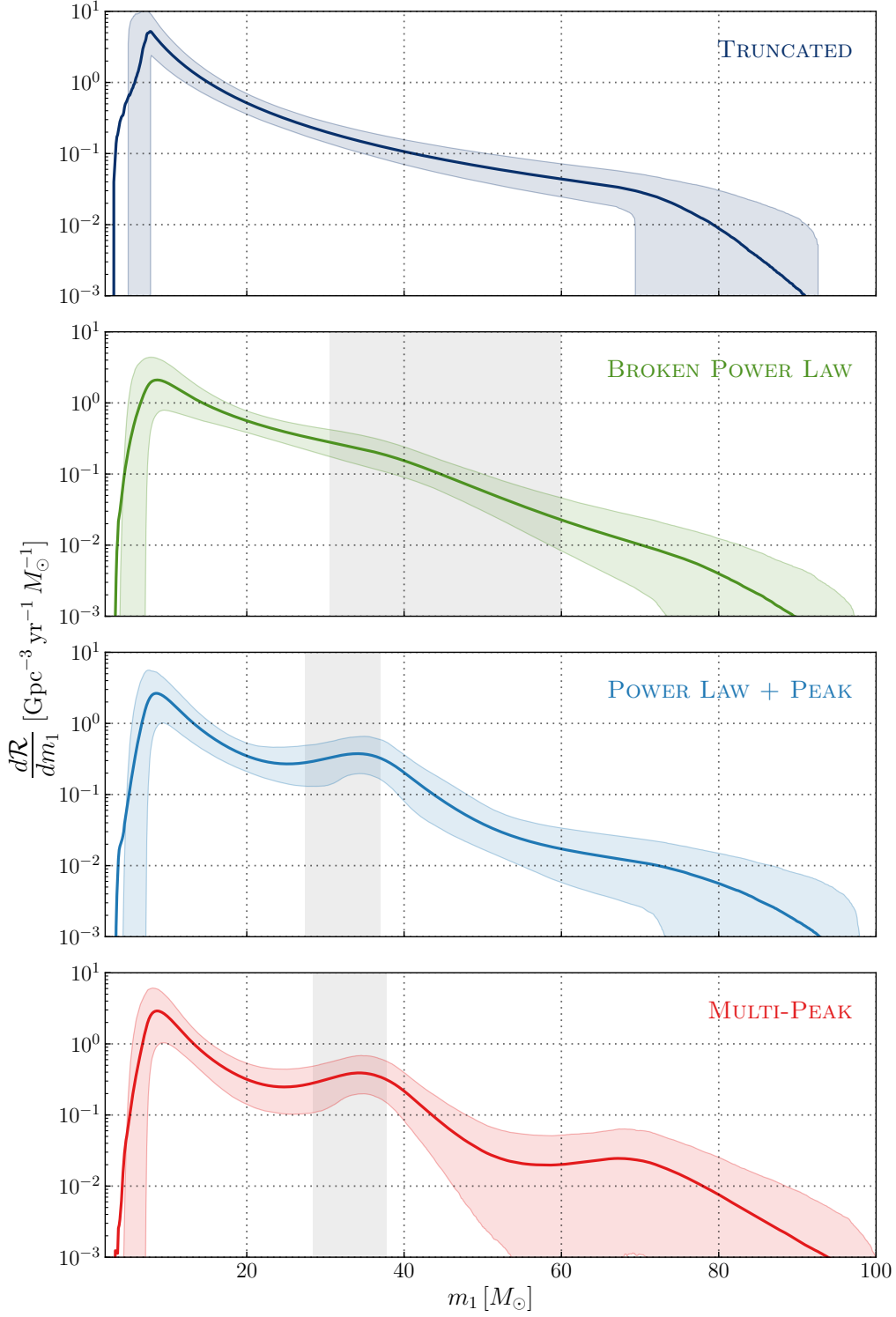


Figure 3. *Astrophysical* primary BH mass distribution for the TRUNCATED, BROKEN POWER LAW, POWER LAW + PEAK and MULTI PEAK models. The solid curve is the posterior population distribution (averaging over model uncertainty) while the shaded region shows the 90% credible interval. While the median rate is always inside the credible region, the solid curve represents the *mean*, which can be outside the credible region. Top (navy) is the TRUNCATED model, second from the top (green) is the BROKEN POWER LAW model, third from the top (blue) is for the POWER LAW + PEAK model, and bottom (red) is for the MULTI PEAK model. The TRUNCATED model is disfavored compared to the three latter models that predict a feature at $\sim 40 M_{\odot}$: a break in the mass spectrum in the BROKEN POWER LAW model or additional Gaussian peaks in the POWER LAW + PEAK and MULTI PEAK models. The vertical gray bands show 90% credible bounds on the locations of these additional features.

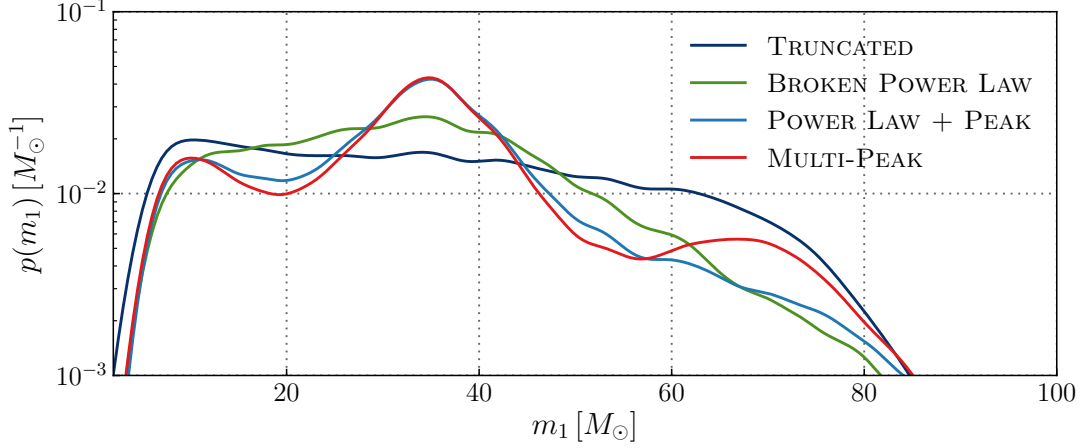


Figure 4. Observed primary BH mass distributions predicted by each mass model. For each model, we average over the uncertainty in the hyper-parameter posterior. The *observed* distribution describes the events successfully detected by LIGO–Virgo, preferentially favoring more massive systems relative to the astrophysical distribution due to selection effects.

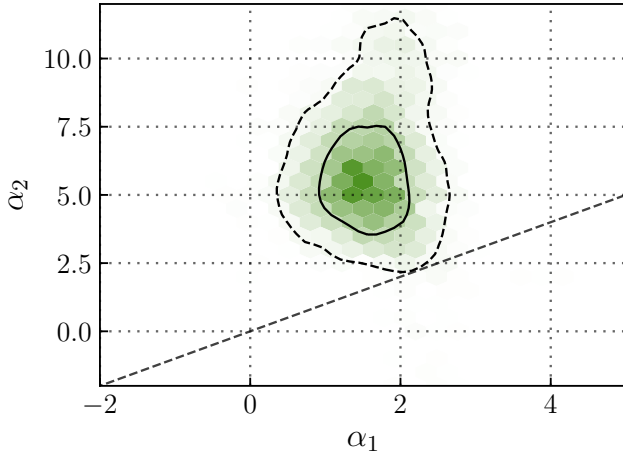


Figure 5. Constraints on the power-law indices governing the primary mass distribution within the BROKEN POWER LAW model. The parameter α_1 is the power-law index below the break, which is found to be $m_{\text{break}} = 39.7_{-9.1}^{+20.3}$ while α_2 is the index above the break. The dashed and solid contours mark the central 50% and 90% posterior credible regions, respectively, under a flat prior on α_1, α_2 in the range $(-4, 12)$. We rule out with high confidence the hypothesis that $\alpha_1 = \alpha_2$, indicated by the dashed diagonal line, finding $\alpha_2 > \alpha_1$ with 98% credibility.

accommodate the most massive binaries in GWTC-2, the power-law extends to values of $m_{\text{max}} = 86_{-13}^{+12} M_{\odot}$.

While the mass spectrum must extend to these high masses, we find that 99% of primary BH masses lie below $m_{99\%} \sim 60 M_{\odot}$; see Table 3. The *astrophysical* rate density at $\sim 80 M_{\odot}$ (the primary mass of GW190521) is two orders of magnitude lower than the rate density at $\sim 40 M_{\odot}$. However, because of selection effects, the posterior predictive distribution skews to much higher

masses, as seen in Fig. 4, so that the probability of detecting at least one event with $m_1 \geq 80 M_{\odot}$ after observing 44 BBH events drawn from the POWER LAW + PEAK posterior predictive distribution of Fig. 4 is high: 32%.

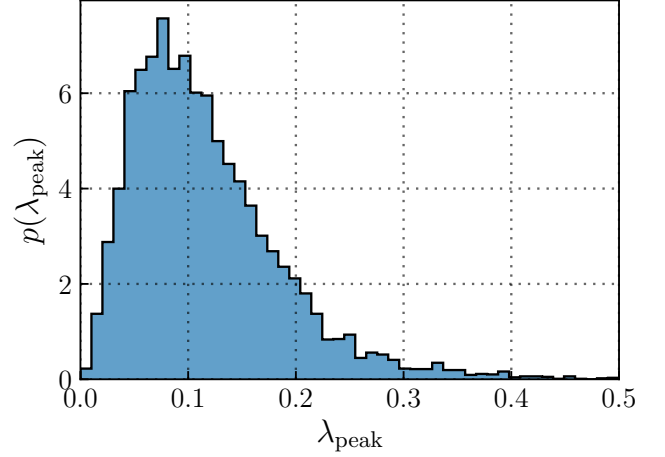


Figure 6. Posterior distribution on the fraction of binaries (λ_{peak}) in the Gaussian component of POWER LAW + PEAK model, under a flat prior on λ_{peak} ; see Appendix B.2. We find that $\lambda_{\text{peak}} = 0$ (which corresponds to no Gaussian peak) is disfavored, supporting the hypothesis that there is a feature in the BH primary mass spectrum.

We cannot determine whether the high-mass events of GWTC-2 belong to a distinct subpopulation rather than a high-mass tail of the normal BBH population. An additional subpopulation may be expected if high-mass BHs have a different origin from low mass ones; for example, if they are the products of hierarchical mergers (Fishbach et al. 2017; Gerosa & Berti 2017;

Chatziioannou et al. 2019; Doctor et al. 2019; Kimball et al. 2020a). Using the MULTI PEAK model (bottom panel in Fig. 3), which allows for a second high-mass Gaussian component at $m_1 > 50 M_\odot$ in addition to the Gaussian component at $m_1 \lesssim 40 M_\odot$, we find that the addition of a second Gaussian peak is not preferred by the data. The MULTI PEAK model is mildly disfavored compared to POWER LAW + PEAK, with a $\log_{10} \mathcal{B} = -0.3$ (or Bayes factor $\mathcal{B} = 0.5$) for MULTI PEAK relative to POWER LAW + PEAK. Motivated by the hypothesis of hierarchical mergers, we consider a variation of the MULTI PEAK model, in which the location of the second peak is required to be at twice the value of the first peak; that is, $\mu_{m,2} = 2\mu_{m,1}$ (see Appendix B.4). Studying the $(\mu_{m,1}, \mu_{m,2})$ panel of the corner plot in Fig. 18, we see that the data mildly prefer the second peak at $\approx 70 M_\odot$, consistent with twice the value of the first peak at $\approx 35 M_\odot$. This “MODIFIED MULTIPLEAK” is mildly preferred over the original version by a Bayes factor of ~ 2 . A similar conclusion is found using the MULTI SPIN model; as discussed in Section 5.2, we find hints, but no significant evidence for subpopulations with distinct spin distributions. Additional evidence for hierarchical mergers is presented in Kimball et al. (2020b).

Within the framework of the BROKEN POWER LAW, POWER LAW + PEAK and MULTI PEAK models, the most massive event, GW190521, appears to be a normal member of the BBH population in the context of the other GWTC-2 events (see Appendix C.2). The event GW190521 is an outlier if we consider it in the context of GWTC-1 with the TRUNCATED model, but we interpret this as a limitation of the TRUNCATED model (see Fig. 2; Abbott et al. 2020f).

The GWTC-1 detections showed that BHs more massive than $\sim 45 M_\odot$ merge relatively rarely, based on simple extrapolations from below $45 M_\odot$. With GWTC-2, we are beginning to resolve the shape of the primary BH mass spectrum above $45 M_\odot$. The implications are not yet clear, but there are intriguing possibilities. One hypothesis is that the events with $m_1 > 45 M_\odot$ are simply the high-mass tail of the ordinary BBH population, and do not form through a distinct channel. For example, if the lower edge of the PPSN gap may be modeled as a smooth tapering rather than a sharp cutoff, the feature at $m_{\text{break}} = 39.7^{+20.3}_{-9.1}$ may represent the onset of pair-instability. This explanation may pose challenges to our understanding of stellar evolution since the pair-instability cutoff of BH masses at $\sim 40 M_\odot$ is thought to be relatively abrupt (Woosley et al. 2002; Woosley 2017; Farmer et al. 2019), even though its precise location is uncertain (Mapelli et al. 2020; Spera & Mapelli 2017; Giacobbo et al. 2017; van Son et al. 2020; Farmer et al.

2020; Croon et al. 2020; Marchant & Moriya 2020). If the PPSN cutoff is indeed sharp and all observed BBH systems lie below the PPSN gap, the cutoff must occur at relatively high masses; in the TRUNCATED model, $m_{\text{max}} = 78.5^{+14.1}_{-9.4} M_\odot$ (or, excluding the most massive event, GW190521, $m_{\text{max}} = 57.0^{+11.9}_{-6.6} M_\odot$). This may have significant implications for nuclear (Farmer et al. 2020) and particle (Croon et al. 2020; Ziegler & Freese 2020) physics.

Another hypothesis is that the events with $m_1 > 45 M_\odot$ constitute a distinct population, created, for example, from hierarchical mergers of lower mass binaries in globular clusters or galactic nuclei (Miller & Hamilton 2002a; Antonini & Rasio 2016; Kimpson et al. 2016; Rodriguez et al. 2018; Yang et al. 2019; Arca Sedda 2020a). Alternatively, the high-mass gap might be populated from low-metallicity stellar mergers in young star clusters, the remnants of which can merge dynamically (Carlo et al. 2019a,b), BH growth through accretion (Roupas & Kazanas 2019; Rice & Zhang 2020; Natarajan 2020; Safarzadeh & Haiman 2020), or Population III stellar remnants with large hydrogen envelopes (Tanikawa et al. 2020; Farrell et al. 2020; Liu & Bromm 2020).

The BBH primary mass distribution exhibits a global maximum between ~ 4 and $\sim 10 M_\odot$. Figure 7 shows the joint posterior for the m_{min} and δ_m parameters inferred using the POWER LAW + PEAK and BROKEN POWER LAW mass models, including only BBH events with $m_2 > 3 M_\odot$. Recall that, while the TRUNCATED model has a sharp cutoff at m_{min} , the remaining models implement a smooth turn-on of width δ_m above m_{min} , causing the mass spectrum to peak and turn over between m_{min} , and $\delta_m + m_{\text{min}}$ (Talbot & Thrane 2018). Using both the BROKEN POWER LAW model and the POWER LAW + PEAK model, we find that the primary mass spectrum does not decrease monotonically from $3 M_\odot$. Rather, it turns over at $7.8^{+1.8}_{-2.0} M_\odot$ (POWER LAW + PEAK model) or $6.02^{+0.78}_{-1.96} M_\odot$ (BROKEN POWER LAW model). In other words, the mass distribution must turn over at $m_1 > 3 M_\odot$, with 99.9% credibility (assuming the POWER LAW + PEAK model) or 98.5% credibility (BROKEN POWER LAW model). As seen in Fig. 7, if the BH low-mass cutoff is sharp ($\delta_m = 0$), then $m_{\text{min}} \gtrsim 4 M_\odot$. Conversely, if the BH mass spectrum extends below $m_{\text{min}} \lesssim 4 M_\odot$, an extended turn-on $\delta_m \gtrsim 3 M_\odot$ is required. These results support the existence of a low-mass gap (or dip) between $\sim 2.6 M_\odot$ (the secondary mass of GW190814; the most massive component mass observed below $3 M_\odot$) and $\sim 6 M_\odot$, strengthening results from Fishbach et al. (2020a), although we cannot determine whether the low-mass gap is empty.

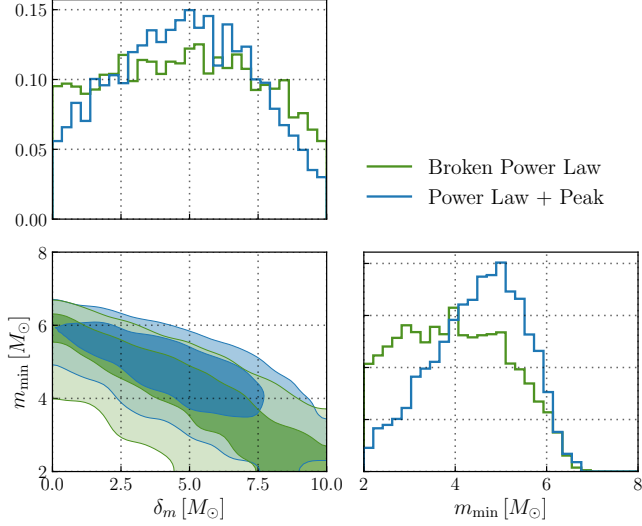


Figure 7. Posterior distribution for population parameters m_{\min} , the minimum BH mass, and δ_m , which controls the sharpness of the low-mass cut-off. A sharp cut-off corresponds to $\delta_m = 0$. Analyzing the 44 BBH events (with the exclusion of GW190814), both models exclude ($m_{\min} = 3 M_{\odot}$, $\delta_m = 0$) with $> 99\%$ credibility, indicating that the rate drops off at low masses. To varying degrees, both models allow for $m_{\min} \leq 3 M_{\odot}$, $\delta_m > 0$, suggesting that the low-mass gap may not be empty. See Appendices B.3 and B.2 for additional details about the δ_m , m_{\min} parameters.

Since our models do not permit additional features beyond a smooth turn on to a power law at low masses, they struggle to accommodate GW190814 (with secondary mass at $m_2 = 2.59^{+0.08}_{-0.09} M_{\odot}$). We can see this by comparing the mass distribution inferred from the events with $m_1 \geq m_2 > 3 M_{\odot}$, discussed above, to the distribution inferred with GW190814. If GW190814 is a BBH system, the minimum BH mass must extend to $m_{\min} = 2.18^{+0.27}_{-0.16} M_{\odot}$ (see the dashed histograms in Fig. 8a). In Fig. 8b we show how the inclusion/exclusion of GW190814 affects the shape of the primary mass distribution below $\lesssim 5 M_{\odot}$. We see that the two distributions are inconsistent at the low mass end, suggesting that there is a feature in the mass distribution between $\sim 2.6 M_{\odot}$ and $\sim 6 M_{\odot}$ that our models cannot capture. This effect can also be seen in the $m_{1\%}$ values inferred with/without GW190814, shown in Table 3. Assuming the TRUNCATED and POWER LAW + PEAK models, the m_{\min} posteriors inferred with GW190814 lie at the $0.25^{+0.44}_{-0.20}$ and $0.78^{+2.22}_{-0.69}$ percentiles, respectively, of the m_{\min} posteriors obtained without GW190814. Even using the BROKEN POWER LAW model, which admits greater overlap in the 1-dimensional m_{\min} posteriors inferred with/without GW190814, the addition of GW190814 significantly shifts the two-dimensional (δ_m, m_{\min}) pos-

terior and the inferred mass spectrum. Assuming the BROKEN POWER LAW model with GW190814, the mass at which the mass spectrum turns over is shifted down to $2.59^{+0.78}_{-0.39} M_{\odot}$, which is inconsistent with the turnover mass (the low-mass local maximum) inferred without GW190814, $6.02^{+0.78}_{-1.96} M_{\odot}$. This indicates a failure of our models to fit GW190814 together with the BBH systems of GWTC-2. This finding is supported by additional studies described in Appendix C.3. Because GW190814 is a population outlier with respect to the BBH events of GWTC-2 and our choice of models, we exclude it from the analyses here unless otherwise indicated.

The distribution of mass ratios is broad. The GWTC-1 events are all individually consistent with $q = 1$. Describing the conditional mass-ratio distribution as a power law $p(q|m_1) \propto q^{\beta_q}$, a population analysis of GWTC-1 allowed $\beta_q = 12$ (our maximum prior bound), consistent with a mass-ratio distribution sharply peaked at equal-mass pairings (Abbott et al. 2019a; Roulet & Zaldarriaga 2019; Fishbach & Holz 2020b). GWTC-2 saw the first detections of confidently asymmetric systems: GW190412 (Abbott et al. 2020a) and GW190814 (Abbott et al. 2020b). Excluding GW190814, our reconstruction of the mass ratio distribution is consistent with the results published in Abbott et al. (2020a): $\beta_q = 1.3^{+2.4}_{-1.5}$ for the POWER LAW + PEAK model and $\beta_q = 1.4^{+2.5}_{-1.5}$ for the BROKEN POWER LAW model. We rule out distributions that are sharply peaked around $q = 1$, with $\beta_q < 2.9$ (POWER LAW + PEAK) and $\beta_q < 3.1$ (BROKEN POWER LAW) at 90% credibility. However, we also disfavor distributions that prefer unequal-mass pairings, with $\beta_q > 0$ at 92% (POWER LAW + PEAK) and 94% (BROKEN POWER LAW) credibility. We find that 90% of systems in the underlying population have mass ratios $q > 0.26^{+0.14}_{-0.08}$.

5.2. Spin Distribution

In this subsection, we highlight the results from the GAUSSIAN, DEFAULT, and MULTI SPIN models. We fix the redshift distribution to a NON-EVOLVING merger rate. The GAUSSIAN and MULTI SPIN models assume the mass distributions described in Appendix D.2 and D.3, respectively. For the DEFAULT spin model, we employ the POWER LAW + PEAK mass model, simultaneously fitting the mass and spin distribution as in the previous subsection.

We observe spin-induced general relativistic precession of the orbital plane. As two BHs merge, the morphology of the resulting gravitational waveform depends on their spins. The spin-dependence of a gravitational waveform is determined in part by two phenomenological parameters. First, the effective inspiral spin pa-

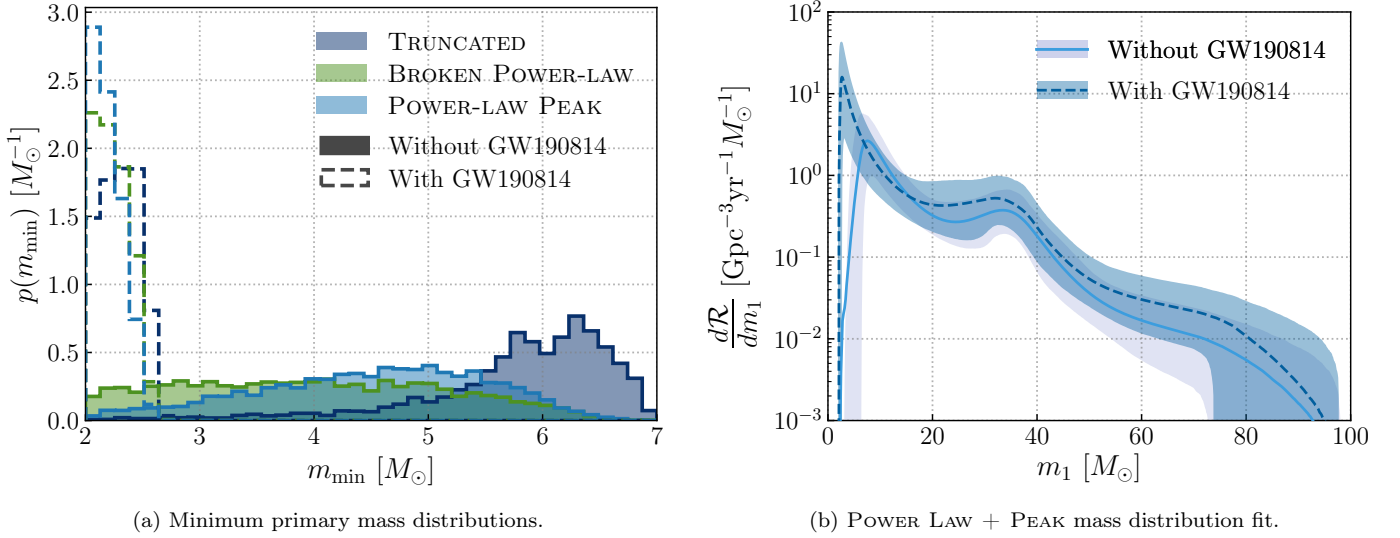


Figure 8. (a) Posterior distribution for the minimum mass parameter in the TRUNCATED (navy), BROKEN POWER LAW (green) and POWER LAW + PEAK (blue) models. The solid bars show the posterior for m_{\min} when fitting the models to the confident BBH events excluding GW190814, while the dashed lines show the fits to the BBH events including GW190814. The TRUNCATED model is disfavored. (b) Distribution of primary masses inferred using the POWER LAW + PEAK model when including (navy, dashed line) and excluding (light blue, solid line) GW190814. Only the secondary mass of GW190814 is below $3 M_{\odot}$. However, the primary and secondary mass distributions share a common m_{\min} parameter in all models we consider. The effect of GW190814 on the mass spectrum at low masses inferred using the BROKEN POWER LAW model is similar.

parameter χ_{eff} quantifies the spin components aligned with the orbital angular momentum (Damour 2001):

$$\chi_{\text{eff}} = \frac{\chi_1 \cos \theta_1 + q \chi_2 \cos \theta_2}{1 + q}. \quad (5)$$

Here, χ_1 and χ_2 are the dimensionless component spins, defined by $\chi_i = |cS_i/(Gm_i^2)|$ where S_i is the spin angular momentum of component i , and θ_1 and θ_2 are the misalignment angles between the component spins and the orbital angular momentum. Second, spins with components perpendicular to the orbital angular momentum drive relativistic precession of the orbital plane (Apostolatos et al. 1994). The effect is quantified by the effective precession spin parameter (Schmidt et al. 2012; Hannam et al. 2014; Schmidt et al. 2015)

$$\chi_p = \max \left[\chi_1 \sin \theta_1, \left(\frac{4q + 3}{4 + 3q} \right) q \chi_2 \sin \theta_2 \right]. \quad (6)$$

A non-zero value of χ_p indicates the presence of relativistic spin-induced precession of the orbital plane. Although the component spin tilts θ_1 and θ_2 appearing in Eqs. (5) and (6) generically evolve over the course of a binary inspiral, χ_{eff} and χ_p are themselves approximately conserved quantities (Kidder 1995; Schmidt et al. 2015).

The first unambiguous measurements of BH spin in gravitational-wave astronomy came from analyses of the BBH event GW151226. This system had $\chi_{\text{eff}} > 0$ at 99% credibility, with at least one of its components having spin magnitude $\chi > 0.2$, and spin misalignment

angles consistent with $\theta_1 = \theta_2 = 0$ (Abbott et al. 2016b). While analyses of GWTC-1 found no clear evidence for spin in the other events in GWTC-1 (Miller et al. 2020, but also see Zackay et al. 2019 and Huang et al. 2020), GWTC-1 is collectively inconsistent with a population of non-spinning BHs, if one allows for both spinning and non-spinning subpopulations (Kimball et al. 2020a). Moreover, population analyses of GWTC-1 mildly disfavor the scenario in which all spins are perfectly aligned ($\theta_1 = \theta_2 = 0$), although the degree of misalignment is degenerate with the spin magnitude distribution (Farr et al. 2017; Farr et al. 2018; Tiwari et al. 2018; Abbott et al. 2019a; Wysocki et al. 2019b).

In GWTC-2, additional BBH events are observed with confidently positive effective inspiral spin parameter. No individual event is observed with confidently negative χ_{eff} (Abbott et al. 2020c). Several events, including GW190521 (Abbott et al. 2020e,f) and GW190412 (Abbott et al. 2020a), show moderate evidence for non-zero χ_p , but no single event unambiguously exhibits spin-induced precession (Abbott et al. 2020c).

Using the DEFAULT model described in Sec. 3 (see also Appendix D.1), we obtain evidence for non-vanishing spin-orbit misalignment among the population of BBH events in GWTC-2. The DEFAULT model describes the distribution of spin-orbit misalignments as a mixture between two components: a component with isotropically-oriented spins and a preferentially-aligned component

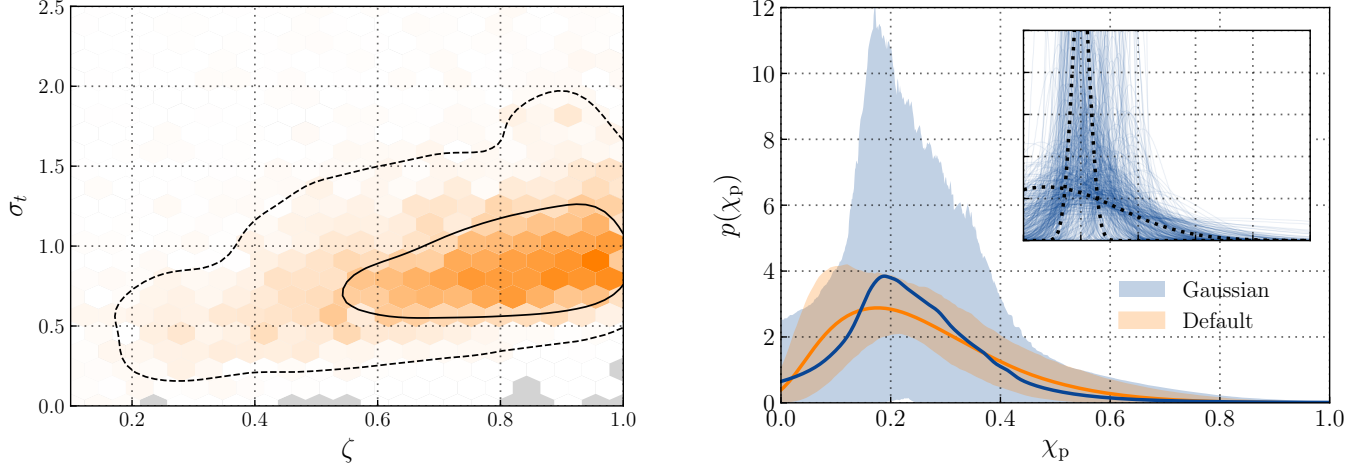


Figure 9. *Left:* Joint posterior on the fraction ζ of BBHs with preferentially-aligned spins (versus isotropic spins) and the spread σ_t of misalignment angles among this population obtained using the DEFAULT spin model (see Appendix D.1 for additional details). We rule out a population with perfectly aligned spins corresponding to $\zeta = 1$ and $\sigma_t = 0$. The gray shaded region represents the region of parameter space inaccessible to our analysis. This region is artificially excluded due to sampling uncertainties even when analyzing uninformative samples drawn from the spin tilt prior. The dashed and solid contours mark the central 50% and 90% posterior credible regions, respectively, assuming a flat prior on ζ and σ_t . *Right:* Population predictive distributions for the effective precession spin parameter χ_p of BBH systems obtained using the GAUSSIAN (blue) and DEFAULT (orange) spin models. Shaded regions show the central 90% credible bounds on $p(\chi_p)$ at a given spin value, while the solid lines show the median posterior prediction. The inset shows draws of the GAUSSIAN χ_p distributions implied by the posterior on μ_p and σ_p . Broadly, we see support for two possible morphologies, indicated schematically by the dashed black curves. GWTC-2 is compatible with a χ_p distribution that is either broad, or one that is narrow and centered at $\mu_p \sim 0.2$.

with $z = \cos \theta$ values centered at $z = 0$ (perfect alignment) with a Gaussian spread of width σ_t . In the left side of Fig. 9, we show the joint posterior on σ_t and the fraction ζ of events in the preferentially-aligned subpopulation. Perfect alignment corresponds to $\zeta = 1$ and $\sigma_t = 0$. We see that this case is ruled out at $> 99\%$ credibility. Thus, either a non-zero fraction of BBH events exhibit isotropically-oriented spins, or BBH spins are preferentially aligned to their orbits but with a non-vanishing spread. Either case constitutes an observation of in-plane spin components among the BBH population. The shaded gray tiles in the left side of Fig. 9 show the values of ζ and σ_t that are artificially excluded by the prior and/or finite sampling effects; the true measurement using GWTC-2 lies well away from this artificial exclusion region.⁷

In Fig. 10, discussed further below, we plot the range of component spin magnitude and tilt angle distributions recovered using the DEFAULT model. Although the data are consistent with tilt angle distributions that

favor alignment, distributions that are highly peaked at $\cos \theta_{1,2} = 1$ are ruled out.

A similar conclusion regarding the presence of in-plane spin components may be drawn using GAUSSIAN spin model, which imposes an entirely different parameterization for the BH spin distribution and makes different assumptions regarding their masses. In particular, when measuring the mean μ_p and standard deviation σ_p of the χ_p distribution, the case $\mu_p = \sigma_p = 0$ is ruled out at $> 99\%$ credibility; fewer than 1% of posterior samples occur at $\mu_p \leq 0.05$ and $\sigma_p \leq 0.05$. Since any non-zero μ_p or σ_p implies the existence of spin-induced precession, this result supports the observation of spin misalignment seen in the DEFAULT model. In the right side of Fig. 9, the dark blue curve and shaded blue region mark the median and 90% credible bound, respectively, on $p(\chi_p)$ as inferred by the GAUSSIAN model. While the blue region in this figure suggests a χ_p distribution that peaks at ~ 0.2 , there are in fact two morphologies preferred by the data according to the GAUSSIAN model: the recovered χ_p distribution is *either* broad—or narrowly peaked at $\chi_p \approx 0.2$. This is illustrated by the inset, in which we plot an ensemble of distributions corresponding to individual draws from the (μ_p, σ_p) posterior; the dashed black curves highlight traces representative of the two permitted morphologies.

⁷ In order to determine the artificial exclusion region, we generate prior samples for tilt angles $\theta_{1,2}$ conditioned on the measured values of mass ratio q and spin magnitudes $\chi_{1,2}$. There are no prior samples in the gray tiles, which indicate that these tiles are artificially excluded due to finite sampling effects.

For comparison, the orange curve in the right side of Fig. 9 shows the χ_p distribution implied by the DEFAULT results discussed above. There are several potentially meaningful differences between the results from the GAUSSIAN and DEFAULT models. In particular, the DEFAULT model predicts χ_p distributions that are generally broader and peaked at lower values. This is due to additional physical constraints imposed by the DEFAULT spin model; component spins are presumed to preferentially cluster about $\theta = 0$, an assumption that preferentially favors smaller χ_p values. Nevertheless, the two models agree well within statistical uncertainties,⁸ indicating that the identification of spin-induced precession is robust to the systematic modeling choices and prior uncertainties.

As mentioned above, GW190521 and GW190412 individually show mild evidence of precession, with χ_p posteriors shifted away from their respective priors (Abbott et al. 2020a,e,f). To verify that our population-level conclusions are not driven primarily by these two events, we have repeated the GAUSSIAN analysis excluding GW190521 and GW190412. Our results again exclude $\mu_p = \sigma_p = 0$ at a similar level of confidence ($> 99\%$ credibility). This implies that the signature of precession observed here is due to the combined influence of many systems with only weakly measured χ_p , consistent with expectations from simulation studies (Fairhurst et al. 2019; Wysocki et al. 2019b).

The injection sets used to quantify search selection effects (see Appendix A) contain only events whose component spins are perfectly aligned with their orbital angular momenta. The results in Fig. 9 therefore *do not* account for systematics possibly affecting our ability to detect events with misaligned spins. The matched filter template banks adopted by the GstLAL and PyCBC search pipelines, for instance, are composed of purely aligned-spin waveforms, and so may have reduced sensitivity to events with high χ_p (Harry et al. 2016; Calderón Bustillo et al. 2017). Selection effects can, however, only *decrease* the efficiency with which events with large in-plane spins are detected; incorporating such effects would further shift the posterior in Fig. 9 away from $\zeta = 1$ and $\sigma_t = 0$ and/or more strongly rule out a delta function at $\chi_p = 0$. Thus, the presence of in-plane spin components is robust to selection effects. The specific preference for $\mu_p \approx 0.2$, though, may not be. In the future, accurately characterizing the effects of in-plane spins on detection efficiency

⁸ For technical reasons, we do not have a Bayes factor to compare the DEFAULT and GAUSSIAN spin models, though, this comparison is possible in principle.

will be crucial in order to robustly determine the shape of the $\cos \theta$ and χ_p distributions.

We observe anti-aligned spin, which may suggest the presence of more than one binary formation channel. Using the GAUSSIAN model described in Sec. 3, we infer the presence of systems with negative effective inspiral spin parameter: $\chi_{\text{eff}} < 0$. Thus, there exist BBH systems with at least one component spin tilted by $\theta > 90^\circ$ relative to the orbital angular momenta. Figure 11 shows posteriors for the mean μ_{eff} and standard deviation σ_{eff} of the χ_{eff} distribution, marginalized over μ_p , σ_p , and the covariance between the effective inspiral spin parameter and the effective precession spin parameter. With a peak at $\mu_{\text{eff}} = 0.06^{+0.05}_{-0.05}$, we find that most systems have small but positive χ_{eff} , in agreement with the inference from GWTC-1 (Miller et al. 2020; Roulet & Zaldarriaga 2019). With GWTC-2, we can now also constrain the width of the χ_{eff} distribution. The result, $\sigma_{\text{eff}} = 0.12^{+0.06}_{-0.04}$, requires that a nonzero fraction of BBH systems have $\chi_{\text{eff}} < 0$. Unlike the constraints on the χ_p distribution presented above, the results for the presence of negative effective inspiral spin parameter *do* incorporate selection effects via the prescription described in Sec. 4.

Analysis with the DEFAULT spin model is also suggestive of an anisotropic distribution of spin orientations. In Fig. 10, we plot the population distribution of $\cos \theta_{1,2}$ reconstructed using the DEFAULT model. While the $\cos \theta_{1,2}$ distribution shows a preference for primarily aligned spins, with $\cos \theta_{1,2} > 0$, it also exhibits non-vanishing posterior support for $\cos \theta_{1,2} < 0$, indicating the presence of component spins misaligned by more than 90° . The χ_{eff} distribution inferred with the DEFAULT model closely matches the distribution inferred using the GAUSSIAN model; compare the orange and blue bands in the right panel of Fig. 11. The two models therefore agree on the fraction of systems with anti-aligned component spins.

To further verify that the apparent presence of events with negative χ_{eff} is physical and not an artifact of our choice of models, we repeat our inference of the GAUSSIAN χ_{eff} distribution, this time permitting the minimum allowed effective inspiral spin parameter $\chi_{\text{eff}}^{\text{min}}$ (until now fixed to $\chi_{\text{eff}}^{\text{min}} = -1$) to vary as an additional hyper-parameter to be inferred from the data. When fitting for $\chi_{\text{eff}}^{\text{min}}$ alongside μ_{eff} and σ_{eff} , we find that $\chi_{\text{eff}}^{\text{min}}$ is less than zero at 99% credibility (see Fig. 27 in the Appendix), confirming that the evidence for anti-aligned spin is not an artifact of our parameterization. Allowing $\chi_{\text{eff}}^{\text{min}}$ to vary yields similar results for the implied χ_{eff} distribution, and in particular, the fraction of systems with negative χ_{eff} .

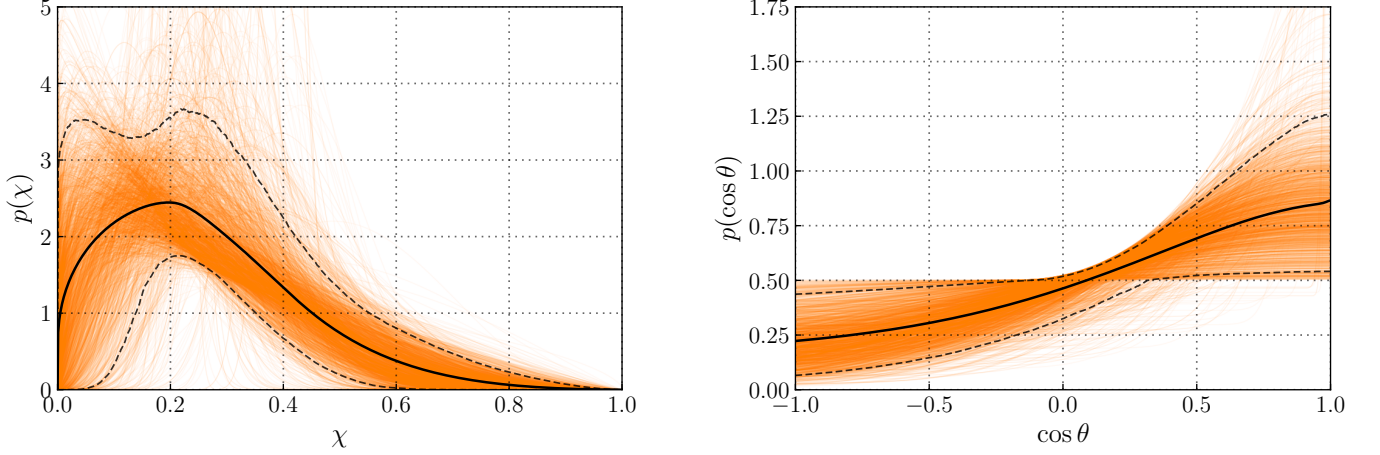


Figure 10. Reconstructions of the BH spin magnitude and tilt distributions. *Left:* The distribution of dimensionless spin magnitude χ as inferred using the DEFAULT spin model (see Appendix D.1). Light traces show individual draws from the DEFAULT posterior, while the solid black curve shows the posterior population distribution for χ . Dashed lines mark the central 90% quantiles. *Right:* the reconstructed distribution of tilt angle $\cos \theta_{1,2}$ of BH component spins relative to the orbital angular momenta. An isotropic spin orientation, which corresponds to a uniform distribution in $\cos \theta_{1,2}$, is disfavored but not ruled out. The data do, however, rule out a highly peaked distribution at $\cos \theta_{1,2} = 1$. Rather, the data are consistent with a gently peaked distribution, with a modest preference for aligned spin ($\cos \theta_{1,2} > 0$).

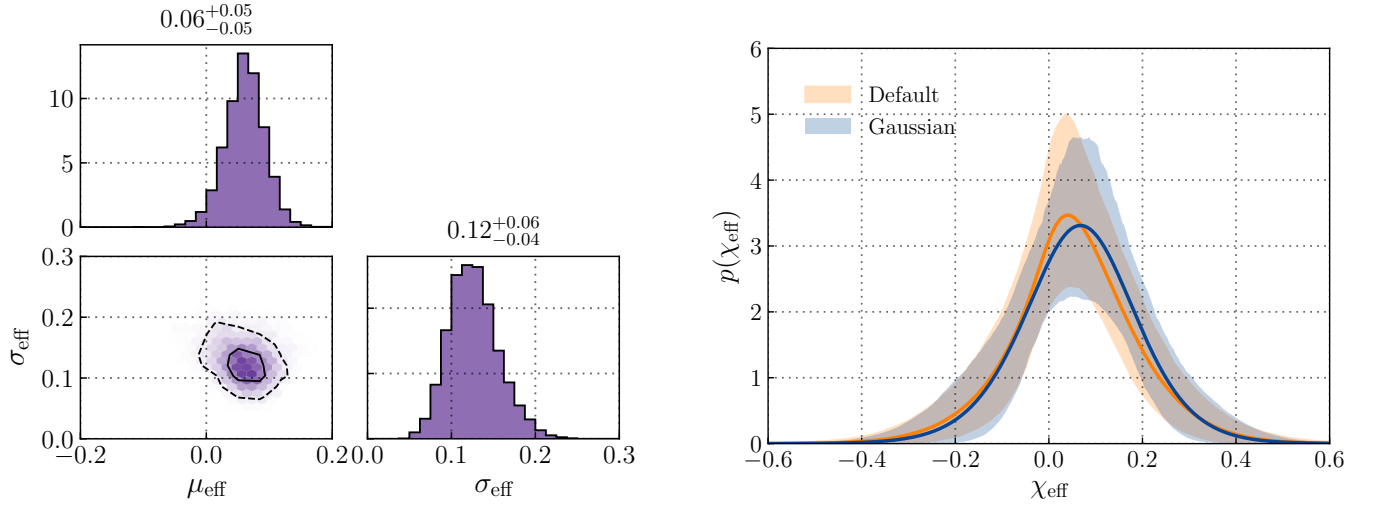


Figure 11. *Left:* Posterior for the mean μ_{eff} and standard deviation σ_{eff} of the BBH χ_{eff} distribution, obtained using the GAUSSIAN model described in Appendix D.2. We marginalize over the parameters governing the distribution of the effective inspiral spin parameter and the effective precession spin parameter. While we infer a χ_{eff} distribution that is peaked at positive values, its measured width implies that a non-zero fraction of BBH systems have negative χ_{eff} , implying component spins misaligned by $t_{1,2} > 90^\circ$ relative to the orbital angular momentum. *Right:* Population predictive distributions for the effective inspiral spin parameter χ_{eff} obtained with both the GAUSSIAN and DEFAULT spin models. Shaded regions show the central 90% credible bounds on $p(\chi_{\text{eff}})$ and the solid lines show the median posterior prediction for the χ_{eff} distribution.

The presence of BBH systems with negative effective inspiral spin parameter carries implications for the formation channels that give rise to stellar-mass BBH mergers. BBHs born in the field from isolated stellar progenitors are predicted to contain components whose spins are nearly aligned with their orbital angular momenta, although sufficiently strong supernova kicks might produce

modest misalignment (O’Shaughnessy et al. 2017; Stevenson et al. 2017; Gerosa et al. 2018; Rodriguez et al. 2016; Bavera et al. 2019). In contrast, binaries assembled dynamically in dense stellar environments are expected to have randomly oriented component spins, yielding positive or negative χ_{eff} with equal probabilities (Kalogera 2000; Mandel & O’Shaughnessy 2010; Rodriguez et al.

2016; Zevin et al. 2017; Rodriguez et al. 2018; Doctor et al. 2019).

Using the posteriors for μ_{eff} and σ_{eff} from Fig. 11, in Fig. 12 we show posteriors for the implied fractions of BBH systems with negative ($\chi_{\text{eff}} < -0.01$) and positive effective inspiral spin parameter ($\chi_{\text{eff}} > 0.01$). Motivated by recent work suggesting that BHs are born with natal spins as small as $\chi \approx 10^{-2}$ (Qin et al. 2018; Fuller et al. 2019; Fuller & Ma 2019; Bavera et al. 2019), as well as the tendency of vanishingly small spins to confound efforts to distinguish between positive and negative χ_{eff} (Farr et al. 2018; Abbott et al. 2019a), we include a third bin containing vanishingly small spins between $-0.01 \leq \chi_{\text{eff}} \leq 0.01$. At 90% credibility, we find that fractions $f_p = 0.67^{+0.16}_{-0.16}$, $f_n = 0.27^{+0.17}_{-0.15}$, and $f_v = 0.05^{+0.02}_{-0.01}$ of BBH systems have positive, negative, and vanishing χ_{eff} , respectively. All three posterior distributions are peaked away from zero. In particular, $f_n > 7\%$ at 99% credibility. This result is in contrast to results obtained using GWTC-1 alone, which did not exhibit a confidently non-zero fraction of events with negative χ_{eff} (Abbott et al. 2019a; Miller et al. 2020). Additionally, the relatively small fraction f_v of binaries with vanishing spins may provide clues about how BHs gain angular momentum, given recent studies suggesting that most BHs are born slowly rotating (Fuller & Ma 2019). While we define the vanishing bin to be $-0.01 \leq \chi_{\text{eff}} \leq 0.01$, the exact choice of width for the vanishing bin does not strongly affect the values of f_p and f_n , relative to one another. We obtain nearly identical results, albeit with a slightly weaker lower bound on f_n , when we additionally allow the minimum effective inspiral spin $\chi_{\text{eff}}^{\text{min}}$ to vary as described above; in this case $f_p = 0.65^{+0.17}_{-0.16}$ and $f_n = 0.26^{+0.17}_{-0.21}$.

As mentioned above, dynamical formation in dense clusters is not the only astrophysical explanation of negative effective inspiral spin parameter. If stellar progenitors experience both strong natal kicks in supernovae and inefficient spin realignment, $\lesssim 10\%$ of BBH systems formed through isolated binary evolution may have $\chi_{\text{eff}} < 0$ (Rodriguez et al. 2016; O’Shaughnessy et al. 2017; Stevenson et al. 2017; Wysocki et al. 2018), although these results depend on the poorly understood physics of natal kicks and binary interaction via torques and mass transfer. Moreover, we have so far neglected the possibility of other formation channels that may operate in both the field and dynamical regimes. Isolated hierarchical triples, for example, may produce binary mergers with preferentially in-plane component spins (Rodriguez & Antonini 2018; Antonini et al. 2018; Liu et al. 2019; Fragione & Kocsis 2020). Mergers in the disks of active galactic nuclei, meanwhile, yield component spins that are preferentially parallel or anti-parallel to a binary’s

orbital angular momentum (McKernan et al. 2018; Yang et al. 2019; McKernan et al. 2020).

With these qualifications in mind, if we interpret negative χ_{eff} as indicative of dynamical formation in stellar clusters, then our constraints on f_n can be used to infer the fraction of dynamically assembled binaries. We assume that dynamical assembly in dense stellar environments yields a χ_{eff} distribution that is symmetric about zero, while isolated binary evolution produces only *positive* χ_{eff} . Among the binaries with non-negligible spin (excluding those in the “vanishing” category above), the fractions f_d and f_i of binaries arising from dynamical and isolated channels are

$$f_d = \frac{2f_n}{f_p + f_n}, \quad (7)$$

$$f_i = \frac{f_p - f_n}{f_p + f_n}. \quad (8)$$

We find $0.25 \leq f_d \leq 0.93$ at 90% credibility, suggesting that both the field and the dynamical cluster scenarios contribute to the BBH mergers observed in GWTC-2. Because the relative values of f_n and f_p are not sensitive to the width of the vanishing χ_{eff} bin, this conclusion does not depend strongly on the definition of vanishing spin.

At present, we are unable to include a systematic investigation of waveform error in our analysis of anti-aligned spin and orbital precession. However, preliminary studies suggest that waveform error is unlikely to significantly affect this and other results in this paper. As described in Abbott et al. (2020c), there is good agreement regarding the parameters of the GWTC-2 events when inferred with different waveforms. There is a caveat: our studies do not include eccentric waveforms. Romero-Shaw et al. (2020a); Gayathri et al. (2020) suggest that GW190521 may have been eccentric and Calderón Bustillo et al. (2020) point out that eccentricity can be confused with precession for high-mass events. Currently the only event likely to be affected is GW190521 (Calderón Bustillo et al. 2020). It is not clear how our results would change if we accounted for eccentricity, but we note that eccentricity can be a signature of dynamical assembly (Samsing et al. 2014; Samsing & Ramirez-Ruiz 2017; Samsing 2018; Romero-Shaw et al. 2019; Lower et al. 2018; Fragione & Kocsis 2019; Zevin et al. 2019). We also note that Fishbach & Holz (2020a); Nitz & Capano (2020) find that GW190521 may be an intermediate mass ratio inspiral, which could potentially alter our conclusions if true. For future work, it would be worthwhile to estimate the systematic error using different waveform approximants.

No strong evidence for variation of the spin distribution with mass. BHs born in hierarchical mergers

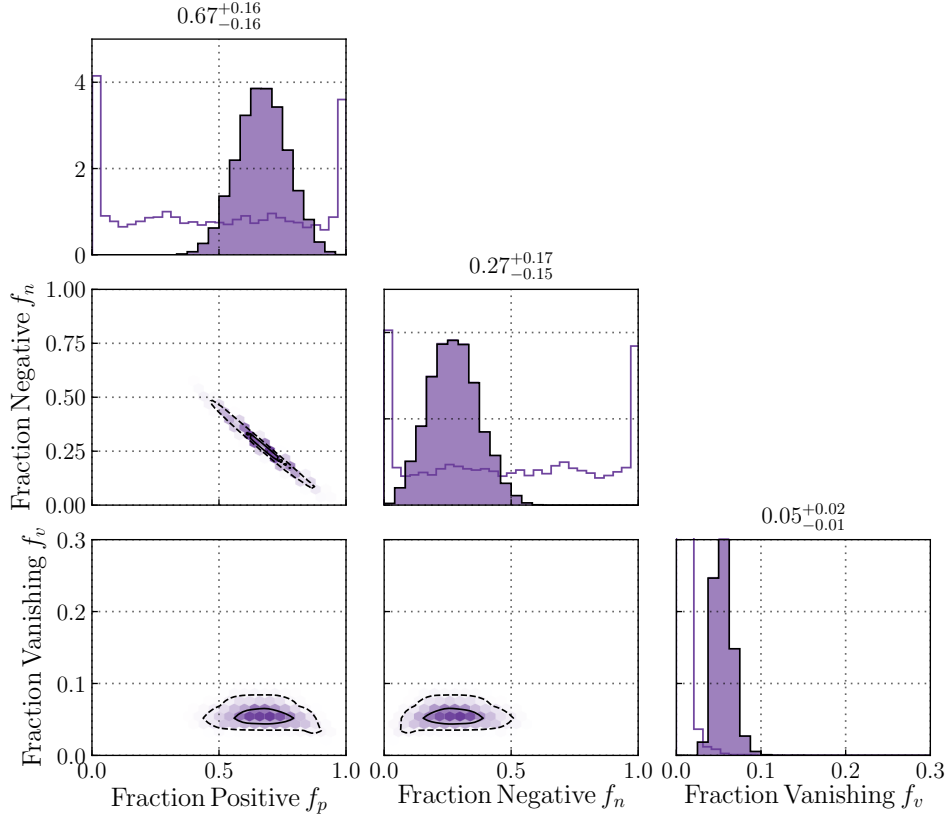


Figure 12. Posterior distribution for the fraction of BBH events with positive or negative χ_{eff} (corresponding to alignment or anti-alignment of the BH spin with the orbital angular momentum; see Eq. 5). We also include the fraction of events that is consistent with vanishingly small spins $|\chi_{\text{eff}}| < 0.01$. We confidently infer that a nonzero fraction of events have positive χ_{eff} , which requires at least one component to have spin tilt less than 90° . A smaller fraction of events have negative χ_{eff} , which requires at least one component with spin tilt $> 90^\circ$. A nonzero fraction of events have vanishingly small spins. The *prior* distributions on the parameters are marked with the non-filled histograms.

inherit the orbital angular momenta of their progenitor systems, leading to significant spin magnitudes $\chi \approx 0.7$ for nearly equal-mass systems (Pretorius 2005; Berti & Volonteri 2008; Fishbach et al. 2017; Gerosa et al. 2018; Doctor et al. 2019; Rodriguez et al. 2018, 2019; Kimball et al. 2020a). If hierarchical mergers are present in GWTC-2, then one may expect correlations between the spins and masses of BBH systems, with more massive hierarchical mergers also possessing larger spins. We use the MULTI SPIN model to explore possible trends in the BBH spin distribution with mass, allowing for a distinct low-mass and high-mass subpopulation (with primary mass distributions parameterized by a power-law and Gaussian, respectively; see Sec. D.3), each with a distinct spin distribution. The low-mass power-law has a weak preference for smaller spins, as compared to the high-mass Gaussian. Both subpopulations disfavor perfectly aligned systems, though the low-mass subpopulation has more support for small misalignments. In spite of these differences, the uncertainties on both of these subpopulations are broad enough that the two are fully consistent

with each other, and we cannot confidently claim to detect a mass-dependence to the spin distribution at this stage. This is demonstrated in Fig. 13, which shows the posteriors for the spin distribution hyper-parameters associated with each mass subpopulation. These findings support the results of previous studies on GWTC-1, which could neither exclude nor confidently detect variation of the spin distribution with mass (Safarzadeh et al. 2020; Tiwari 2020).

5.3. Merger rate and redshift evolution

In this subsection we use the POWER LAW + PEAK and BROKEN POWER LAW mass models with the DEFAULT spin model, and infer the merger rate using the NON-EVOLVING redshift model and the POWER-LAW evolution redshift model.

We better constrain the binary black hole merger rate. Assuming a log-uniform prior, we find a BBH merger rate of $R_{\text{BBH}} = 23.9^{+14.3}_{-8.6} \text{ Gpc}^{-3} \text{ yr}^{-1}$ using the POWER LAW + PEAK mass distribution and the assumption of a NON-EVOLVING merger rate den-

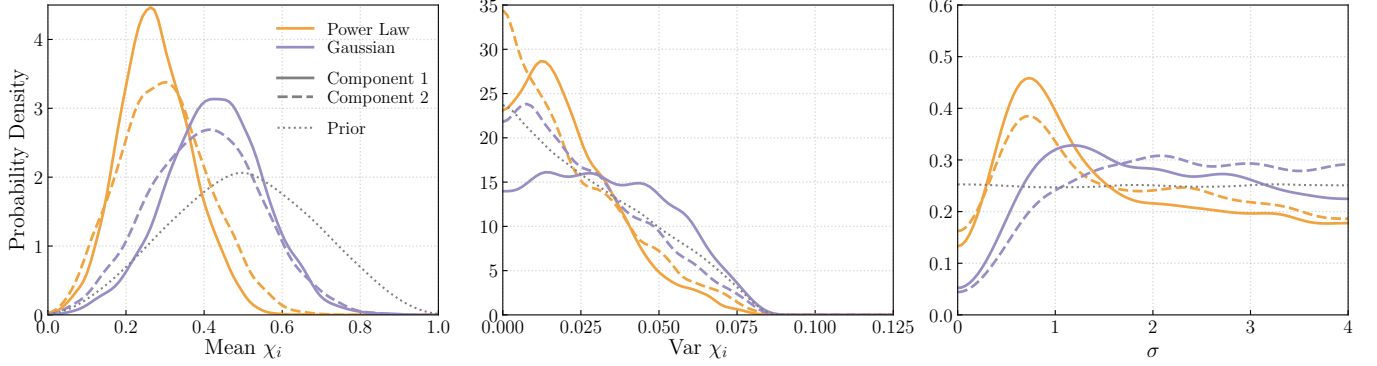


Figure 13. Posterior distribution for MULTI SPIN spin hyper-parameters. Each subplot corresponds to a different parameter controlling the shape of the spin distribution (see Appendix D.3 for details). Each color corresponds to a different subpopulation (power-law or Gaussian) or component (primary mass or secondary mass) of the binary. The power-law subpopulation is slightly better measured than the Gaussian component, as a large number of detections are assigned to it. The results hint at a potential correlation between mass and spin, but the large measurement errors mean the spin distributions are consistent between the two subpopulations.

sity. We find that estimates of the BBH merger rate are robust to our choice of mass model, with excellent agreement between the POWER LAW + PEAK, BROKEN POWER LAW, and MULTI PEAK models. The TRUNCATED model yields a higher merger rate than the other models, but the results agree within statistical uncertainties: $R_{\text{BBH}} = 33^{+22}_{-12} \text{ Gpc}^{-3} \text{ yr}^{-1}$. Our BBH merger rate estimate is consistent with the hypothesis that a significant fraction of the merger rate is due to dynamically assembled binaries in globular clusters (Portegies Zwart & McMillan 2000; O’Leary et al. 2006; Moody & Sigurdsson 2009; Downing et al. 2011; Rodriguez et al. 2015; Park et al. 2017; Fragione & Kocsis 2018; Antonini & Gieles 2020), young/open star clusters (Banerjee et al. 2010; Ziosi et al. 2014), nuclear star clusters (O’Leary et al. 2009; Miller & Lauburg 2009; Antonini & Rasio 2016), or active galactic nuclei discs (McKernan et al. 2018; Tagawa et al. 2020; Gröbner et al. 2020).

In Table 4, we show the merger rate in different primary mass bins, as inferred with the BROKEN POWER LAW, POWER LAW + PEAK and MULTI PEAK models. Taking the range between the lowest 5% and highest 95% estimate across these three models in each mass bin, we find the merger rate to be $\sim 4\text{--}14 \text{ Gpc}^{-3} \text{ yr}^{-1}$ in the range of $10\text{--}20 M_{\odot}$, $\sim 1.3\text{--}5.3 \text{ Gpc}^{-3} \text{ yr}^{-1}$ in the range of $20\text{--}30 M_{\odot}$, and $\sim 1.3\text{--}5.2 \text{ Gpc}^{-3} \text{ yr}^{-1}$ in the range of $30\text{--}40 M_{\odot}$. In Fig. 7, we showed that the primary mass spectrum turns over between $4\text{--}10 M_{\odot}$. We estimate the merger rate in this range to be $\sim 3\text{--}21 \text{ Gpc}^{-3} \text{ yr}^{-1}$.

Our estimate of the BBH merger rate include only systems with $m_1 \geq m_2 > 3 M_{\odot}$, which notably excludes GW190814. If we calculate the merger rate for all systems down to $m_2 \geq 2 M_{\odot}$ using our models, thereby including GW190814, we infer a higher merger rate:

$R_{\text{BBH}} = 52^{+52}_{-26} \text{ Gpc}^{-3} \text{ yr}^{-1}$ for the POWER LAW + PEAK model. The reason for this change is that including GW190814 increases the low-mass rate (see Fig. 8b). However, because our mass distribution models do not extrapolate well to $m_2 < 3 M_{\odot}$ (see Section 5.1), the fit with GW190814 likely overestimates the rate of systems with masses between $\sim 2.6 M_{\odot}$ and $\sim 6 M_{\odot}$. Because of the uncertainty regarding the nature of GW190814 and the low significance of GW190426_152155 (the other NSBH candidate in GWTC-2), we do not attempt to model the NSBH mass distribution, and do not calculate an NSBH merger rate. An estimate of the merger rate for GW190814-like systems can be found in Abbott et al. (2020b).

We update the binary neutron star merger rate. We give an update to the BNS rate based on the two confident BNS detections in GWTC-2, GW170817 and GW190425. We estimate a rate $\mathcal{R}_{\text{BNS}} = 320^{+490}_{-240} \text{ Gpc}^{-3} \text{ yr}^{-1}$ by Monte-Carlo sampling from a non-spinning distribution of systems, with component masses uniformly distributed between $1 M_{\odot}$ and $2.5 M_{\odot}$,⁹ and uniformly distributed in comoving volume and detector-frame time with isotropic orientations and sky locations. The detectability of each simulated system was approximated by requiring a network signal-to-noise ratio above 10 with signal-to-noise ratios above 5 in at least two detectors. Because of the longer observing time and the lack of additional detections, we find a slightly smaller value for the BNS rate than previously reported: $R_{\text{BNS}} = 320^{+490}_{-240} \text{ Gpc}^{-3} \text{ yr}^{-1}$. Assuming that there are 0.01 Milky Way equivalent galaxies (MWEg)

⁹ See Farrow et al. (2019); Galadage et al. (2020) for fits to the mass distribution of Galactic BNSs.

Mass model	$\mathcal{R} [\text{Gpc}^{-3} \text{yr}^{-1}]$			
	$4 M_{\odot} \leq m_1 < 10 M_{\odot}$	$10 M_{\odot} < m_1 < 20 M_{\odot}$	$20 M_{\odot} \leq m_1 < 30 M_{\odot}$	$30 M_{\odot} \leq m_1 < 40 M_{\odot}$
BROKEN POWER LAW	$7.86^{+11.17}_{-4.81}$	$8.89^{+5.29}_{-3.57}$	$3.71^{+1.58}_{-1.1}$	$2.04^{+1.16}_{-0.78}$
POWER LAW + PEAK	$8.91^{+11.28}_{-5.25}$	$7.07^{+4.58}_{-2.98}$	$2.75^{+1.94}_{-1.14}$	$3.05^{+1.86}_{-1.13}$
MULTI PEAK	$9.54^{+11.48}_{-5.78}$	$7.02^{+4.54}_{-3.06}$	$2.6^{+1.88}_{-1.3}$	$3.19^{+2.02}_{-1.22}$

Table 4. Merger rate estimate in different primary mass bins. These results assume a NON-EVOLVING merger rate density, and exclude GW190814 from the analysis.

in 1 Mpc^3 (Kopparapu et al. 2008), this implies a rate of $R_{\text{BNS}} = 32^{+49}_{-24} \text{ MWEg}^{-1} \text{ Myr}^{-1}$.

The BBH merger rate probably increases with redshift, but slower than the star-formation rate. Figure 14 shows the merger rate as a function of redshift using the POWER LAW evolution model (see Appendix E for additional details, and Fig. 30 for a posterior predictive check). When we allow the merger rate to evolve with redshift according to $(1+z)^\kappa$, we find that the $z=0$ merger rate is $\mathcal{R}(z=0) = 19.3^{+15.1}_{-9.0} \text{ Gpc}^{-3} \text{ yr}^{-1}$. The posterior for the rate evolution parameter κ is shown in Fig. 15. Since GWTC-2 includes events with greater redshifts than the events in GWTC-1, we obtain a much tighter constraint on the evolution of the merger rate; compare our updated constraints of $\kappa = 1.3^{+2.1}_{-2.1}$ (POWER LAW + PEAK model) and $\kappa = 1.8^{+2.1}_{-2.2}$ (BROKEN POWER LAW model) to the GWTC-1 result of $\kappa = 8.4^{+9.6}_{-9.5}$. We find that the merger rate is consistent with a non-evolving distribution ($\kappa = 0$), but is more likely to increase with increasing redshift, with $\kappa > 0$ at 85% credibility (POWER LAW + PEAK model) or 91% (BROKEN POWER LAW model).

Locally ($z \approx 0$), the Madau–Dickinson star-formation rate (Madau & Dickinson 2014) corresponds to $\kappa = 2.7$ in our POWER-LAW REDSHIFT parameterization. We infer $\kappa < 2.7$ at 86% credibility with the POWER LAW + PEAK mass model (77% with BROKEN POWER LAW). Another way of comparing our inferred merger rate to the star-formation rate is by looking at the ratio between the rate at $z=1$ and $z=0$, $\mathcal{R}_{\text{BBH}}(z=1)/\mathcal{R}_{\text{BBH}}(z=0)$. For the star-formation rate $\mathcal{R}_{\text{SFR}}(z=1)/\mathcal{R}_{\text{SFR}}(z=0) \approx 6$, while for BBH systems, we infer $\mathcal{R}_{\text{BBH}}(z=1)/\mathcal{R}_{\text{BBH}}(z=0) = 2.5^{+8.0}_{-1.9}$ (POWER LAW + PEAK model). These results are consistent with most astrophysical formation channels, which predict a factor of ~ 2 increase between the merger rate at $z=0$ and $z=1$ (Santoliquido et al. 2020; Dominik et al. 2013; Neijssel et al. 2019; Eldridge et al. 2019; Mapelli et al. 2017; Baibhav et al. 2019; Rodriguez & Loeb 2018).

6. CONCLUSIONS

The publication of the second LIGO–Virgo gravitational-wave transient catalog has increased the population of BBH events by a factor of more than four. The new

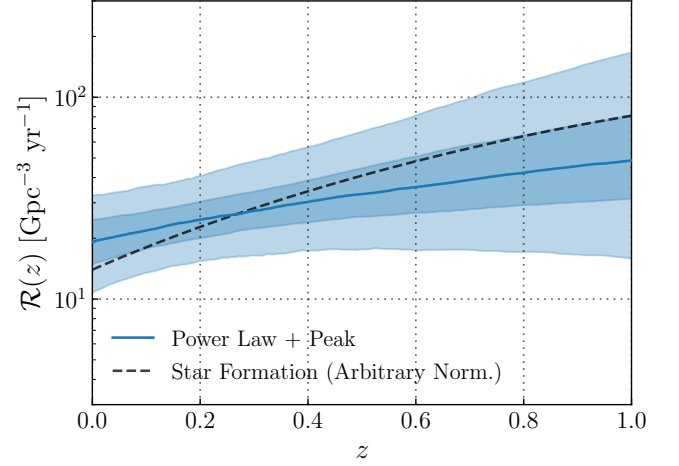


Figure 14. Merger rate density as a function of redshift, fit to the POWER-LAW EVOLUTION model. The solid curve shows the median rate density, while the dark (light) shaded region shows 50% (90%) credible intervals. The dashed curve shows the shape of the SFR. The data exhibit a mild preference for the merger rate to increase with redshift, but are consistent with a flat distribution as well as one that tracks the SFR.

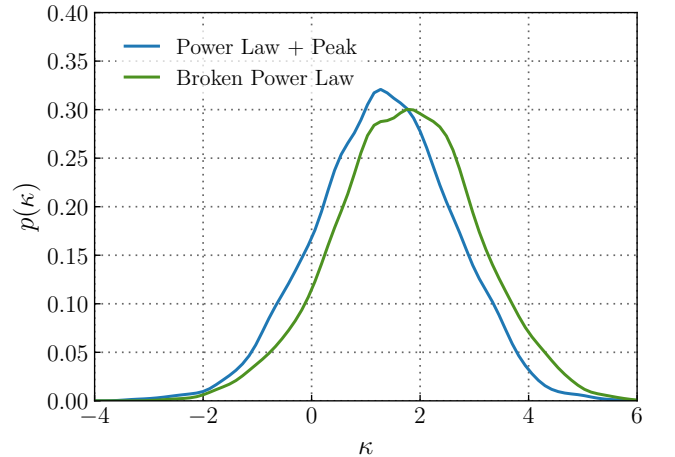


Figure 15. Posterior for the redshift evolution parameter κ from the POWER-LAW EVOLUTION model, which assumes that rate density scales like $(1+z)^\kappa$. We assume the POWER LAW + PEAK and BROKEN POWER LAW mass models, and take a flat prior on κ .

catalog has highlighted the limitations of some early population models while yielding remarkable new signatures:

1. We find that the BBH primary mass spectrum is not well-described as a simple power-law with an abrupt cut-off; there is a strong statistical preference for other models with non-trivial features such as a peak or a tapering. These features occur at $\approx 37 M_\odot$, where one might expect pair instability supernovae (and pulsational pair-instability supernovae) to shape the mass distribution of BHs.
2. At the opposite end of the spectrum, we observe a dearth of systems between NS and BH masses, suggesting that the BH mass spectrum likely turns over at $\sim 7.8_{-2.0}^{+1.8} M_\odot$. We constrain the minimum mass of BHs in BBH systems to be $m_{\min} \lesssim 5.7 M_\odot$ at 90% credibility. This is greater than the mass of BH candidates in Galactic binaries, e.g., [Thompson et al. \(2019\)](#). These results hold only when we restrict our analysis to events with both component masses above $3 M_\odot$.
3. Meanwhile, we find that our models fail to fit GW190814 together with the BBH systems with both components above $3 M_\odot$. This may indicate that GW190814 belongs to a distinct population, or that there are additional features at the low mass end of the BBH mass spectrum that are missing in our models. This is perhaps unsurprising as the combination of mass ratio, merger rate, and secondary mass inferred from this system pose a challenge to our current understanding of compact binary formation ([Abbott et al. 2020b](#); [Arca Sedda 2020b](#); [Zevin et al. 2020](#); [Safarzadeh 2020](#)).
4. We detect clear evidence of spin-induced, general relativistic precession of the orbital plane. We determine that this signature is not due to a single precessing merger, but from the overall preference of the data for precessing waveforms.
5. We observe that some fraction of the BHs in GWTC-2 are spinning with an orientation that is anti-aligned with respect to the orbital angular momentum of the binary. If we plausibly assume that all binaries with anti-aligned spins are assembled dynamically, this may imply that LIGO–Virgo events merge both dynamically and in the field. Based on the inferred mass and spin distributions, we find no clear evidence for or against hierarchical mergers in GWTC-2.

6. We compute the rate of compact binary mergers, finding $\mathcal{R}_{\text{BNS}} = 320_{-240}^{+490} \text{ Gpc}^{-3} \text{ yr}^{-1}$ and $\mathcal{R}_{\text{BBH}} = 23.9_{-8.6}^{+14.3} \text{ Gpc}^{-3} \text{ yr}^{-1}$. The data are consistent with both a merger rate that is constant in time and one that tracks the SFR in the local universe, though the data prefer a merger rate that is somewhere in between. We find that the merger rate at $z = 1$ differs from the merger rate at $z = 0$ by a factor of $\mathcal{R}_{\text{BBH}}(z = 1)/\mathcal{R}_{\text{BBH}}(z = 0) = 2.5_{-1.9}^{+8.0}$, to be compared with the SFR, $\mathcal{R}_{\text{SFR}}(z = 1)/\mathcal{R}_{\text{SFR}}(z = 0) \sim 6$.

While a clearer picture is emerging of the population properties of compact binaries, key questions remain. How do we best characterize the deviations from power-law in the primary BH mass spectrum, and what is the physical origin of these new features? What is the origin of BBH mergers in the high-mass gap: hierarchical mergers, stars producing remnants heavier than expected from pair instability supernovae theory, or something else? What is the shape of the mass spectrum between NS and BH masses, and does the current dearth of systems between $\sim 3 M_\odot$ and $\sim 6 M_\odot$ represent an empty low-mass gap? If so, do systems like the secondary mass of GW190814 belong to the NS or BH side of the gap? Is the observation of anti-aligned spins indicative of dynamically assembled binaries? As the sensitivity of LIGO, Virgo, and KAGRA improves, and as more gravitational-wave transients are detected, we expect to begin to answer these questions. As future observations subject our models to increasing scrutiny, it is inevitable that refinements will be required to fit newly resolved features. This cycle of refining models to account for new data will reveal new questions while providing an evolving understanding of the conclusions presented here.

The authors gratefully acknowledge the support of the United States National Science Foundation (NSF) for the construction and operation of the LIGO Laboratory and Advanced LIGO as well as the Science and Technology Facilities Council (STFC) of the United Kingdom, the Max-Planck-Society (MPS), and the State of Niedersachsen/Germany for support of the construction of Advanced LIGO and construction and operation of the GEO600 detector. Additional support for Advanced LIGO was provided by the Australian Research Council. The authors gratefully acknowledge the Italian Istituto Nazionale di Fisica Nucleare (INFN), the French Centre National de la Recherche Scientifique (CNRS) and the Netherlands Organization for Scientific Research, for the construction and operation of the Virgo detector and the creation and support of the EGO consortium. The authors also gratefully acknowledge research support

from these agencies as well as by the Council of Scientific and Industrial Research of India, the Department of Science and Technology, India, the Science & Engineering Research Board (SERB), India, the Ministry of Human Resource Development, India, the Spanish Agencia Estatal de Investigación, the Vicepresidència i Conselleria d'Innovació, Recerca i Turisme and the Conselleria d'Educació i Universitat del Govern de les Illes Balears, the Conselleria d'Innovació, Universitats, Ciència i Societat Digital de la Generalitat Valenciana and the CERCA Programme Generalitat de Catalunya, Spain, the National Science Centre of Poland, the Swiss National Science Foundation (SNSF), the Russian Foundation for Basic Research, the Russian Science Foundation, the European Commission, the European Regional Development Funds (ERDF), the Royal Society, the Scottish Funding Council, the Scottish Universities Physics Alliance, the Hungarian Scientific Research Fund (OTKA), the French Lyon Institute of Origins (LIO), the Belgian Fonds de la Recherche Scientifique (FRS-FNRS), Actions de Recherche Concertées (ARC) and Fonds Wetenschappelijk Onderzoek – Vlaanderen (FWO), Belgium,

the Paris Île-de-France Region, the National Research, Development and Innovation Office Hungary (NKFIH), the National Research Foundation of Korea, Industry Canada and the Province of Ontario through the Ministry of Economic Development and Innovation, the Natural Science and Engineering Research Council Canada, the Canadian Institute for Advanced Research, the Brazilian Ministry of Science, Technology, Innovations, and Communications, the International Center for Theoretical Physics South American Institute for Fundamental Research (ICTP-SAIFR), the Research Grants Council of Hong Kong, the National Natural Science Foundation of China (NSFC), the Leverhulme Trust, the Research Corporation, the Ministry of Science and Technology (MOST), Taiwan and the Kavli Foundation. The authors gratefully acknowledge the support of the NSF, STFC, INFN and CNRS for provision of computational resources.

We would like to thank all of the essential workers who put their health at risk during the COVID-19 pandemic, without whom we would not have been able to complete this work.

This is LIGO document number LIGO-P2000077.

REFERENCES

- Aasi, J., et al. 2015, CQGra, 32, 074001
- Abbott, B., Abbott, R., Abbott, T., et al. 2013, Prospects for Observing and Localizing Gravitational-Wave Transients with Advanced LIGO, Advanced Virgo and KAGRA, arXiv:1304.0670
- . 2016a, PhRvD, 94, 064035
- . 2016b, PhRvL, 116, 241103
- . 2016c, PhRvL, 116, 241102
- . 2019a, ApJL, 882, L24
- . 2019b, PhRvX, 9, 031040
- . 2019c, arXiv:1912.11716
- Abbott, R., Abbott, T., Abraham, S., et al. 2020a, arXiv:2004.08342
- . 2020b, ApJL, 896, L44
- . 2020c, arXiv e-prints, arXiv:2010.14527
- Abbott, R., et al. 2020d
- . 2020e, PhRvL, 125, 101102
- . 2020f, ApJL, 900, L13
- Acernese, F., et al. 2015, CQGra, 32, 024001
- Adams, T., Buskulic, D., Germain, V., et al. 2016, Classical and Quantum Gravity, 33, 175012
- Allen, B. 2005, PhRvD, 71, "062001"
- Allen, B., Anderson, W. G., Brady, P. R., Brown, D. A., & Creighton, J. D. E. 2012, PhRvD, 85, "122006"
- Antonini, F., & Gieles, M. 2020, arXiv e-prints, arXiv:2009.01861
- Antonini, F., Murray, N., & Mikkola, S. 2014, ApJ, 781, 45
- Antonini, F., & Rasio, F. A. 2016, ApJ, 831, 187
- Antonini, F., Rodriguez, C. L., Petrovich, C., & Fischer, C. L. 2018, Mon. Not. R. Ast. Soc. Lett., 480, L58
- Antonini, F., Toonen, S., & Hamers, A. S. 2017, ApJ, 841, 77
- Apostolatos, T. A., Cutler, C., Sussman, G. J., & Thorne, K. S. 1994, PhRvD, 49, 6274
- Arca Sedda, M. 2020a, ApJ, 891, 47
- . 2020b, Communications Physics, 3, 43
- Arca Sedda, M., Mapelli, M., Spera, M., Benacquista, M., & Giacobbo, N. 2020, ApJ, 894, 133
- Ashton, G., & Thrane, E. 2020, Mon. Not. Roy. Astron. Soc., 498, 1905
- Ashton, G., Hübner, M., Lasky, P. D., et al. 2019, ApJS, 241, 27
- Babak, S., Taracchini, A., & Buonanno, A. 2017, Phys. Rev. D, 95, 024010
- Baibhav, V., Berti, E., Gerosa, D., et al. 2019, PhRvD, 100, 064060
- Bailyn, C., Jain, R. K., Coppi, P., & Orosz, J. A. 1998, ApJ, 499, 367
- Banerjee, S., Baumgardt, H., & Kroupa, P. 2010, MNRAS, 402, 371

- Barkat, Z., Rakavy, G., & Sack, N. 1967, *PhRvL*, 18, 379
- Bartos, I., Kocsis, B., Haiman, Z., & Márka, S. 2017, *ApJ*, 835, 165
- Bavera, S. S., Fragos, T., Qin, Y., et al. 2019, *A&A*, 635, A97
- Belczynski, K., Kalogera, V., & Bulik, T. 2002, *ApJ*, 572, 407
- Belczynski, K., Heger, A., Gladysz, W., et al. 2016, *A&A*, 594, A97
- Belczynski, K., Klencki, J., Fields, C. E., et al. 2020, *A&A*, 636, A104
- Berti, E., & Volonteri, M. 2008, *ApJ*, 684, 822
- Bethe, H. A., & Brown, G. E. 1998, *ApJ*, 506, 780
- Biscoveanu, S., Isi, M., Vitale, S., & Varma, V. 2020, *arXiv:2007.09156*
- Bohé, A., Hannam, M., Husa, S., et al. 2016
- Bohé, A., et al. 2017, *PhRvD*, 95, 044028
- Calderón Bustillo, J., Sanchis-Gual, N., Torres-Forné, A., & Font, J. A. 2020, *arxiv/2009.01066*
- Calderón Bustillo, J., Laguna, P., & Shoemaker, D. 2017, *Physical Review D*, 95, doi:10.1103/physrevd.95.104038
- Canton, T. D., et al. 2014, *PhRvD*, 90, 082004
- Carlo, U. D., et al. 2019a, *arxiv/1911.01434*
- . 2019b, *MNRAS*, 487, 2947
- Carpenter, B., Gelman, A., Hoffman, M. D., et al. 2017, *Journal of Statistical Software*, 76, doi:10.18637/jss.v076.i01
- Carr, B., Kühnel, F., & Sandstad, M. 2016, *PhRvD*, 94, 083504
- Carr, B. J., & Hawking, S. W. 1974, *MNRAS*, 168, 399
- Chatziioannou, K., et al. 2019, *PhRvD*, 100, 104015
- Chu, Q. 2017, PhD thesis, The University of Western Australia
- Croon, D., McDermott, S. D., & Sakstein, J. 2020, *arXiv:2007.07889*
- Dai, L., Venumadhav, T., & Sigurdson, K. 2017, *PhRvD*, D95, 044011
- Damour, T. 2001, *PhRvD*, 64, 124013
- de Mink, S. E., & Mandel, I. 2016, *MNRAS*, 460, 3545
- Doctor, Z., Wysocki, D., O’Shaughnessy, R., Holz, D. E., & Farr, B. 2019, *ApJ*, 893, 35
- Dominik, M., Belczynski, K., Fryer, C., et al. 2013, *ApJ*, 779, 72
- Dominik, M., Berti, E., O’Shaughnessy, R., et al. 2015, *apj*, 806, 263
- Downing, J. M. B., Benacquista, M. J., Giersz, M., & Spurzem, R. 2011, *MNRAS*, 416, 133
- Eldridge, J. J., Stanway, E. R., & Tang, P. N. 2019, *MNRAS*, 482, 870
- Eldridge, J. J., Stanway, E. R., Xiao, L., et al. 2017, *PASA*, 34, e058
- Essick, R., & Landry, P. 2020, *arXiv:2007.01372*
- Fairhurst, S., Green, R., Hannam, M., & Hoy, C. 2019, *arXiv:1908.00555*
- Farmer, R., Renzo, M., de Mink, S., Fishbach, M., & Justham, S. 2020, *arXiv e-prints*, *arXiv:2006.06678*
- Farmer, R., Renzo, M., de Mink, S. E., Marchant, P., & Justham, S. 2019, *ApJ*, 887, 53
- Farr, B., Holz, D. E., & Farr, W. M. 2018, *ApJL*, 854, L9
- Farr, W. M. 2019, *Research Notes of the American Astronomical Society*, 3, 66
- Farr, W. M., Sravan, N., Cantrell, A., et al. 2011, *ApJ*, 741, 103
- Farr, W. M., Stevenson, S., Coleman Miller, M., et al. 2017, *Nature*, 548, 426
- Farrell, E. J., Groh, J. H., Hirschi, R., et al. 2020, *arXiv:2009.06585*
- Farrow, N., Zhu, X.-J., & Thrane, E. 2019, *ApJ*, 876, 18
- Fernandez, N., & Profumo, S. 2019, *JCAP*, 2019, 022
- Fishbach, M., Essick, R., & Holz, D. E. 2020a, *arXiv:2006.13178*
- Fishbach, M., Farr, W. M., & Holz, D. E. 2020b, *ApJL*, 891, L31
- Fishbach, M., & Holz, D. E. 2017, *ApJL*, 851, L25
- Fishbach, M., & Holz, D. E. 2020a, *ApJL*, 904, L26
- . 2020b, *ApJL*, 891, L27
- Fishbach, M., Holz, D. E., & Farr, B. 2017, *ApJL*, 840, L24
- Fishbach, M., Holz, D. E., & Farr, W. M. 2018, *ApJL*, 863, L41
- Foreman-Mackey, D., Hogg, D. W., Lang, D., & Goodman, J. 2013, *Publ. Astron. Soc. Pac.*, 125, 306
- Fowler, W. A., & Hoyle, F. 1964, *ApJS*, 9, 201
- Fragione, G., Grishin, E., Leigh, N. W. C., Perets, H. B., & Perna, R. 2019, *MNRAS*, 488, 47
- Fragione, G., & Kocsis, B. 2018, *PhRvL*, 121, 161103
- . 2019, *MNRAS*, 486, 4781
- . 2020, *MNRAS*, 493, 3920
- Fuller, J., & Ma, L. 2019, *ApJL*, 881, L1
- Fuller, J., Piro, A. L., & Jermyn, A. S. 2019, *MNRAS*, 485, 3661
- Galaudage, S., Adamcewicz, C., Zhu, X.-J., & Thrane, E. 2020, *arxiv/2011.01495*
- Galaudage, S., Talbot, C., & Thrane, E. 2019, *arxiv/1912.09708*
- Gayathri, V., Healy, J., Lange, J., et al. 2020, *arxiv/2009.05461*
- Gerosa, D., & Berti, E. 2017, *PhRvD*, 95, 124046
- Gerosa, D., Berti, E., O’Shaughnessy, R., et al. 2018, *PhRvD*, 98, 084036
- Giacobbo, N., Mapelli, M., & Spera, M. 2017, *MNRAS*, 474, 2959

- Gröbner, M., Ishibashi, W., Tiwari, S., Haney, M., & Jetzer, P. 2020, *A&A*, 638, A119
- Gültekin, K., Miller, M. C., & Hamilton, D. P. 2004, *ApJ*, 616, 221
- Hanna, C., et al. 2020, *PhRvD*, 101, 022003
- Hannam, M., et al. 2014, *PhRvL*, 113, 151101
- Hannuksela, O. A., Haris, K., Ng, K. K. Y., et al. 2019, *ApJ*, 874, L2
- Harry, I., Privitera, S., Bohé, A., & Buonanno, A. 2016, *Physical Review D*, 94, doi:10.1103/physrevd.94.024012
- Heger, A., Fryer, C. L., Woosley, S. E., Langer, N., & Hartmann, D. H. 2003, *ApJ*, 591, 288
- Heger, A., & Woosley, S. E. 2002, *ApJ*, 567, 532
- Huang, Y., Haster, C.-J., Vitale, S., et al. 2020, arXiv e-prints, arXiv:2003.04513
- Husa, S., et al. 2016, *PhRvD*, 93, 044006
- Inayoshi, K., Hirai, R., Kinugawa, T., & Hotokezaka, K. 2017, *Mon. Not. Roy. Astron. Soc.*, 468, 5020
- Jeffreys, H. 1961, *Theory of Probability*, 3rd edn. (Oxford University Press)
- Kalogera, V. 2000, *apj*, 541, 319
- Khan, S., Ohme, F., Chatziioannou, K., & Hannam, M. 2020, *PhRvD*, 101, 024056
- Khan, S., et al. 2016, *PhRvD*, 93, 044007
- Kidder, L. E. 1995, *Phys. Rev. D*, 52, 821
- Kimball, C., Talbot, C., Berry, C. P., et al. 2020a, *ApJ*, 900, 177
- . 2020b, arxiv/2011.05332
- Kimpson, T. O., Spera, M., Mapelli, M., & Ziosi, B. M. 2016, *MNRAS*, 463, 2443
- Klimenko, S., & Mitselmakher, G. 2004, *Class. Quant. Grav.*, 21, S1819
- Klimenko, S., et al. 2016, *PhRvD*, 93, 042004
- Kopparapu, R. K., Hanna, C., Kalogera, V., et al. 2008, *apj*, 675, 1459
- Kovetz, E. D., Cholis, I., Breyse, P. C., & Kamionkowski, M. 2017, *PhRvD*, 95, 103010
- Kreidberg, L., Bailyn, C. D., Farr, W. M., & Kalogera, V. 2012, *ApJ*, 757, 36
- Kulkarni, S. R., Hut, P., & McMillan, S. 1993, *Nature*, 364, 421
- Kushnir, D., Zaldarriaga, M., Kollmeier, J. A., & Waldman, R. 2016, *MNRAS*, 462, 844
- Lange, J., O’Shaughnessy, R., & Rizzo, M. 2018, arxiv/1805.10457
- Li, S.-S., Mao, S., Zhao, Y., & Lu, Y. 2018, *MNRAS*, 476, 2220
- LIGO Scientific Collaboration. 2018, *LIGO Algorithm Library - LALSuite*, Free Software (GPL), doi:10.7935/GT1W-FZ16
- LIGO-Virgo. 2020, *GWTC-2 Data Release: Sensitivity of Matched Filter Searches to Binary Black Hole Merger Populations*, doi:https://dcc.ligo.org/LIGO-P2000217/public
- Liu, B., & Bromm, V. 2020, arXiv e-prints, arXiv:2009.11447
- Liu, B., Lai, D., & Wang, Y.-H. 2019, *ApJ*, 881, 41
- Loredo, T. J. 2004, in *American Institute of Physics Conference Series*, Vol. 735, 195–206
- Lower, M. E., Thrane, E., Lasky, P. D., & Smith, R. J. E. 2018, *PhRvD*, 98, 083028
- Madau, P., & Dickinson, M. 2014, *Annual Review of Astronomy and Astrophysics*, 52, 415
- Madau, P., & Rees, M. J. 2001, *ApJL*, 551, L27
- Magee, R., et al. 2019, *ApJ*, 878, L17
- Mandel, I., & de Mink, S. E. 2016, *MNRAS*, 458, 2634
- Mandel, I., Farr, W. M., & Gair, J. R. 2019, *MNRAS*, 486, 1086
- Mandel, I., Müller, B., Riley, J., et al. 2021, *MNRAS*, 500, 1380
- Mandel, I., & O’Shaughnessy, R. 2010, *CQGra*, 27, 114007
- Mapelli, M. 2016, *MNRAS*, 459, 3432
- Mapelli, M., Giacobbo, N., Ripamonti, E., & Spera, M. 2017, *MNRAS*, 472, 2422
- Mapelli, M., Spera, M., Montanari, E., et al. 2020, *ApJ*, 888, 76
- Marchant, P., Langer, N., Podsiadlowski, P., Tauris, T. M., & Moriya, T. J. 2016, *A&A*, 588, A50
- Marchant, P., & Moriya, T. 2020, arXiv:2007.06220
- McKernan, B., Ford, K. E. S., Lyra, W., & Perets, H. B. 2012, *MNRAS*, 425, 460
- McKernan, B., Ford, K. E. S., O’Shaughnessy, R., & Wysocki, D. 2020, *MNRAS*, 494, 1203
- McKernan, B., Saavik Ford, K. E., Bellovary, J., et al. 2018, *ApJ*, 866, 66
- Messick, C., et al. 2017, *PhRvD*, 95, 042001
- Miller, C. M., & Hamilton, D. P. 2002a, *ApJ*, 576, 894
- Miller, M. C., & Hamilton, D. P. 2002b, *MNRAS*, 330, 232
- Miller, M. C., & Lauburg, V. M. 2009, *ApJ*, 692, 917
- Miller, S., Callister, T. A., & Farr, W. 2020, *ApJ*, 895, 128
- Moody, K., & Sigurdsson, S. 2009, *ApJ*, 690, 1370
- Most, E. R., Papenfort, L. J., Weih, L. R., & Rezzolla, L. 2020, arXiv:2006.14601
- Natarajan, P. 2020, arXiv e-prints, arXiv:2009.09156
- Neijssel, C. J., Vigna-Gómez, A., Stevenson, S., et al. 2019, *MNRAS*, 490, 3740
- Ng, K. K., Vitale, S., Zimmerman, A., et al. 2018a, *PhRvD*, 98, 083007
- Ng, K. K. Y., Wong, K. W. K., Broadhurst, T., & Li, T. G. F. 2018b, *PhRvD*, 97, 023012

- Nitz, A., et al. 2019a, "gwastro/pycbc: Pycbc release v1.15.0"
- Nitz, A. H., Capano, C., Nielsen, A. B., et al. 2019b, *ApJ*, 872, 195
- Nitz, A. H., & Capano, C. D. 2020, *arXiv/2010.12558*
- Nitz, A. H., Dent, T., Canton, T. D., Fairhurst, S., & Brown, D. A. 2017, *ApJ*, 849, 118
- Nitz, A. H., Dent, T., Davies, G. S., et al. 2020, *ApJ*, 891, 123
- Oguri, M. 2018, *MNRAS*, 3842
- O’Leary, R. M., Kocsis, B., & Loeb, A. 2009, *MNRAS*, 395, 2127
- O’Leary, R. M., Rasio, F. A., Fregeau, J. M., Ivanova, N., & O’Shaughnessy, R. 2006, *ApJ*, 637, 937
- Olejak, A., Fishbach, M., Belczynski, K., et al. 2020, *arXiv e-prints*, *arXiv:2004.11866*
- O’Shaughnessy, R., Gerosa, D., & Wysocki, D. 2017, *PhRvL*, 119, 011101
- Ossokine, S., et al. 2020, *arXiv:2004.09442*
- Özel, F., Psaltis, D., Narayan, R., & McClintock, J. E. 2011, *ApJ*, 725, 1918
- Pan, Y., Buonanno, A., Taracchini, A., et al. 2014, *Phys. Rev. D*, 89, 084006
- Park, D., Kim, C., Lee, H. M., Bae, Y.-B., & Belczynski, K. 2017, *MNRAS*, 469, 4665
- Portegies Zwart, S. F., & McMillan, S. L. W. 2000, *ApJL*, 528, L17
- Portegies Zwart, S. F., & Yungelson, L. R. 1998, *A&A*, 332, 173
- Pratten, G., & Vecchio, A. 2020, *arXiv:2008.00509*
- Pretorius, F. 2005, *PhRvL*, 95, 121101
- Qin, Y., Fragos, T., Meynet, G., et al. 2018, *A&A*, 616, A28
- Rice, J. R., & Zhang, B. 2020, *arXiv e-prints*, *arXiv:2009.11326*
- Riddell, A., Hartikainen, A., Lee, D., Riddell-Stan, et al. 2018, *Stan-Dev/PyStan: V2.18.0.0*, *doi:10.5281/ZENODO.1456206*
- Rodriguez, C. L., Amaro-Seoane, P., Chatterjee, S., & Rasio, F. A. 2018, *PhRvL*, 120, 151101
- Rodriguez, C. L., & Antonini, F. 2018, *ApJ*, 863, 7
- Rodriguez, C. L., & Loeb, A. 2018, *ApJ*, 866, L5
- Rodriguez, C. L., Morscher, M., Pattabiraman, B., et al. 2015, *PhRvL*, 115, 051101
- Rodriguez, C. L., Zevin, M., Amaro-Seoane, P., et al. 2019, *PhRvD*, 100, 043027
- Rodriguez, C. L., Zevin, M., Pankow, C., Kalogera, V., & Rasio, F. A. 2016, *ApJL*, 832, L2
- Romero-Shaw, I. M., Lasky, P. D., & Thrane, E. 2019, *MNRAS*, 490, 5210
- Romero-Shaw, I. M., Lasky, P. D., Thrane, E., & Bustillo, J. C. 2020a, *ApJL*, 903, L5
- Romero-Shaw, I. M., et al. 2020b, *arXiv/2006.00714*
- Roulet, J., Venumadhav, T., Zackay, B., Dai, L., & Zaldarriaga, M. 2020, *arXiv e-prints*, *arXiv:2008.07014*
- Roulet, J., & Zaldarriaga, M. 2019, *MNRAS*, 484, 4216
- Roupas, Z., & Kazanas, D. 2019, *A&A*, 632, L8
- Sachdev, S., et al. 2019, *arXiv:1901.08580*
- Safarzadeh, M. 2020, *Nature Astronomy*, 4, 735
- Safarzadeh, M., Farr, W. M., & Ramirez-Ruiz, E. 2020, *ApJ*, 894, 129
- Safarzadeh, M., & Haiman, Z. 2020, *arXiv e-prints*, *arXiv:2009.09320*
- Samsing, J. 2018, *PhRvD*, 97, 103014
- Samsing, J., MacLeod, M., & Ramirez-Ruiz, E. 2014, *ApJ*, 784, 71
- Samsing, J., & Ramirez-Ruiz, E. 2017, *ApJL*, 840, L14
- Santoliquido, F., Mapelli, M., Bouffanais, Y., et al. 2020, *arXiv e-prints*, *arXiv:2004.09533*
- Schmidt, P., Hannam, M., & Husa, S. 2012, *PhRvD*, 86, 104063
- Schmidt, P., Ohme, F., & Hannam, M. 2015, *PhRvD*, 91, 024043
- Sigurdsson, S., & Hernquist, L. 1993, *Nature*, 364, 423
- Smith, G. P., Jauzac, M., Veitch, J., et al. 2018, *MNRAS*, 475, 3823
- Speagle, J. S. 2020, *MNRAS*, 493, 3132
- Spera, M., & Mapelli, M. 2017, *MNRAS*, 470, 4739
- Stevenson, S., Berry, C. P. L., & Mandel, I. 2017, *MNRAS*, 471, 2801
- Stone, N. C., Metzger, B. D., & Haiman, Z. 2017, *MNRAS*, 464, 946
- Sun, L., Goetz, E., Kissel, J. S., et al. 2020, *Classical and Quantum Gravity*, 37, 225008
- Tagawa, H., Haiman, Z., & Kocsis, B. 2020, *The Astrophysical Journal*, 898, 25
- Talbot, C., Smith, R., Thrane, E., & Poole, G. B. 2019, *PhRvD*, 100, 043030
- Talbot, C., & Thrane, E. 2017, *PhRvD*, 96, 023012
- . 2018, *ApJ*, 856, 173
- Tan, H., Noronha-Hostler, J., & Yunes, N. 2020, *arXiv:2006.16296*
- Tanikawa, A., Susa, H., Yoshida, T., Trani, A. A., & Kinugawa, T. 2020, *arXiv e-prints*, *arXiv:2008.01890*
- Taracchini, A., et al. 2014, *Phys. Rev. D*, 89, 061502
- Tews, I., Pang, P. T., Dietrich, T., et al. 2020, *arXiv:2007.06057*
- Thompson, T. A., et al. 2019, *Science*, 366
- Thrane, E., & Talbot, C. 2019, *PASA*, 36, E010
- Tiwari, V. 2018, *Classical and Quantum Gravity*, 35, 145009

- . 2020, arXiv e-prints, arXiv:2006.15047
- Tiwari, V., Fairhurst, S., & Hannam, M. 2018, *ApJ*, 868, 140
- Trovato, A., et al. 2020, *PoS, Asterics2019*, 082
- Usman, S. A., et al. 2016, *CQGra*, 33, 215004
- van Son, L. A. C., de Mink, S. E., Broekgaarden, F. S., et al. 2020, arXiv e-prints, arXiv:2004.05187
- Varma, V., Field, S. E., Scheel, M. A., et al. 2019, *Phys. Rev. Research*, 1, 033015
- Veitch, J., Raymond, V., Farr, B., et al. 2015, *PhRvD*, 91, 042003
- Venumadhav, T., Zackay, B., Roulet, J., Dai, L., & Zaldarriaga, M. 2019, *PhRvD*, 100, 023011
- . 2020, *PhRvD*, 101, 083030
- Vigna-Gómez, A., Toonen, S., Ramirez-Ruiz, E., et al. 2020, arXiv e-prints, arXiv:2010.13669
- Vitale, S. 2020, arXiv:2007.05579
- Vitale, S., Gerosa, D., Haster, C.-J., Chatziioannou, K., & Zimmerman, A. 2017a, *PhRvL*, 119, 251103
- Vitale, S., Lynch, R., Sturani, R., & Graff, P. 2017b, *Class. Quant. Grav.*, 34, 03LT01
- Woosley, S. E. 2017, *ApJ*, 836, 244
- Woosley, S. E., & Heger, A. 2015, in *Very Massive Stars Local Universe* (Springer, Cham), 199–225
- Woosley, S. E., Heger, A., & Weaver, T. A. 2002, *Rev. of Mod. Phys.*, 74, 1015
- Wysocki, D. 2020
- Wysocki, D., Lange, J., & O’Shaughnessy, R. 2019a, *PhRvD*, 100, 043012
- Wysocki, D., & O’Shaughnessy, R. 2017, *Bayesian Parametric Population Models*, bayesian-parametric-population-models.readthedocs.io
- Wysocki, D., O’Shaughnessy, R., Lange, J., & Fang, Y.-L. L. 2019b, *PhRvD*, 99
- Wysocki, D., et al. 2018, *PhRvD*, 97, 043014
- Yang, Y., Bartos, I., Gayathri, V., et al. 2019, *PhRvL*, 123, 181101
- Zackay, B., Dai, L., Venumadhav, T., Roulet, J., & Zaldarriaga, M. 2020, *PhRvD*, 101, 083030
- Zackay, B., Venumadhav, T., Dai, L., Roulet, J., & Zaldarriaga, M. 2019, *PhRvD*, 100, 023007
- Zaldarriaga, M., Kushnir, D., & Kollmeier, J. A. 2018, *MNRAS*, 473, 4174
- Zevin, M., Pankow, C., Rodriguez, C. L., et al. 2017, *ApJ*, 846, 82
- Zevin, M., Samsing, J., Rodriguez, C., Haster, C.-J., & Ramirez-Ruiz, E. 2019, *ApJ*, 871, 91
- Zevin, M., Spera, M., Berry, C. P., & Kalogera, V. 2020, arXiv:2006.14573
- Zhang, N.-B., & Li, B.-A. 2020, arXiv:2007.02513
- Ziegler, J., & Freese, K. 2020, arXiv e-prints, arXiv:2010.00254
- Ziosi, B. M., Mapelli, M., Branchesi, M., & Tormen, G. 2014, *MNRAS*, 441, 3703

APPENDIX

A. ESTIMATING THE DETECTION FRACTION

A key ingredient in Eqs. (1) and (2) is the detection fraction $\xi(\Lambda)$, the fraction of systems within some prior volume (redshift $z < 2.3$) that we expect to successfully detect. The detection fraction quantifies selection biases, and so it is critical to accurately characterize. For a population described by hyper-parameters Λ , the detection fraction is

$$\xi(\Lambda) = \int P_{\text{det}}(\theta) \pi(\theta|\Lambda) d\theta. \quad (\text{A1})$$

Here, $P_{\text{det}}(\theta)$ is the detection probability: the probability that an event with parameters θ is detectable. The detection probability depends primarily on the masses and redshift of a system, and, to a lesser degree, on the spins.

We calculate $\xi(\Lambda)$ using injections. We simulate compact binary signals from a reference population and record which ones are successfully detected by the PyCBC and GstLAL search pipelines; see Abbott et al. (2020c). Following Tiwari (2018); Farr (2019); Vitale (2020); Loredó (2004), the point estimate for Eq. A1 is calculated using a Monte Carlo integral over found injections:

$$\hat{\xi}(\Lambda) = \frac{1}{N_{\text{inj}}} \sum_{j=1}^{N_{\text{found}}} \frac{\pi(\theta_j | \Lambda)}{p_{\text{draw}}(\theta_j)}, \quad (\text{A2})$$

where N_{inj} is the total number of injections, N_{found} are the injections that are successfully detected, and p_{draw} is the probability distribution from which the injections are drawn; see LIGO-Virgo (2020) for additional details. When sampling the population likelihood, we marginalize over the uncertainty in $\hat{\xi}(\Lambda)$ following Farr (2019), and ensure that the effective number of found injections remaining after population re-weighting is sufficiently high ($N_{\text{eff}} > 4N_{\text{det}}$).

For the O3a observing period, we use the injection campaign described in Abbott et al. (2020c) and characterize the found injections as those recovered with a FAR below our threshold of 1 yr^{-1} in either PyCBC or GstLAL. For the O1 and O2 observing period, we supplement the O3a pipeline injections with mock injections drawn from the same distribution p_{draw} above. For the mock injections, we calculate $P_{\text{det}}(m_1, m_2, z, \chi_{1,z}, \chi_{2,z})$ according to the semi-analytic approximation described in Abbott et al. (2019a), based on a single-detector signal-to-noise ratio threshold $\rho = 8$ and the ADVANCED LIGO EARLY-HIGH NOISE PSD (Abbott et al. 2013). We combine O1, O2 and O3 injection sets ensuring a constant rate of injections across the total observing time, yielding $N_{\text{inj}} \approx 7.7 \times 10^7$ injections for O3a and $N_{\text{inj}} \approx 7.1 \times 10^7$ for O1 and O2. To control computational costs, not all of the injections are performed in real data. Before injecting, the expected network signal-to-noise ratio of the injections is computed, and the hopeless injections with signal-to-noise ratio < 6 are removed.

Due to the finite number of injections, we approximate Eq. (A1) with a fixed spin distribution instead of the distribution implied by Λ . When combining the TRUNCATED, POWER LAW + PEAK, BROKEN POWER LAW and MULTI PEAK mass models together with the DEFAULT spin distribution, we assume that the aligned spin components $\chi_{1,z}, \chi_{2,z}$ are independently drawn from a uniform distribution $U(-0.5, 0.5)$. By making this approximation, we are in effect ignoring selection effects due to spin. Nevertheless, we expect this approximation to have a negligible impact on the inferred spin distribution compared to the statistical uncertainties. For aligned spin components in the range $(-0.5, 0.5)$, the detection probability varies by no more than a factor of 2 (Ng et al. 2018a). Furthermore, our main conclusions regarding the spin distribution inferred from the DEFAULT model are supported by the GAUSSIAN model, which requires no approximations for spin selection effects. The MULTI SPIN model calculates Eq. (A1) by calibrating a semi-analytic approximation to the list of found injections (Wysocki 2020).

The transfer function between the observed strain and astrophysical strain is subject to a systematic calibration uncertainty. We neglect this calibration uncertainty in our estimates of the search sensitivity above. For the O3a observing run, the amplitude uncertainty was $\lesssim 3\%$ (Sun et al. 2020), which leads to a $\lesssim 10\%$ systematic uncertainty in the sensitive spacetime volume and the inferred merger rate. This systematic uncertainty is subdominant to our uncertainties from Poisson counting error.

B. DETAILS OF MASS POPULATION MODELS

In this section we provide details about the population models described above in Section 3; see also Fig. 1. Each subsection includes a table with a summary of the parameters for that model and the prior distribution used for each parameter. The prior distributions are indicated using abbreviations: for example, $U(0, 1)$ translates to uniform on the interval $(0, 1)$ and $\text{LU}(10^{-6}, 10^5)$ translates to log-uniform on the interval $10^{-6}, 10^5$.

Parameter	Description	Prior
α	Spectral index for the power-law of the primary mass distribution.	$U(-4, 12)$
β_q	Spectral index for the power-law of the mass ratio distribution.	$U(-4, 12)$
m_{\min}	Minimum mass of the power-law component of the primary mass distribution.	$U(2 M_{\odot}, 10 M_{\odot})$
m_{\max}	Maximum mass of the power-law component of the primary mass distribution.	$U(30 M_{\odot}, 100 M_{\odot})$

Table 5. Summary of TRUNCATED parameters.

B.1. TRUNCATED mass model

This model is equivalent to “Model B” in [Abbott et al. \(2019a\)](#). The primary mass distribution for this model follows a power-law with spectral index α , and with a sharp cut-off at the lower end m_{\min} and the upper end of the distribution m_{\max} :

$$\pi(m_1 | \alpha, m_{\min}, m_{\max}) \propto \begin{cases} m_1^{-\alpha} & m_{\min} < m_1 < m_{\max} \\ 0 & \text{otherwise,} \end{cases} \quad (\text{B3})$$

Meanwhile, the mass ratio $q \equiv m_2/m_1$ follows a power-law distribution with spectral index β_q

$$\pi(q | \beta_q, m_{\min}, m_1) \propto \begin{cases} q^{\beta_q} & m_{\min} < m_2 < m_1 \\ 0 & \text{otherwise.} \end{cases} \quad (\text{B4})$$

The hyper-parameters for this model are summarized in Table 5.

B.2. POWER LAW + PEAK mass model

This is equivalent to “Model C” from [Abbott et al. \(2019a\)](#). It is motivated by the idea that the mass loss undergone by pulsational pair-instability supernovae could lead to a pile-up of BBH events before the pair-instability gap ([Talbot & Thrane 2018](#)). The primary mass distribution is an extension of TRUNCATED with the addition of tapering at the lower mass end of the distribution and a Gaussian component:

$$\pi(m_1 | \lambda_{\text{peak}}, \alpha, m_{\min}, \delta_m, m_{\max}, \mu_m, \sigma_m) = \left[(1 - \lambda_{\text{peak}}) \mathfrak{P}(m_1 | -\alpha, m_{\max}) + \lambda_{\text{peak}} G(m_1 | \mu_m, \sigma_m) \right] S(m_1 | m_{\min}, \delta_m). \quad (\text{B5})$$

Here, $\mathfrak{P}(m_1 | -\alpha, m_{\max})$ is a normalized power-law distribution with spectral index $-\alpha$ and high-mass cut-off m_{\max} . Meanwhile, $G(m_1 | \mu_m, \sigma_m)$ is a normalized Gaussian distribution with mean μ_m and width σ_m . The parameter λ_{peak} is a mixing fraction determining the relative prevalence of mergers in \mathfrak{P} and G . Finally, $S(m_1, m_{\min}, \delta_m)$ is a smoothing function, which rises from 0 to 1 over the interval $(m_{\min}, m_{\min} + \delta_m)$:

$$S(m | m_{\min}, \delta_m) = \begin{cases} 0 & (m < m_{\min}) \\ [f(m - m_{\min}, \delta_m) + 1]^{-1} & (m_{\min} \leq m < m_{\min} + \delta_m) \\ 1 & (m \geq m_{\min} + \delta_m) \end{cases} \quad (\text{B6})$$

with

$$f(m', \delta_m) = \exp \left(\frac{\delta_m}{m'} + \frac{\delta_m}{m' - \delta_m} \right). \quad (\text{B7})$$

The conditional mass ratio distribution in this model also includes the smoothing term:

$$\pi(q | \beta, m_1, m_{\min}, \delta_m) \propto q^{\beta_q} S(qm_1 | m_{\min}, \delta_m). \quad (\text{B8})$$

The hyper-parameters for this model are summarized in Table 6.

In Fig. 16, we provide a corner plot representation of the posterior distribution for the POWER LAW + PEAK hyper-parameters. The $(\mu_m, \lambda_{\text{peak}})$ panel describes the Gaussian component: μ_m is the center of the Gaussian while

Parameter	Description	Prior
α	Spectral index for the power-law of the primary mass distribution.	$U(-4, 12)$
β_q	Spectral index for the power-law of the mass ratio distribution.	$U(-4, 12)$
m_{\min}	Minimum mass of the power-law component of the primary mass distribution.	$U(2 M_{\odot}, 10 M_{\odot})$
m_{\max}	Maximum mass of the power-law component of the primary mass distribution.	$U(30 M_{\odot}, 100 M_{\odot})$
λ_{peak}	Fraction of BBH systems in the Gaussian component.	$U(0, 1)$
μ_m	Mean of the Gaussian component in the primary mass distribution.	$U(20 M_{\odot}, 50 M_{\odot})$
σ_m	Width of the Gaussian component in the primary mass distribution.	$U(1 M_{\odot}, 10 M_{\odot})$
δ_m	Range of mass tapering at the lower end of the mass distribution.	$U(0 M_{\odot}, 10 M_{\odot})$

Table 6. The parameters that describe the BBH mass distribution for Model POWER LAW + PEAK.

λ_{peak} is the fraction of mergers taking place in the Gaussian (as opposed to the power-law distribution). Judging from this panel, it appears at first that λ_{peak} peaks close to 0 (corresponding to no Gaussian peak). However, if we zoom in as in Fig. 6, we see that the posterior for λ_{peak} is peaked clearly away from zero at ~ 0.02 . This is consistent with the large Bayes factor indicating preference for POWER LAW + PEAK over TRUNCATED.

B.3. BROKEN POWER LAW *mass model*

This model is an extension of TRUNCATED. The primary mass distribution consists of a broken power-law. This is motivated by the potential tapering of the primary mass distribution at high masses. Also, the model employs a smoothing function to prevent a sharp cut-off at low masses.

$$\pi(m_1 | \alpha_1, \alpha_2, m_{\min}, m_{\max}) \propto \begin{cases} m_1^{-\alpha_1} S(m_1 | m_{\min}, \delta_m) & m_{\min} < m_1 < m_{\text{break}} \\ m_1^{-\alpha_2} S(m_1 | m_{\min}, \delta_m) & m_{\text{break}} < m_1 < m_{\max} \\ 0 & \text{otherwise.} \end{cases} \quad (\text{B9})$$

Here,

$$m_{\text{break}} = m_{\min} + b(m_{\max} - m_{\min}), \quad (\text{B10})$$

is the mass where there is a break in the spectral index and b is the fraction of the way between m_{\min} and m_{\max} at which the primary mass distribution undergoes a break. Meanwhile, $S(m_1, m_{\min}, \delta_m)$ is a smoothing function as in Eq. (B6). The conditional mass ratio distribution is the same as in the POWER LAW + PEAK model; see Eq. B8. The hyper-parameters for this model are summarized in Table 7. In Fig. 17 we provide a corner plot for BROKEN POWER LAW. In the limit of no low-mass smoothing ($\delta_m = 0$), and in the limit of a second power-law with a steep slope that mimics a sharp cutoff ($m_{\text{break}} = m_{\max}$), this model reduces to TRUNCATED. Above, we noted that the BROKEN POWER LAW model prefers a break in the primary mass spectrum near $40 M_{\odot}$. On the other hand, if we believe that the feature represented by m_{break} should be closer to a sharp cutoff, then the cut-off must occur at higher masses approaching the maximum mass of TRUNCATED at $m_{\max} = 74.6^{+15.4}_{-8.6} M_{\odot}$. This can be seen by the correlation between b and α_2 in Fig. 17.

B.4. MULTI PEAK *mass model*

This model is an extension of POWER LAW + PEAK, where there is an additional Gaussian component at the upper end of the mass distribution motivated by a possible subpopulation of objects in the upper mass gap:

$$\pi(m_1 | \lambda, \alpha, m_{\min}, \delta_m, m_{\max}, \mu_m, \sigma_m) = \left[(1 - \lambda) \mathfrak{P}(m_1 | -\alpha, m_{\max}) + \lambda \lambda_1 G(m_1 | \mu_{m,1}, \sigma_{m,1}) + \lambda(1 - \lambda_1) G(m_1 | \mu_{m,2}, \sigma_{m,2}) \right] S(m_1 | m_{\min}, \delta_m). \quad (\text{B11})$$

Here, the parameters λ and λ_1 correspond to the fraction of binaries in any Gaussian component and the fraction of binaries in the lower-mass Gaussian of the Gaussian components, respectively. The distribution $G(m_1 | \mu_{m,1}, \sigma_{m,1})$ is a

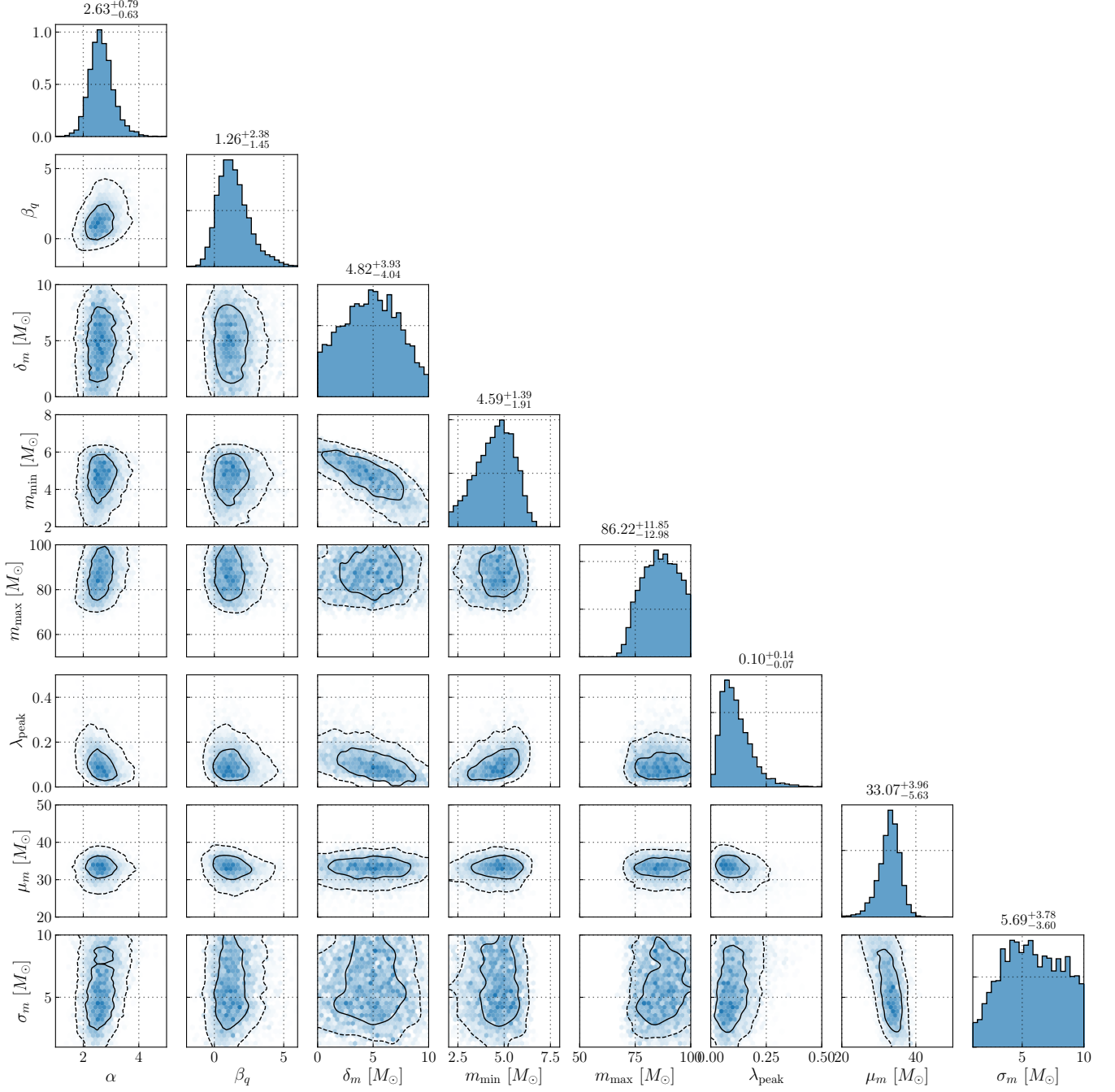


Figure 16. Posterior distribution for mass hyper-parameters for POWER LAW + PEAK. The fit excludes GW190814. The contours represent 50% and 90% credible bounds.

normalized Gaussian distribution for the lower-mass peak with mean $\mu_{m,1}$ and width $\sigma_{m,2}$ and $G(m_1|\mu_{m,2},\sigma_{m,1})$ is a normalized Gaussian distribution for the upper-mass peak with mean $\mu_{m,2}$ and width $\sigma_{m,2}$. The hyper-parameters for this model are summarized in Table 8. In Fig. 18 we provide a corner plot for MULTI PEAK for parameters corresponding to the two Gaussian peaks. The mean of the upper-mass peak $\mu_{m,2} = 68^{+18}_{-14} M_\odot$ is located at approximately twice the mean of the lower-mass peak $\mu_{m,1} = 33.4^{+4.4}_{-4.9} M_\odot$. The remaining parameters are: $\alpha = 2.9^{+1.9}_{-1.4}$, $\beta_q = 0.9^{+1.3}_{-1.3}$, $m_{\min} = 4.6^{+1.3}_{-1.8} M_\odot$ and $m_{\max} = 65^{+31}_{-30} M_\odot$. In Fig. 19, we provide a posterior predictive check for all of the mass models used in this analysis.

Parameter	Description	Prior
α_1	Power-law slope of the primary mass distribution for masses below m_{break} .	$\text{U}(-4, 12)$
α_2	Power-law slope for the primary mass distribution for masses above m_{break} .	$\text{U}(-4, 12)$
β_q	Spectral index for the power-law of the mass ratio distribution.	$\text{U}(-4, 12)$
m_{min}	Minimum mass of the power-law component of the primary mass distribution.	$\text{U}(2 M_{\odot}, 10 M_{\odot})$
m_{max}	Maximum mass of the primary mass distribution.	$\text{U}(30 M_{\odot}, 100 M_{\odot})$
b	The fraction of the way between m_{min} and m_{max} at which the primary mass distribution breaks, e.g. a break fraction of 0.4 between $m_{\text{min}} = 5$ and $m_{\text{max}} = 85$ means the break occurs at $m_1 = 32$.	$\text{U}(0, 1)$
δ_m	Range of mass tapering on the lower end of the mass distribution.	$\text{U}(0 M_{\odot}, 10 M_{\odot})$

Table 7. Summary of BROKEN POWER LAW parameters.

Parameter	Description	Prior
α	Spectral index for the power-law of the primary mass distribution.	$\text{U}(-4, 12)$
β_q	Spectral index for the power-law of the mass ratio distribution.	$\text{U}(-4, 12)$
m_{min}	Minimum mass of the power-law component of the primary mass distribution.	$\text{U}(2 M_{\odot}, 10 M_{\odot})$
m_{max}	Maximum mass of the power-law component of the primary mass distribution.	$\text{U}(30 M_{\odot}, 100 M_{\odot})$
λ	Fraction of BBH systems in the Gaussian components.	$\text{U}(0, 1)$
λ_1	Fraction of BBH systems in the Gaussian components belonging to the lower-mass component.	$\text{U}(0, 1)$
$\mu_{m,1}$	Mean of the lower-mass Gaussian component in the primary mass distribution.	$\text{U}(20 M_{\odot}, 50 M_{\odot})$
$\sigma_{m,1}$	Width of the lower-mass Gaussian component in the primary mass distribution.	$\text{U}(1 M_{\odot}, 10 M_{\odot})$
$\mu_{m,2}$	Mean of the upper-mass Gaussian component in the primary mass distribution.	$\text{U}(50 M_{\odot}, 100 M_{\odot})$
$\sigma_{m,2}$	Width of the upper-mass Gaussian component in the primary mass distribution.	$\text{U}(1 M_{\odot}, 10 M_{\odot})$
δ_m	Range of mass tapering on the lower end of the mass distribution.	$\text{U}(0 M_{\odot}, 10 M_{\odot})$

Table 8. Parameters for the BBH mass distribution for Model MULTI PEAK.

C. MASS MODEL CHECKING

Section 5.1 describes the inferred mass distribution obtained with the TRUNCATED, BROKEN POWER LAW, POWER LAW + PEAK, and MULTI PEAK models, and compares the different models by calculating their Bayes factors. Here we assess the goodness-of-fit of the models using posterior predictive checks, comparing predicted and empirical catalogs of observed m_1 distributions in Fig. 19. The light colored bands show the cumulative distribution of m_1 as predicted by the model, while the darker bands show the empirical distribution based on the actual events observed in GWTC-2. The bands represent a family of curves, where each curve corresponds to a different draw from the population hyper-posterior. Each draw from the hyper-posterior updates both the predicted distribution (in the lighter color) and the empirical distribution (in the darker color), as the individual event posteriors are updated according to the inferred population distribution (Fishbach et al. 2020b; Galaudage et al. 2019; Miller et al. 2020). If the model is a good fit to the data, the dark colored bands should overlap with the light colored bands. Figure 19 shows the relatively poor fit for the TRUNCATED model, which cannot capture the excess of events at $\sim 30\text{--}40 M_{\odot}$ compared to $\gtrsim 40 M_{\odot}$. The remaining panels show the improved fits with the POWER LAW + PEAK, BROKEN POWER LAW and MULTI PEAK models. These results are consistent with the Bayes factors in Table 2, which conclude that the TRUNCATED model is disfavored by a Bayes factor of 10–80 relative to the other models.

C.1. On GW190412

Other than GW190814, we find that GW190412 (Abbott et al. 2020a), when analyzed with a population informed prior, remains the only system for which we can confidently bound the mass ratio away from unity, yielding $q < 0.53$ at 99% credibility (using the POWER LAW + PEAK mass model). All other events, when analyzed with a population-informed prior, are consistent with $q = 1$ at 99% credibility. Repeating the analysis in Abbott et al. (2020a), we perform a leave-one-out analysis without GW190412 and find $\beta_q = 4.0^{+6.4}_{-3.2}$ ($\beta_q = 4.5^{+5.9}_{-3.5}$) for the POWER LAW + PEAK (BROKEN POWER LAW) model. The β_q posterior inferred with the inclusion of GW190412 ($\beta_q = 1.3^{+2.4}_{-1.5}$ for the POWER LAW +

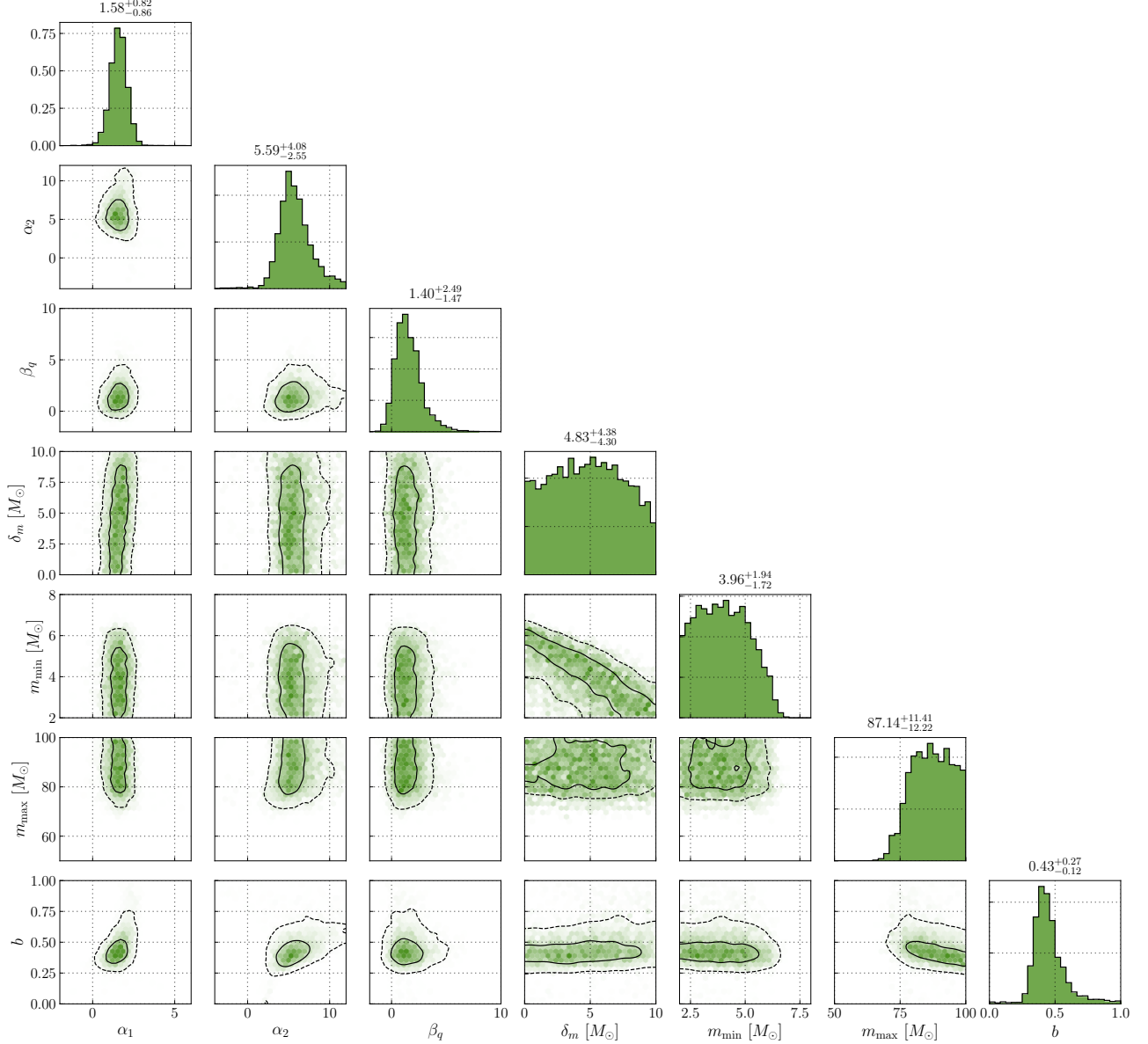


Figure 17. Posterior distribution for mass hyper-parameters for BROKEN POWER LAW. The fit excludes GW190814. The contours represent 50%, 90% credible bounds.

PEAK model; $\beta_q = 1.4^{+2.5}_{-1.5}$ for the BROKEN POWER LAW model) has moderate ($\sim 50\%$) overlap with the leave-one-out β_q posterior, indicating that, consistent with the conclusion in [Abbott et al. \(2020a\)](#), GW190412 likely belongs to the low mass ratio tail of the distribution rather than a distinct subpopulation of asymmetric systems.

C.2. On GW190521

As discussed in Section 5.1, the most massive event, GW190521 ([Abbott et al. 2020e](#)), is an outlier with respect to the TRUNCATED model (see Fig. 2), but fits well within the mass distributions inferred from the other models. In Fig. 20, we show the effect of GW190521 on the primary mass distribution. This event shifts the best-fit mass distribution, but this shift is within the statistical uncertainties. Thus, we find no evidence that GW190521 is an outlier within the framework of the POWER LAW + PEAK and BROKEN POWER LAW mass models. This finding is supported by the posterior predictive check in subsection C.4. In Fig. 21, we show how the primary mass posterior distribution for GW190521 changes when we use the POWER LAW + PEAK model to inform our prior. While the population-informed posterior on the primary mass prefers smaller masses ([Fishbach et al. 2020b](#)), the conclusion that the primary mass of

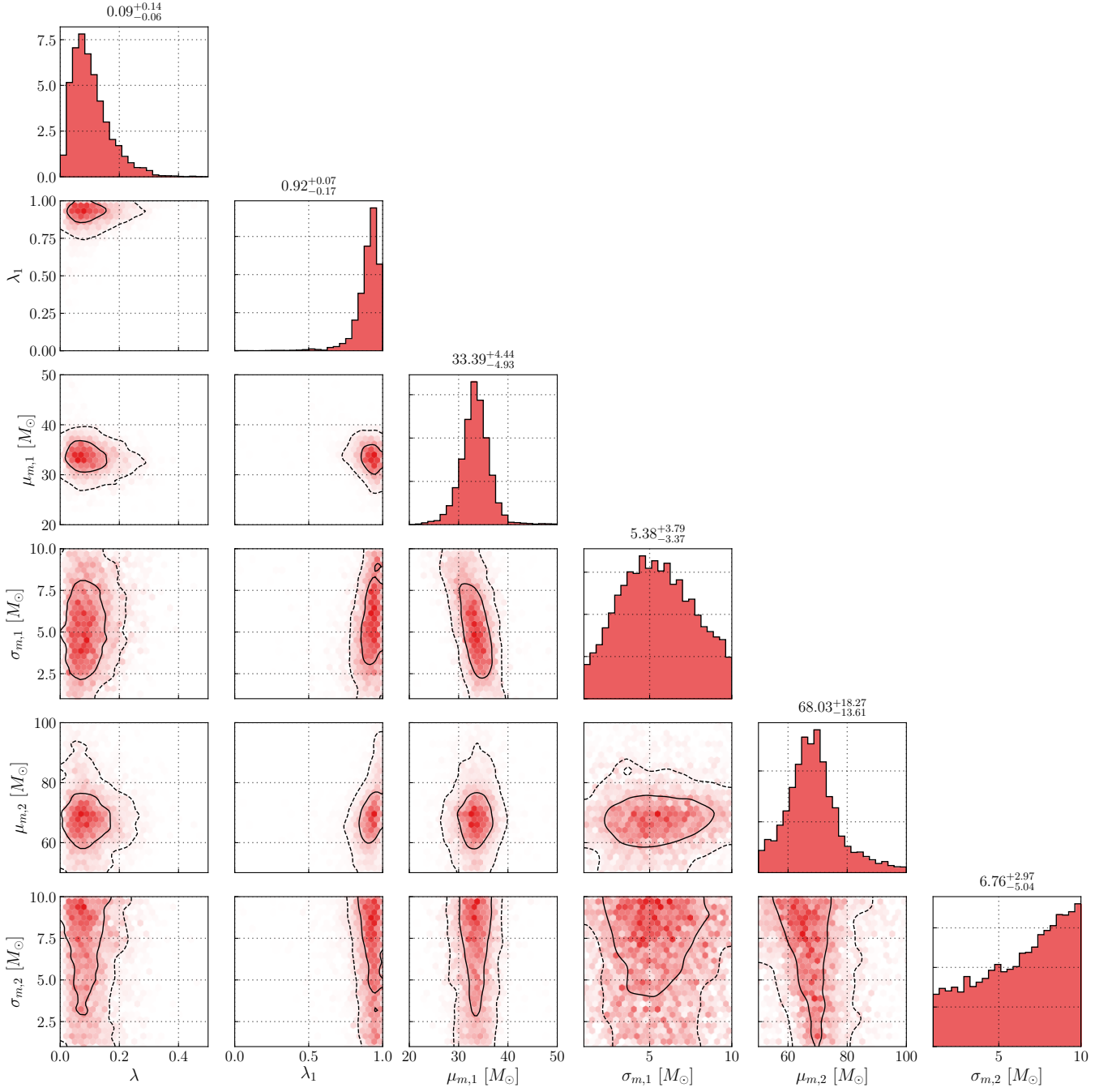


Figure 18. Posterior distribution for mass hyper-parameters for MULTI PEAK. The fit excludes GW190814. The contours represent 50% and 90% credible bounds.

GW190521 is above $67 M_{\odot}$ (99% credibility) is robust to the choice of prior, consistent with the claims in [Abbott et al. \(2020e\)](#).

C.3. On GW190814

On the other hand, we see clear indication that GW190814 is an outlier with respect to the BBH population within the framework of the POWER LAW + PEAK and BROKEN POWER LAW mass models, as discussed in Section 5.1. As an additional posterior predictive check, following the analysis described in [Fishbach et al. \(2020b\)](#) and [Abbott et al. \(2020a\)](#), we use the posterior predictive distribution, inferred without GW190814, to construct a distribution for the

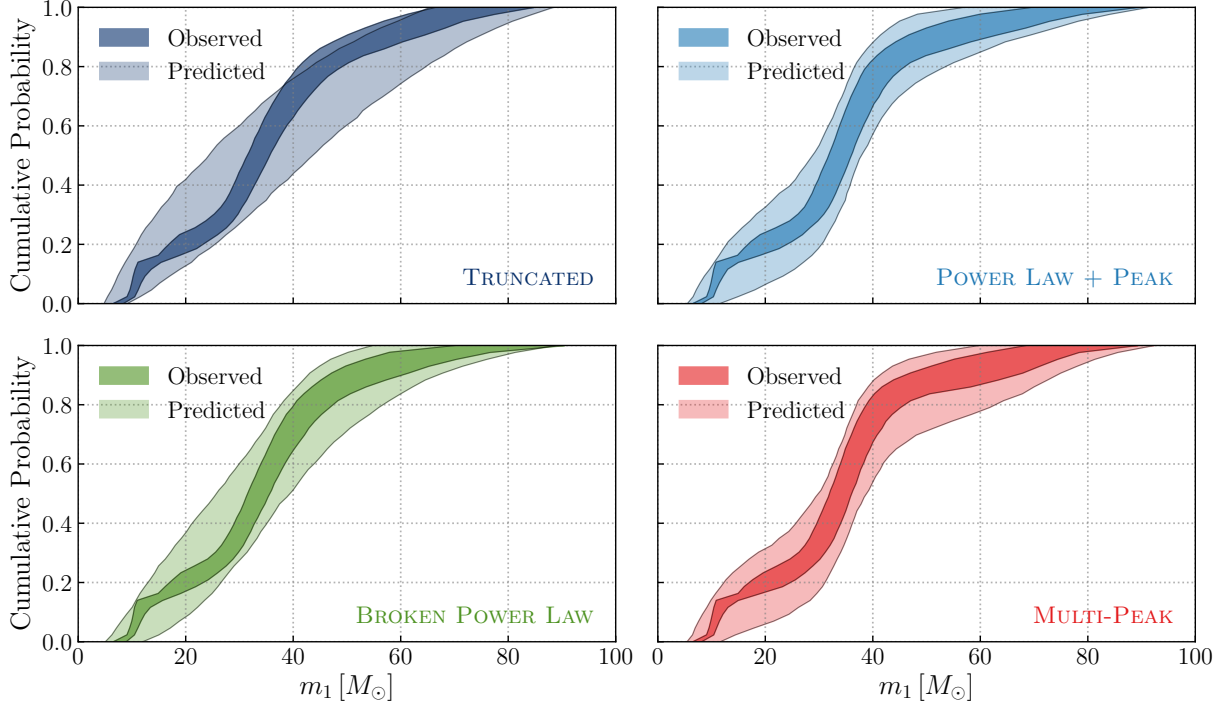


Figure 19. A posterior predictive check: the cumulative density function (CDF) of the observed primary mass distribution for the TRUNCATED, POWER LAW + PEAK, BROKEN POWER LAW and MULTI PEAK models. The observed event distribution is shown in the darker colors. The thickness of the bands indicates the 90% credibility range. The POWER LAW + PEAK, BROKEN POWER LAW and MULTI PEAK models are a better fit than the TRUNCATED model; the dark band overlaps entirely with the light colored band. This is due to the POWER LAW + PEAK, BROKEN POWER LAW and MULTI PEAK models having more flexibility to fit the relative excess of binaries in the $30 M_{\odot}$ – $40 M_{\odot}$ region compared to the $\gtrsim 40 M_{\odot}$ region. GW190814 is excluded from this analysis.

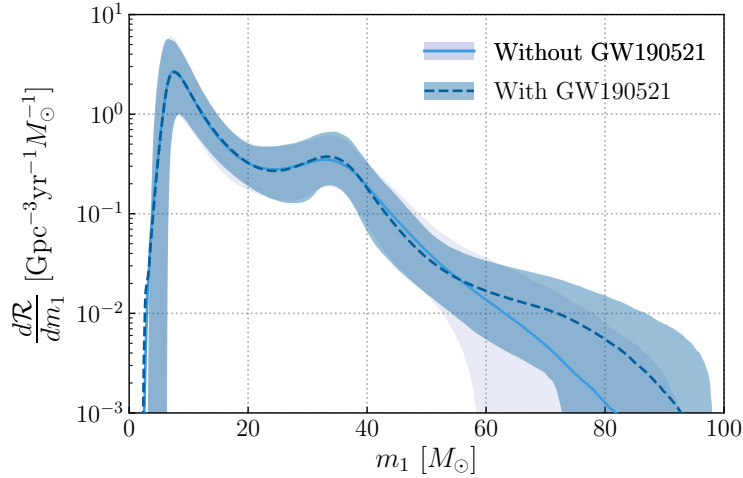


Figure 20. A comparison of the primary BH mass distribution for the population with and without GW190521. The data are fit using the POWER LAW + PEAK model; the BROKEN POWER LAW model produces similar results. The solid curves are the posterior predictive distributions while the shaded regions show the 90% credible interval. The inclusion/exclusion of GW190521 does not have a significant effect on the fit. GW190814 is excluded from this analysis.

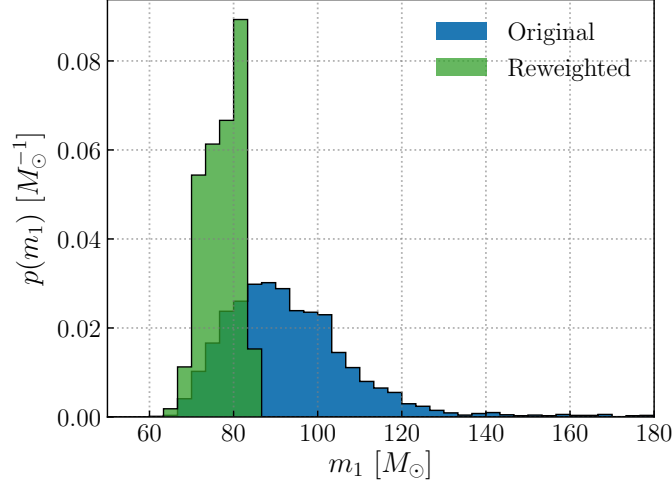


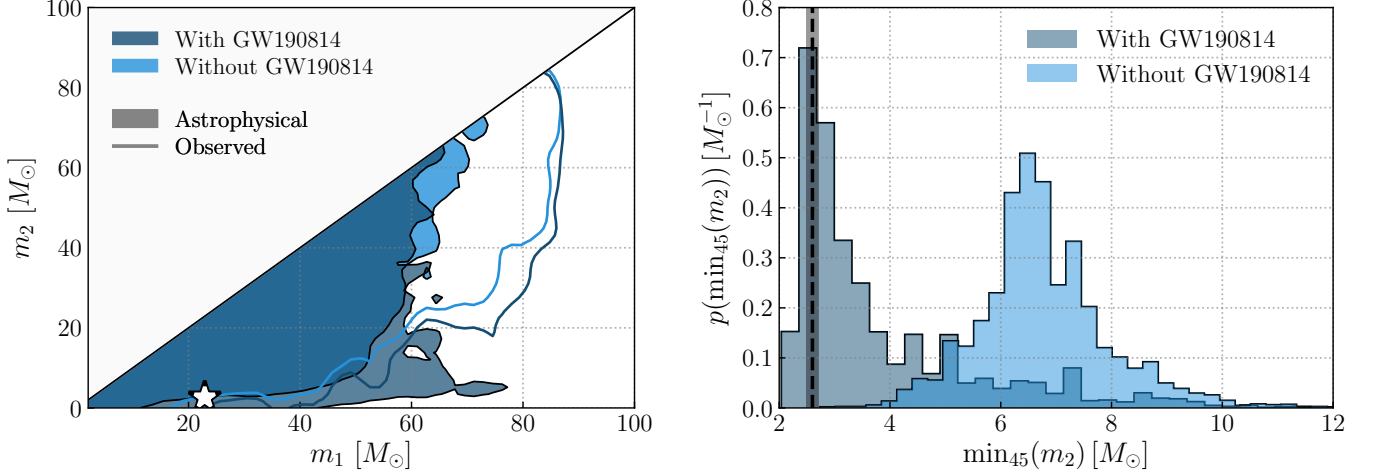
Figure 21. The posterior probability density for the primary mass of GW190521 using the original default prior (blue; flat in redshifted masses) and a reweighted version (green) obtained by using the POWER LAW + PEAK mass model. Results using the BROKEN POWER LAW mass model are similar. The reweighted version shifts the posterior support to lower masses, with $m_1 < 83 M_\odot$ (99% credibility).

minimum m_2 detected in a sample of 45 events. When using both the POWER LAW + PEAK and BROKEN POWER LAW models, we find that the observation of a system with a secondary mass equal to or smaller than the that of GW190814 ($2.59^{+0.08}_{-0.09} M_\odot$) is highly improbable, with probability $< 0.02\%$ for both POWER LAW + PEAK and BROKEN POWER LAW; see Fig. 22b for the distribution of the minimum observed secondary mass in a sample of 45 events predicted by the POWER LAW + PEAK model. The distribution for BROKEN POWER LAW is qualitatively similar. The mass ratio of GW190814 is also somewhat unusual according to this posterior predictive check; see Fig. 22a. Observing an event with the mass ratio of GW190814 or smaller, based on the fit to the other 44 BBH events, has probability $< 0.02\%$ in both the POWER LAW + PEAK and BROKEN POWER LAW models. These posterior predictive checks suggest that GW190814 is not a typical BBH, and support the conclusion that there may be a dearth of systems between $\sim 2.6 M_\odot$ and $\sim 6 M_\odot$. Future observations will reveal the precise shape of the mass distribution at low masses and extreme mass ratios, and better determine the nature of GW190814.

C.4. Mass and distance checks with a burst analysis

The earlier posterior predictive checks in this section compared simulated sets of BBH masses to the observed set of catalog events. As a complimentary posterior predictive check, we can simulate the gravitational-wave signals from these predicted events, run it through our search pipelines, and compare the synthetic data, as detected by the pipeline, to the observed data. As a proof of principle, we carry out this posterior predictive check with the COHERENT WAVEBURST (cWB) pipeline (Klimenko & Mitselmakher 2004; Klimenko et al. 2016), which is designed to detect unmodeled gravitational-wave transients. The cWB analysis resulted in the detection of 22 BBH events in GWTC-2. We investigate whether the set of cWB observations is consistent with the model predictions. We focus on assessing possible outliers at high masses and high redshifts, where cWB is especially sensitive to BBH signals. In particular, we examine whether GW190521, which was recovered with higher significance by the cWB search than the templated searches, is an outlier in the context of our mass and redshift models. Following Klimenko et al. (2016), we calculate the expected distribution of the central frequency f (which depends on the redshifted mass of the BBH) and coherent signal-to-noise ratio ρ (which, for a given redshifted mass, depends on the distance of the BBH) for two different population models: POWER LAW + PEAK and BROKEN POWER LAW, using the NON-EVOLVING redshift model. We then compare the empirical distribution of (f, ρ) , as recovered by the cWB pipeline to the distribution predicted by the population model. We quantify the comparison by calculating a p -value for each event i , which measures how unusual its observed (f_i, ρ_i) is, given the distribution of predicted (f, ρ) . The central frequency is a proxy for the redshifted mass while the signal-to-noise ratio is a proxy for the distance.

To compute the predicted distribution of (f, ρ) , we inject simulated waveforms drawn from the POWER LAW + PEAK and BROKEN POWER LAW distributions into the O1, O2 and O3a data and compile injections recovered by cWB

(a) The model-averaged astrophysical mass distribution $p(m_1, m_2)$.

(b) Observed minimum secondary mass distribution.

Figure 22. Left: the posterior population distribution for primary and secondary mass with and without GW190814. Shown here are the 99% credible intervals. Dark blue is with GW190814 and light blue is without. The shaded regions show the *astrophysical*, while the colored contours show the *observed* distribution (as it appears in the catalog due to selection effects). The median values of the posterior of GW190814 is marked with a star. Right: Distribution of the minimum secondary mass detected out of 45 detections, predicted from the fit to the POWER LAW + PEAK model to the BBH population excluding GW190814 (light blue) and the BBH population including GW190814 (dark blue). The dashed line and shaded region (gray) denote the median and 90% symmetric credible interval on the secondary mass of GW190814. This distribution is qualitatively similar to the distribution predicted from the fit to the BROKEN POWER LAW model.

with a FAR $< 1 \text{ yr}^{-1}$. The central frequencies and coherent signal-to-noise ratios of the recovered injections generated according to POWER LAW + PEAK are plotted in Fig. 23. The results for BROKEN POWER LAW are similar. The locations of the 22 detections on this plane are visually consistent with the model predictions, indicating that the model is a reasonably good fit to the data. The event with the lowest p -value (least consistent with predictions) is GW190521, with p -values of 0.053 and 0.077 for the BROKEN POWER LAW model and the POWER LAW + PEAK model respectively. These p -values indicate that GW190521 is a moderately unusual detection, but it is consistent with the population models.

D. DETAILS OF SPIN POPULATION MODELS

D.1. DEFAULT *spin* model

This model was introduced in Abbott et al. (2019a). Following Wysocki et al. (2019a), the dimensionless spin magnitude distribution is taken to be a Beta distribution,

$$\pi(\chi_{1,2}|\alpha_\chi, \beta_\chi) = \text{Beta}(\alpha_\chi, \beta_\chi), \quad (\text{D12})$$

where α_χ and β_χ are the standard shape parameters that determine the distribution's mean and variance. The Beta distribution is convenient because it is bounded on (0,1). The distributions for χ_1 and χ_2 are assumed to be the same. Following Talbot & Thrane (2017), we define $z = \cos \theta_{1,2}$ as the cosine of the tilt angle between component spin and a binary's orbital angular momentum, and assume that z is distributed as a mixture of two populations:

$$\pi(z|\zeta, \sigma_t) = \zeta G_t(z|\sigma_t) + (1 - \zeta)\mathcal{I}(z). \quad (\text{D13})$$

Here, $\mathcal{I}(z)$ is an isotropic distribution, while $G_t(z|\sigma_t)$ is a truncated Gaussian, peaking at $z = 0$ (perfect alignment) with width σ_t . The mixing parameter ζ controls the relative fraction of mergers drawn from the isotropic distribution and Gaussian subpopulations. The isotropic subpopulation is intended to accommodate dynamically assembled binaries, while G_t is a model for field mergers. The hyper-parameters for this model and their priors are summarized in Table 9. Additional constraints to the priors on μ_χ and σ_χ^2 are applied by setting $\alpha_\chi, \beta_\chi > 1$.

In Fig. 24 we provide a corner plot for the DEFAULT spin model. This model prefers modest spin magnitudes. It favors the hypothesis that binaries are preferentially aligned ($\zeta \rightarrow 1$ and $\sigma_t \lesssim 2$), albeit with potentially large misalignment

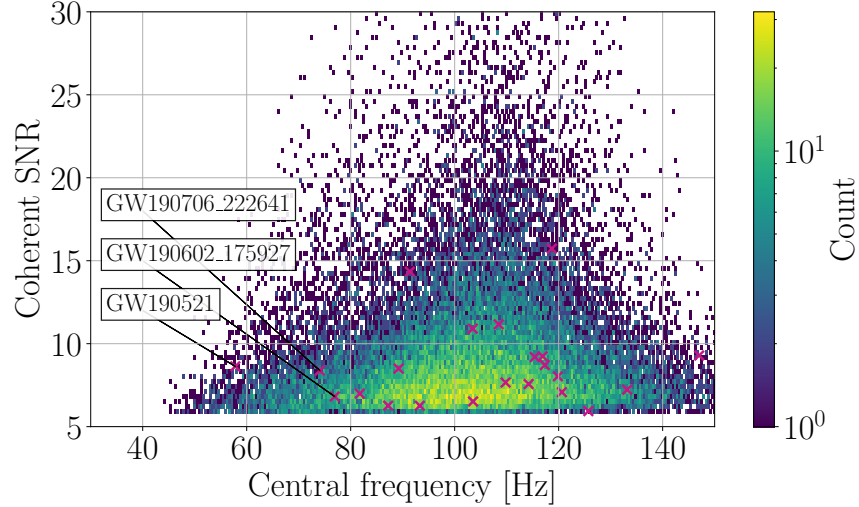


Figure 23. The coherent signal-to-noise ratio and central frequency for 22 BBH events detected by one of our detection pipelines, cWB, in O1, O2 and O3a (violet dots) compared to simulated BBH events from the POWER LAW + PEAK model detected by cWB. The consistency between the distributions of simulated and observed triggers shows that the POWER LAW + PEAK mass model coupled with the NON-EVOLVING redshift distribution is a good fit to the data. Results for the BROKEN POWER LAW model are similar.

Parameter	Description	Prior
μ_χ	Mean of the Beta distribution of spin magnitudes.	$U(0,1)$
σ_χ^2	Variance of the Beta distribution of spin magnitudes.	$U(0,0.25)$
ζ	Mixing fraction of mergers from truncated Gaussian distribution.	$U(0,1)$
σ_t	Width of truncated Gaussian, determining typical spin misalignment.	$U(0.01,4)$

Table 9. Summary of DEFAULT spin parameters.

angles ($\sigma_t > 0$). The case of *perfect* alignment, which would correspond to $\zeta = 1$ and $\sigma = 0$, is disfavored, lying outside the 99% credible bound on ζ and σ_t . Within the main text, Fig. 10 shows the implied distributions of component spin magnitudes and tilt angles. The implied distributions of the effective precession spin parameter (χ_p) and the effective inspiral spin parameter (χ_{eff}) are shown in Figs. 9 and 11, respectively; these distributions are in good agreement with the results obtained using the GAUSSIAN model described below. In particular, both models predict the existence of systems with anti-aligned spins (negative χ_{eff}), and in-plane spin components (non-zero χ_p).

D.2. GAUSSIAN spin model

The GAUSSIAN spin model offers an alternative description of BBH spins. It is convenient to measure the distribution of the effective inspiral spin parameter (χ_{eff}) and the effective precession spin parameter (χ_p), which are better constrained than individual component spin magnitudes or tilts. We parameterize the distributions of χ_{eff} and χ_p , using a bivariate Gaussian:

$$\pi(\chi_{\text{eff}}, \chi_p | \mu_{\text{eff}}, \sigma_{\text{eff}}, \mu_p, \sigma_p, \rho) \propto G(\chi_{\text{eff}}, \chi_p | \boldsymbol{\mu}, \boldsymbol{\Sigma}). \quad (\text{D14})$$

The distribution has a mean $\boldsymbol{\mu} = (\mu_{\text{eff}}, \mu_p)$ and a covariance matrix

$$\boldsymbol{\Sigma} = \begin{pmatrix} \sigma_{\text{eff}}^2 & \rho \sigma_{\text{eff}} \sigma_p \\ \rho \sigma_{\text{eff}} \sigma_p & \sigma_p^2 \end{pmatrix}. \quad (\text{D15})$$

The population parameters appearing in Eqs. (D14) and (D15) and their associated priors are summarized in Table 10. We truncate and normalize Eq. (D14) based on the allowed regions of the effective inspiral spin parameter: $\chi_{\text{eff}} \in (-1, 1)$ and $\chi_p \in (0, 1)$. The results from the GAUSSIAN model are obtained assuming a TRUNCATED mass model with $\alpha = -2.2$, $\beta_q = 1.3$, $m_{\text{min}} = 5 M_\odot$, and $m_{\text{max}} = 75 M_\odot$, consistent with the median values obtained when fitting the TRUNCATED

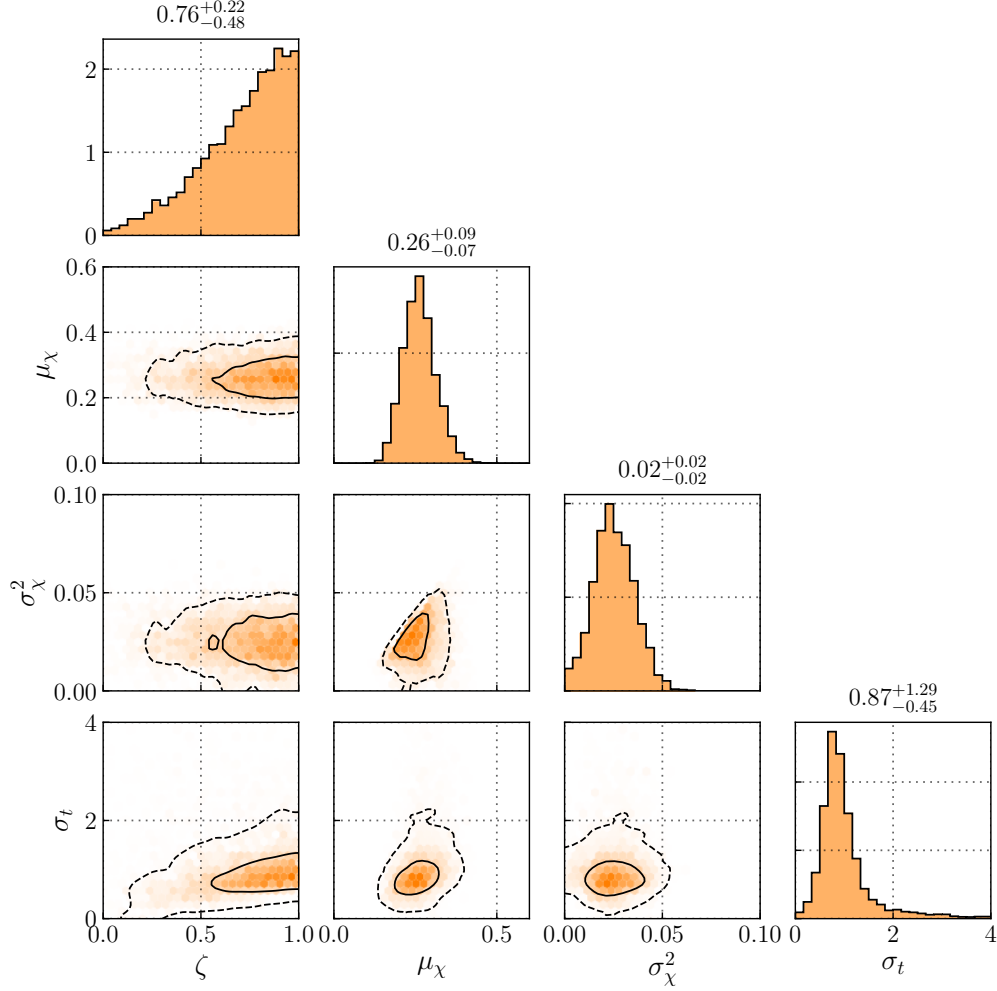


Figure 24. Posterior distribution for spin hyper-parameters for DEFAULT, assuming the POWER LAW + PEAK mass model and NON-EVOLVING redshift distribution. The fit excludes GW190814. The contours represent 50%, 90% credible bounds. A *perfectly* aligned spin distribution ($\sigma_t = 0$, $\zeta = 1$) is ruled out at $> 99\%$ credibility, consistent with the results of the GAUSSIAN model, but the data disfavor a purely isotropic distribution ($\zeta = 0$ or $\sigma_t \gtrsim 2$).

Parameter	Description	Prior
μ_{eff}	Mean of the χ_{eff} distribution.	$\text{U}(-1, 1)$
σ_{eff}	Standard deviation of the χ_{eff} distribution.	$\text{U}(0.01, 1)$
μ_p	Mean of the χ_p distribution.	$\text{U}(0.01, 1)$
σ_p	Standard deviation of the χ_p distribution.	$\text{U}(0.01, 1)$
ρ	Degree of correlation between χ_{eff} and χ_p .	$\text{U}(-0.75, 0.75)$

Table 10. Summary of GAUSSIAN spin parameters.

model to GWTC-2. We additionally assume a comoving merger rate density that grows as $(1+z)^{2.7}$. Although the TRUNCATED model is disfavored relative to the more complex mass models discussed above, it is sufficient for purposes of constructing an informed mass ratio distribution, the primary confounding factor in efforts to measure χ_{eff} and χ_p (Ng et al. 2018a).

The full posterior on parameters of the GAUSSIAN model is shown in Fig. 25. We find no correlation between the parameters of the χ_{eff} and χ_p distributions, nor do we obtain any information regarding the degree of correlation ρ between the effective inspiral spin parameter and the effective precession spin parameter. As discussed in Sec. 5.2,

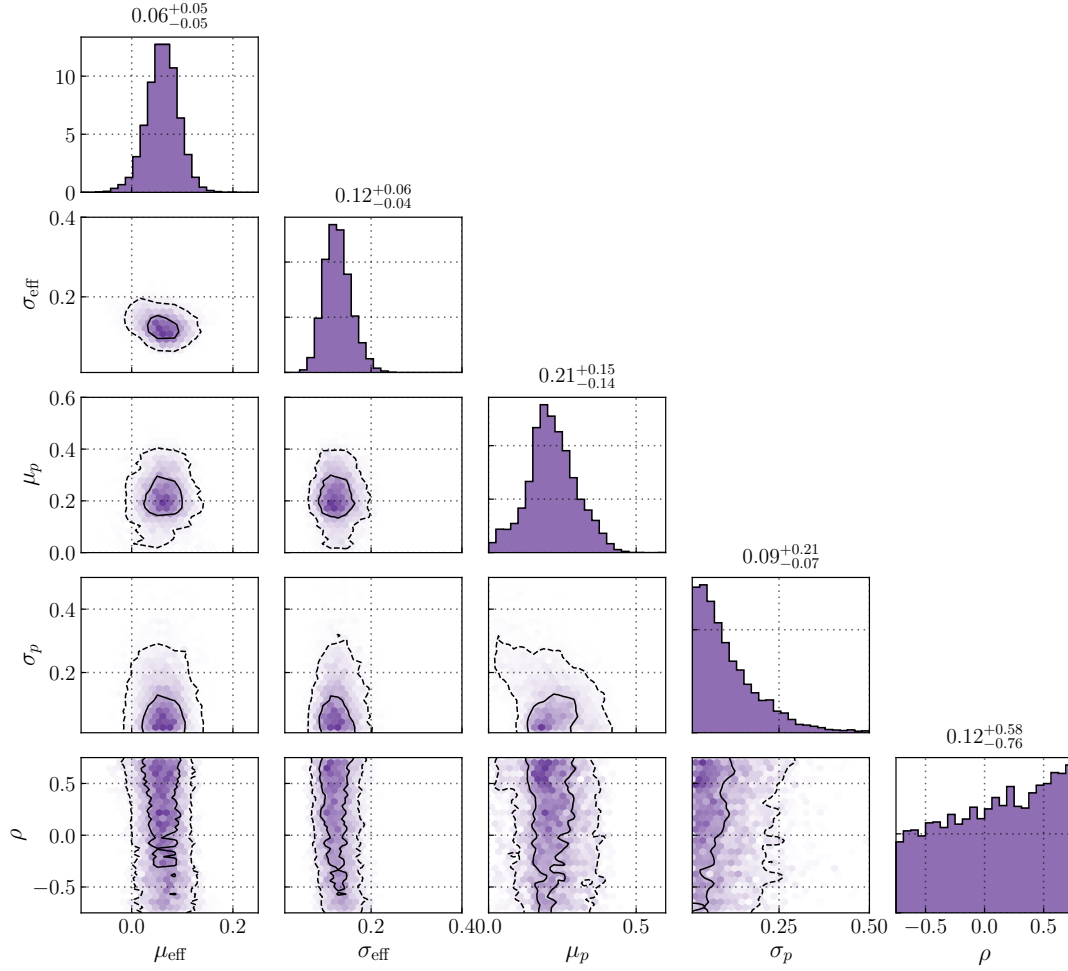


Figure 25. Posterior distribution for spin hyper-parameters under the GAUSSIAN model. The fit again excludes GW190814, and contours represent 50% and 90% credible bounds. Consistent with the results of the DEFAULT model, which results out a perfectly aligned spin distribution at 99% credibility, here we find that a vanishing χ_p distribution ($\mu_p = \sigma_p = 0$) is disfavored.

analysis with the GAUSSIAN spin model is consistent with the identification of spin-orbit misalignment using the DEFAULT spin model; with $\mu_p = \sigma_p = 0$ disfavored. For the DEFAULT spin model, we verified that the signature of spin-orbit misalignment was not a spurious prior artifact, finding that our posterior lies safely outside the artificial exclusion region in Fig. 9. A similar exclusion region also exists for the GAUSSIAN model around $\mu_p = \sigma_p = 0$, but our estimate of its exact size is subject to sampling uncertainties driven by the relatively small number of prior samples close to $\chi_p = 0$ for each event.

With the GAUSSIAN model, we also find evidence that at least some BHs have anti-aligned spins, with $\theta > 90^\circ$, such that $\chi_{\text{eff}} < 0$. To further evaluate the robustness of our GAUSSIAN model fits, in Fig. 26 we show posterior predictive comparisons between predicted and empirical catalogs of χ_{eff} and χ_p measurements. The light blue bands mark 90% credible bounds on the predicted cumulative distribution of observed effective inspiral spin parameter values, given our posterior on the GAUSSIAN model parameters. The dark shaded regions, meanwhile, show 90% credible bounds on the true distribution observed within GWTC-2, achieved by reweighting single event χ_{eff} and χ_p by repeated random draws from the GAUSSIAN hyper-posterior. A similar predictive comparison between observation and an alternative *strictly positive* model, in which the effective inspiral spin distribution is truncated on the interval $0 \leq \chi_{\text{eff}} \leq 1$, reveals possible tension; when asserting that all effective inspiral spins are positive, the resulting population model underpredicts the number of observations with $\chi_{\text{eff}} < 0.1$ approximately 75% of the time.

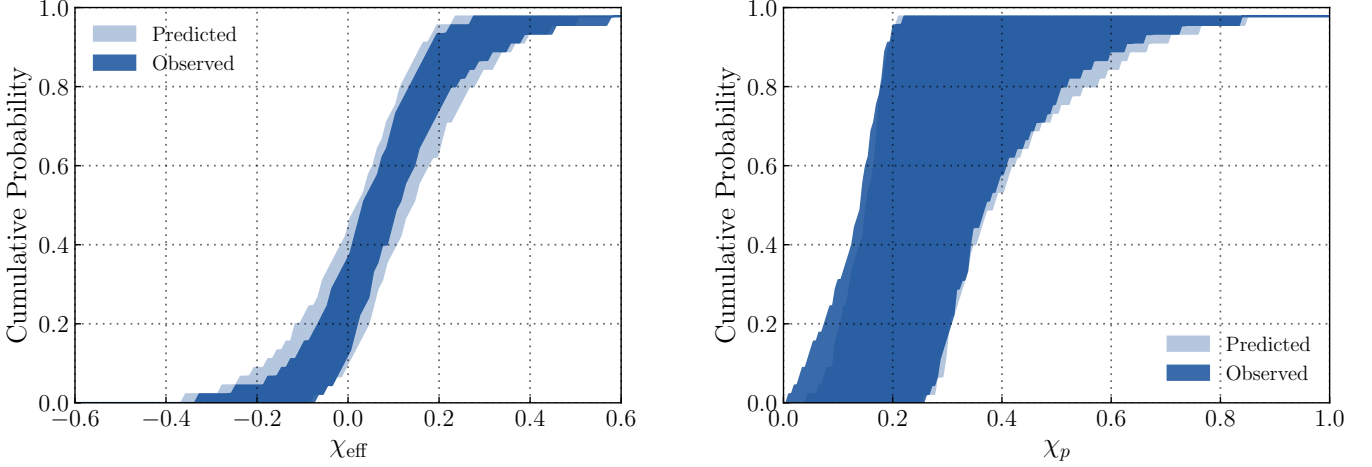


Figure 26. Population predictive checks for the effective inspiral spin parameter χ_{eff} (left) and the effective precession spin parameter χ_p (right) of BBH mergers using the GAUSSIAN spin model. The light shaded regions show the central 90% credible bounds on the posterior predictive distributions. According to the model, we expect the observed distributions on χ_{eff} and χ_p to lie within the light shaded region 90% of the time. The dark shaded regions show the 90% credible bounds on the observed distributions in GWTC-2, found using the population-informed posteriors of the confident BBH events in GWTC-2. The overlap between the dark and light regions shows that the model passes the posterior predictive check. The results for the DEFAULT model are similar, indicating that both models are a good fit to the data.

As described in the main text, we can leverage the assumption that BBH with negative values of χ_{eff} are formed dynamically to infer the fraction of binaries formed via dynamical (f_d) and isolated (f_i) channels; see Eq. (7). In Fig. 28 we show the corresponding posterior distributions for f_i and f_d .

There are several sources of possible bias that might influence our GAUSSIAN model conclusions. One possible source of bias is the mass model presumed for the GAUSSIAN spin analysis. As noted above, measurements of a binary’s χ_{eff} and mass ratio q are generally anti-correlated (Ng et al. 2018a). Therefore, our particular choice of $\beta_q = 1.3$ could conceivably affect conclusions regarding the χ_{eff} distribution. We have directly verified that the results in Fig. 27 remain robust under different fiducial choices of β_q between -1.5 and 2 .

Another source of bias may be the Gaussian functional form we impose on the χ_{eff} and χ_p distributions, enforcing a unimodal distribution with smooth tails. As discussed in Sec. 5.2, though, the DEFAULT spin model yields near-identical χ_{eff} and χ_p distributions, despite its different parametrization and different physical assumptions. As an additional check, we repeat the GAUSSIAN spin analysis on our data, truncating the χ_{eff} distribution not on $(-1, 1)$, but on $(\chi_{\text{eff}}^{\min}, 1)$, where χ_{eff}^{\min} is inferred from the data. Figure 27 shows the marginal posterior for χ_{eff}^{\min} . We find that χ_{eff}^{\min} is constrained to be negative at 99% credibility, confirming that support for negative effective inspiral spin parameter is a feature of the data and not simply an artifact of the GAUSSIAN model. In contrast, when we repeat the measurement of χ_{eff}^{\min} using simulated catalogs drawn from (i) a Gaussian population truncated to strictly positive values, and (ii) a pair of delta functions at $\chi_{\text{eff}} = 0$ and 0.1 , we correctly observe consistency with $\chi_{\text{eff}}^{\min} = 0$. Examining χ_{eff}^{\min} is therefore a useful safeguard even when the true population is poorly fit by a Gaussian. However, if the χ_{eff} distribution deviates too strongly from a Gaussian functional form, then it may remain possible to spuriously conclude that $\chi_{\text{eff}}^{\min} < 0$. In the case of significant tidal torques, for example, it is predicted that the χ_{eff} distribution is strongly bimodal, with effective inspiral spins clustered near $\chi_{\text{eff}} = 0$ or 1 , with no support at $\chi_{\text{eff}} < 0$ (Kushnir et al. 2016; Zaldarriaga et al. 2018; Bavera et al. 2019; Belczynski et al. 2020). To illustrate how results can be biased from model misspecification, we analyze mock observations drawn from a similar bimodal distribution. Using this intentionally misspecified model, we incorrectly conclude that $\chi_{\text{eff}}^{\min} < 0$. However, in cases of such extreme model mismatch, we expect that our data would fail the predictive check of Fig. 26. Indeed, Fig. 29 shows the result of such a predictive check in the case of the bimodal, tidally-torqued χ_{eff} distribution. When fitting this population with a Gaussian model, we find that the model overpredicts the fraction of mock observations with negative χ_{eff} as well as the range $0.3 \lesssim \chi_{\text{eff}} \lesssim 0.8$, showing a clear deviation in the predicted and observed cumulative χ_{eff} distributions.

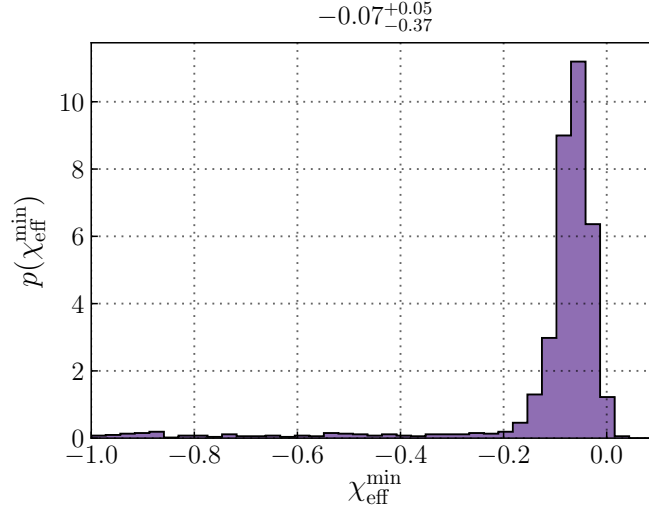


Figure 27. Posterior distribution for $\chi_{\text{eff}}^{\text{min}}$, below which we truncate the GAUSSIAN χ_{eff} distribution. While the results shown in the main text presume $\chi_{\text{eff}}^{\text{min}} = -1$, in Sec. D.2 we elevate $\chi_{\text{eff}}^{\text{min}}$ to a free hyper-parameter to be determined by the data; the resulting marginalized posterior distribution is shown here. In this case, we exclude $\chi_{\text{eff}}^{\text{min}} \geq 0$ at 99% credibility. This finding affirms that the signatures of anti-aligned BH spins are present in our BBH catalog, and not a bias due to our choice of parameterized spin model.

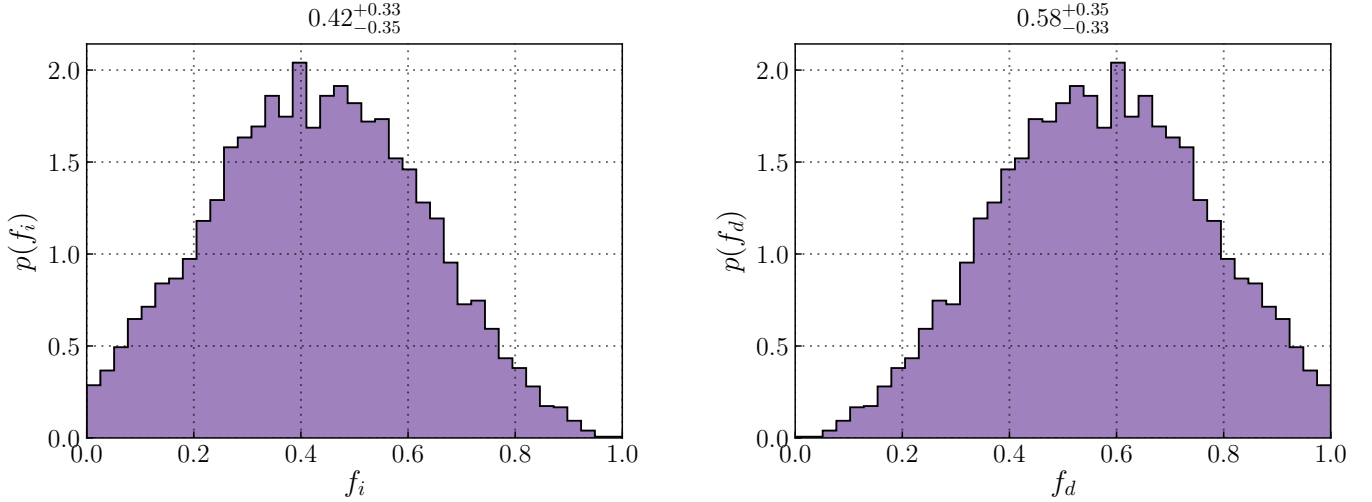


Figure 28. Posterior distributions for f_i (left) and f_d (right) of BBH mergers as defined Eq. 7. Assuming all binaries with $\chi_{\text{eff}} < 0$ are dynamically formed, f_d corresponds to the fraction of dynamically assembled BBH systems. f_i corresponds to the fraction of BBH systems formed through the isolated channel.

D.3. MULTI SPIN *model*

This model is an extension of the TRUNCATED mass model with an additional Gaussian component. It is similar to the POWER LAW + PEAK model, but there are several differences. First, the high-mass subpopulation in MULTI SPIN is described by a Gaussian in both m_1 and m_2 (up to the $m_1 \geq m_2$ truncation) while POWER LAW + PEAK only models m_1 as a Gaussian, and assumes that all BBH systems are described by a power-law distribution in mass ratio q . Most importantly, as its name suggests, MULTI SPIN allows each subpopulation to have its own independent spin distribution, each of which follows the DEFAULT model, with $\zeta = 1$. This allows us to probe whether the spin distribution varies with mass. The parameters for MULTI SPIN are summarized in Table 11.

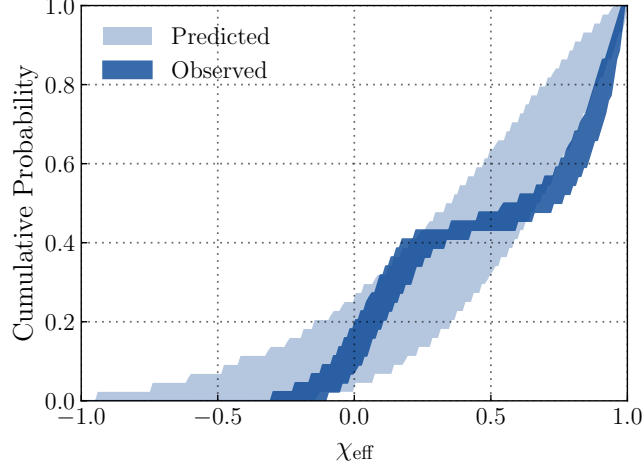


Figure 29. Example of a failed posterior predictive check for the effective inspiral spin parameter χ_{eff} distribution. We fit the GAUSSIAN spin model to a mock catalog drawn from the strongly bimodal χ_{eff} distributions predicted in the presence of tidal torques (Kushnir et al. 2016; Zaldarriaga et al. 2018; Bavera et al. 2019; Belczynski et al. 2020). The dark shaded region shows the central 90% credible bounds on the mock observed cumulative χ_{eff} distribution, while the dark region corresponds to that predicted by the model. In this case, our GAUSSIAN model is an extremely poor representation of the underlying χ_{eff} distribution, and so significant tension is seen between the observed and predicted distributions, with the model overpredicting the fraction of observations with $\chi_{\text{eff}} < 0$ as well the fraction of observations with $0.3 \lesssim \chi_{\text{eff}} \lesssim 0.8$.

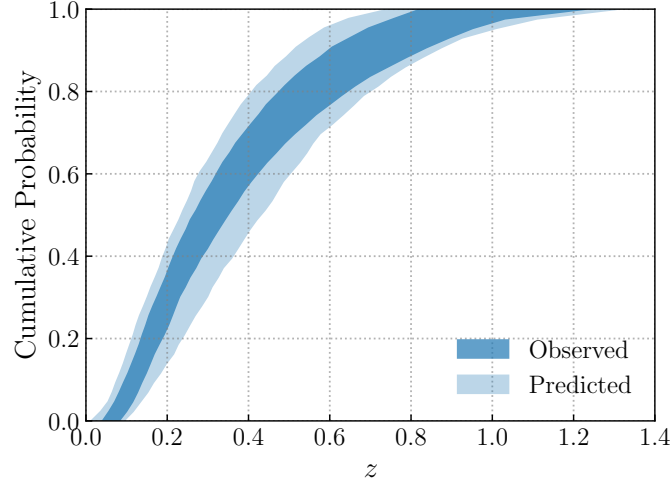


Figure 30. A posterior predictive check: the cumulative density function (CDF) for the POWER LAW EVOLUTION model. The model is a good fit to the data. GW190814 is excluded from this analysis.

E. REDSHIFT EVOLUTION MODELS

The POWER-LAW redshift evolution model parameterizes the merger rate density as

$$\mathcal{R}(z) = \mathcal{R}_0(1+z)^\kappa, \quad (\text{E16})$$

where \mathcal{R}_0 denotes the merger rate density at $z = 0$. This implies that the redshift distribution is

$$\frac{dN}{dz} = \mathcal{C} \frac{dV_c}{dz} (1+z)^{\kappa-1}, \quad (\text{E17})$$

where dV_c/dz is the differential comoving volume, and \mathcal{C} is related to \mathcal{R}_0 by

$$\mathcal{R}_0 = \mathcal{C} \frac{dV_c}{dz} \left[\int_0^{z_{\text{max}}} \frac{dV_c}{dz} (1+z)^{\kappa-1} \right]^{-1}. \quad (\text{E18})$$

Parameter	Description	Prior
\mathcal{R}_{pl}	Local merger rate for the low-mass power-law subpopulation.	$\text{U}(0, 5000)$
\mathcal{R}_{g}	Local merger rate for the high-mass Gaussian subpopulation.	$\text{U}(0, 5000)$
α_m	Power-law slope of the primary mass distribution for the low-mass subpopulation.	$\text{U}(-4, 12)$
β_q	Power-law slope of the mass ratio distribution for the low-mass subpopulation	$\text{U}(-4, 10)$
m_{min}	Minimum mass of the primary mass distribution for the low-mass subpopulation.	$\text{U}(2, 10)$
m_{max}	Maximum mass of the primary mass distribution for the low-mass subpopulation.	$\text{U}(30, 100)$
μ_{m_1}	Centroid of the primary mass distribution for the high-mass subpopulation	$\text{U}(20, 50)$
σ_{m_1}	Width of the primary mass distribution for the high-mass subpopulation	$\text{U}(0.4, 10)$
μ_{m_2}	Centroid of the secondary mass distribution for the high-mass subpopulation	$\text{U}(20, 50)$
σ_{m_2}	Width of the secondary mass distribution for the high-mass subpopulation	$\text{U}(0.4, 10)$
$\text{Mean}\chi_{1,\text{pl}}$	Mean of the beta distribution of primary spin magnitudes for the low-mass subpopulation.	$\text{U}(0, 1)$
$\text{Var}\chi_{1,\text{pl}}$	Variance of the beta distribution of primary spin magnitudes for the low-mass subpopulation.	$\text{U}(0, 0.25)$
$\sigma_{1,\text{pl}}$	Width of the truncated Gaussian distribution of $\cos(\text{primary spin tilt angle})$ for the low-mass subpopulation.	$\text{U}(0, 4)$
$\text{Mean}\chi_{2,\text{pl}}$	Mean of the beta distribution of secondary spin magnitudes for the low-mass subpopulation.	$\text{U}(0, 1)$
$\text{Var}\chi_{2,\text{pl}}$	Variance of the beta distribution of secondary spin magnitudes for the low-mass subpopulation.	$\text{U}(0, 0.25)$
$\sigma_{2,\text{pl}}$	Width of the truncated Gaussian distribution of $\cos(\text{secondary spin tilt angle})$ for the low-mass subpopulation.	$\text{U}(0, 4)$
$\text{Mean}\chi_{1,\text{g}}$	Mean of the beta distribution of primary spin magnitudes for the high-mass subpopulation.	$\text{U}(0, 1)$
$\text{Var}\chi_{1,\text{g}}$	Variance of the beta distribution of primary spin magnitudes for the high-mass subpopulation.	$\text{U}(0, 0.25)$
$\sigma_{1,\text{g}}$	Width of the truncated Gaussian distribution of $\cos(\text{primary spin tilt angle})$ for the high-mass subpopulation.	$\text{U}(0, 4)$
$\text{Mean}\chi_{2,\text{g}}$	Mean of the beta distribution of secondary spin magnitudes for the high-mass subpopulation.	$\text{U}(0, 1)$
$\text{Var}\chi_{2,\text{g}}$	Variance of the beta distribution of secondary spin magnitudes for the high-mass subpopulation.	$\text{U}(0, 0.25)$
$\sigma_{2,\text{g}}$	Width of the truncated Gaussian distribution of $\cos(\text{secondary spin tilt angle})$ for the high-mass subpopulation.	$\text{U}(0, 4)$

Table 11. Summary of MULTI SPIN parameters.

We take $z_{\text{max}} = 2.3$ in the analysis, as this is a conservative upper bound on the redshift at which we could detect BBH systems during O3a within the mass range considered here. When fitting this model, we employ a uniform prior on κ centered at $\kappa = 0$. The value $\kappa = 0$ corresponds to no evolution; i.e., a merger rate that is uniform-in-comoving volume and source-frame time. We take a sufficiently wide prior so that the likelihood is entirely within the prior range, $\kappa \in (-6, 6)$.

F. GRAVITATIONAL-WAVE LENSING

It has been suggested that gravitational-wave lensing could bias the estimate of binary masses (Dai et al. 2017; Ng et al. 2018b; Li et al. 2018; Oguri 2018; Hannuksela et al. 2019), which could lead to a biased population inference. However, based on the predictions on the number of expected gravitational-wave sources and the distribution of galaxy lenses in the Universe, Li et al. (2018); Oguri (2018) predict that only around one in a thousand observed events are lensed, although this estimate can vary depending on the redshift evolution of the merger-rate density. The lensing rate

is expected to be similarly rare for galaxy clusters ([Smith et al. 2018](#)). As the expected lensing rate is low compared to the number of events in GWTC-2, we assume that all events in our sample are unlensed.